UNIVERSITÀ DEGLI STUDI DI TRIESTE

XXIX CICLO DEL DOTTORATO DI RICERCA IN NANOTECNOLOGIE

Structure and chemical characterization of novel 2D homo- and hetero-organic architectures on a gold surface: a combined STM and photoemission spectroscopies study

Settore scientifico-disciplinare: FIS/03 – Fisica della Materia

DOTTORANDO
ZHIJING FENG

COORDINATORE
PROF. LUCIA PASQUATO

SUPERVISORE DI TESI
PROF. GIOVANNI COMELLI

TUTOR
DR. CARLO DRI

TUTOR
DR. ALBANO COSSARO

ANNO ACCADEMICO 2015/2016

Università degli Studi di Trieste

xxix ciclo del dottorato di ricerca in Nanotecnologie

Structure and chemical characterization of novel 2D homo- and hetero-organic architectures on a gold surface: a combined STM and photoemission spectroscopies study

settore scientifico-disciplinare fis/03 – Fisica della Materia

student Zhijing Feng

school director prof. Lucia Pasquato

supervisor prof. Giovanni Comelli

co-supervisor dr. Carlo Dri

co-supervisor dr. Albano Cossaro

Academic year 2015/2016

Abstract

This work focuses on the study of the electronic and structural properties of molecular architectures at metal surfaces formed by assembly of functionalized organics, in particular amino- and/or carboxylic-functionalized molecules. Several homo- and hetero-organic architectures are characterized on a gold (111) surface by means of combined low temperature scanning tunneling microscopy (LT-STM) and X-ray spectroscopy techniques, coupled with *ab initio* calculations performed in collaboration with theoretical groups. The aim is to identify the role of the molecule-molecule and molecule-substrate interactions in determining the electronic and structural configuration of the investigated systems. This thesis is subdivided in two parts. In the first part we report the homo-organic assembly of a simple solvent molecule, dimethyl sulfoxide (DMSO), and two different amino-functionalized molecules. In particular, DMSO is found to form molecular complexes unexpectedly trapping gold adatoms natively available on Au(111). Although such adatoms are not visible in the STM images, comparison between experiments and theoretical calculations shows that they are crucial for the stability of the observed DMSO complexes. Then, we have studied a small aminomethyl-functionalized molecule, 1-naphthylmethylamine (NMA), forming complexes of 3 or 4 molecules, and an aminophenyl-porphyrin forming hydrogen bonded molecular chains. In the latter two works, we have pointed out the interplay between the amino-amino and amino-gold substrate interactions which drive the formation of such complexes.

In the second part we exploit what we have learned about the amino-functionalized molecules on Au(111) to build novel hetero-organic supramolecular architectures based on the amino-carboxylic (A-C) interaction. Initially, we have studied the self-assembly of two small molecules, namely NMA and terephthalic acid (TPA, carboxylic-), whose 2D hetero-organic assembly is shown to be driven by the competition between the A-C and carboxylic-carboxylic recognition. In literature, organic templates are successfully synthesized on surfaces to build guest-host systems based on the shape matching between the host template and guest molecules. We instead exploit the competitive A-C bond to develop a novel guest-host method based on chemical affinity. By employing the monolayer of a carboxylic-functionalized porphyrin as the host template, we find that small guest aminomethyl-terminated molecules (like NMA) can be intercalated into this 2D template. These results show that the competitive A-C recognition is a powerful tool to build supramolecular assemblies.

Sommario

In questo lavoro si studiano le proprietà elettroniche e strutturali di architetture molecolari su superfici di metalli formate dall'assemblaggio di molecole funzionalizzate, in particolare con terminazioni amino- e/o carbossiliche. Diverse architetture omo- ed etero-organiche sono stati caratterizzate sulla superficie (111) dell'oro tramite microscopia ad effetto tunnel (STM) a bassa temperatura e tecniche di spettroscopia a raggi X, insieme a simulazioni fatte in collaborazione con gruppi teorici. L'obbiettivo è di identificare il ruolo delle interazioni molecola-molecola e molecola-substrato nel determinare la configurazione elettronica e strutturale dei sistemi studiati. Questa tesi è divisa in due parti. Nella prima parte descriviamo l'assemblaggio omo-organico di un semplice solvente, il dimetilsolfossido (DMSO), e di due diverse molecole con terminazioni amminiche. In particolare, il DMSO forma dei complessi molecolari che intrappolano adatomi di oro nativamente presenti su Au(111). Pur non essendo tali adatomi visibili nelle immagini STM, il confronto tra gli esperimenti e le simulazioni teoriche dimostra che essi sono fondamentali per la stabilità dei complessi di DMSO osservati. Successivamente, abbiamo studiato una piccola molecola, la 1-naftilmetilammina (NMA), che forma complessi di 3 o 4 NMA, e una amminofenil-porfirina che forma catene molecolari tramite legami idrogeno. In quest'ultimi due lavori, abbiamo analizzato i ruoli delle interazioni amino-amino e amino-oro, responsabili della formazione dei complessi.

Nella seconda parte sfruttiamo ciò che abbiamo imparato sulle molecole con terminazioni amminiche su Au(111) per costruire nuove architetture etero-organiche basate sull'interazione amino-carbossilica (A-C). Abbiamo prima studiato due piccole molecole, *i.e.* NMA e l'acido tereftalico (TPA, carbossilico), il cui assemblaggio etero-organico 2D è dimostrato essere guidato dalla competizione tra i legami A-C e carbossilico-carbossilico. I network organici vengono sintetizzati su superfici e usati per costruire sistemi ospite/ospitante basati sulla corrispondenza in dimensione e forma tra l'ospite e l'ospitante. Noi invece sfruttiamo l'interazione A-C competitiva per sviluppare un nuovo metodo ospite/ospitante basato sull'affinità chimica. Usando il monostrato di una porfirina carbossilica come network ospitante, troviamo che diverse piccole molecole amminiche (come la NMA) possono essere intercalate nel network 2D di porfirine. Questi risultati dimostrano che il legame competitivo A-C è un potente strumento per costruite assemblati supramolecolari.

Contents

Chapter 1

Introduction

The traditional semiconductor based devices have almost reached their miniaturization limit, and the industry has acknowledged that the Moore's law, the empirical principle that has driven the development roadmaps of the semiconductor companies since 1960s, cannot be pursued any further [1]. The end of Moore's law is both a technical and economic issue. From the economical point of view, the effort cost to further miniaturize the devices would exceed their economical return. From the technical point of view, when the devices approach atomic dimensions (few nanometers), several issues arise, such as the excessive heating of the integrated circuit caused by the fast electrons moving through the very tiny silicon circuits. Moreover, the rise of quantum mechanical effects that dominate matter at the atomic scale would make the transistors inevitably unreliable.

On one hand the industry has tried to partially circumvent these issues by redesigning the microprocessors; for example, to reduce the heating, the clock rate (how fast the microprocessors execute the instructions) was limited and a multicore design was adopted (two or more processors in a single chip). On the other hand, researchers are exploring different emerging technologies which are potential candidates to substitute the traditional semiconductor technologies. Therefore, the breakdown of Moore's law does not mean the end of innovation and progress, but it can be instead considered as a challenge to develop new technologies.

In this context, the technologies based on organic molecules are among the most promising approaches and their development is now an active area of research. Organic molecules are more versatile than traditional semiconductors and their integration in electronic circuits is at the basis of new-concept devices, such as OLEDs, biosensors, or organic photovoltaic cells. Moreover, the organic-based technologies can potentially solve the two problems affecting the semiconductor devices mentioned above. On one hand, organic molecules are (potentially) much cheaper and more scalable than semiconductors; on the other, organic molecules are potentially more efficient than semiconductors, and thus, for example, can help to solve the excessive heating issue. Furthermore, also in environmental terms organic molecules should be helpful since they are easier to recycle than semiconductor devices

[2]. However, up to now only few of these organic devices are present in our real life (OLED, for example) because several technological issues have to be faced and solved before such devices can be realized and launched on the market. One common limitation of these new technologies is their low efficiency due to the presence of defects in their structure and to the electronic transport properties at the organo-metallic interfaces, on which the functionality of such devices generally relies. To tackle these issues, the structural and electronic properties of molecular layers and molecular junctions need to be characterized in depth, in order to better understand the dependence of the properties of interest (*e.g.* homogeneity, conductance) on the molecular structure and the chemical properties of the adopted substrates.

In order to address these issues, significant effort by fundamental research is needed. In this framework, the aim of this thesis work is to study two-dimensional (2D) hydrogen bonded homo- and hetero-organic supramolecular assemblies at a metal surface. Among all the metal surfaces, gold single crystal terminations, due to their inertness, are the most popular substrates to support the growth of organic assemblies. Therefore, we chose to employ a monocrystalline Au(111) sample as the support for all the systems investigated in this thesis, since molecular interactions on and with this substrate are of great importance in diverse technological applications. The (111) face of gold is the most stable one and thus, where polycrystalline gold substrates or clusters are involved, (111)-terminated facets predominate [3, 4].

In synthesis, during my PhD work I made fundamental studies of 2D supramolecular assemblies on Au(111) in Ultra High Vacuum (UHV) conditions. Working in UHV chambers is necessary for this kind of studies in order to avoid the environmental contribution to sample preparations and measurements. Moreover, UHV is necessary for the X-ray spectroscopy techniques we employed for our studies, namely X-ray Photoelectron Spectroscopy (XPS) and Near Edge X-ray Absorption Fine Structure (NEXAFS), since these techniques are based on the detection of photoelectrons which are easily absorbed by the atmospheric gases. XPS is a quantitative spectroscopic technique that measures the elemental composition, chemical state and electronic state of the elements that exist within a material, and it is widely used in both industrial and fundamental research. NEXAFS, instead, is a less popular technique since it requires a synchrotron facility, but it has a higher sensitivity than XPS and can provide also geometrical information about the systems.

The main experimental technique used during my PhD is Scanning Tunneling Microscopy (STM) for characterizing the investigated systems. With STM it is possible obtain sub-molecular resolution images of a surface and, when at low temperature ($4 - 77$ K), to manipulate single molecules as well as to perform single molecule spectroscopies. Therefore, STM is the ideal technique to study 2D supramolecular systems. STM, XPS and NEXAFS are complementary techniques that together generally give a comprehensive experimental characterization of the system of interest. However, comparison with Density Functional Theory (DFT) simulations, performed in collaborations established *ad hoc* with theoretical groups, is fundamental to achieve a thorough understanding.

This thesis is organized as follows. **Chapter 2** is dedicated to the description of the STM, XPS and NEXAFS techniques and the relative experimental apparatus.

As to the obtained results, this thesis is divided into two main parts. In **Part I** we focus on the role of the Au(111) substrate in the molecular architectures, where the interplay between molecule-molecule and molecule-substrate interactions drives the formation of the supramolecular complexes. Each of the three chapters of this part refers to a molecule forming a peculiar homo-organic assembly. In particular:

- In **Chapter 3** we study the adsorption on Au(111) of a commonly used solvent, dimethyl sulfoxide (DMSO). We reveal that DMSO forms peculiar molecular complexes, unexpectedly trapping gold adatoms natively available on Au(111). Although not visible in the STM images, comparison between experiments and DFT calculations shows that the adatoms are crucial for the stability of the observed DMSO complexes.

- In **Chapter 4** we describe the complexes formed on Au(111) upon adsorption of a small prototypical aminomethyl-functionalized molecule, 1-naphthylmethylamine (NMA). We find that NMAs form complexes of 3 or 4 molecules, and we describe the role of the amino-amino and amino-gold substrate interactions in their assembly.

- In **Chapter 5** a different amino-amino bonded architecture is presented. We report about an amino-terminated tetraphenylporphyrin forming wires via some hydrogen bonds between the NH_2 terminations. Our combined STM experiments and DFT calculations demonstrate that in such wires each porphyrin is alternately a proton donor or acceptor; moreover, we show that the latter tends to trap native gold adatoms underneath. Furthermore, by STM manipulation experiments, we show that the donor porphyrins can behave as binary switches.

After studying the adsorption of molecules on Au(111), in particular amino-functionalized molecules, in **Part II** we exploit our knowledge about these molecules on Au(111) to build novel hetero-organic supramolecular architectures based on the amino-carboxylic (A-C) interaction. In particular:

- In **Chapter 6** we present a novel hetero-organic assembly strategy based on the chemical affinity between two small molecules, namely NMA and a carboxylic-functionalized molecule. By means of STM and XPS experiments, we show that the competition between the A-C and carboxylic-carboxylic recognition drives the formation of peculiar hetero-organic wires.

- In **Chapter 7** we exploit the competitive A-C bond to develop a novel guest-host method based on chemical affinity. In literature, the organic guest-host systems are based on the shape matching between a host organic template

and specific guest molecules. Instead, with our method no shape matching is required for the guest-host coupling, which is entirely based on the chemical affinity between two functional groups.

Finally, in **Chapter 8** conclusions and outlook are drawn.

Chapter 2

The experimental apparatus

In this chapter describe we the fundamental concepts of the experimental techniques used for our studies: the scanning tunneling microscope (STM), the X-ray photoelectron spetroscopy (XPS), and the near edge X-ray absorption fine structure (NEXAFS). Then we give a description of the experimental systems we used: the low temperature STM (LT-STM) and the ALOISA (Advanced Line for Overlayer, Interface and Surface Analysis) beamline for the XPS and NEXAFS measurements. The LT-STM experiments have been carried out at the IOM-CNR TASC Laboratory, whereas the ALOISA beamline is located in the ELETTRA Synchrotron light radiation facility, both being located in Basovizza (Italy).

2.1 Scanning tunneling microscope

The STM is a microscope with atomic resolution. Its invention in 1981 by Gerd Binnig and Heinrich Rohrer at IBM Zurich (Nobel Prize in Physics 1986) gave an incredibly powerful instrument to the development of the nanotechnology since it gave us the possibility to achieve outstanding atomic resolution images in real space [5]. To make a metaphorical comparison, we could say that the invention of STM is to nanotechnology as the telescope was to astronomy. Yet the STM can do more: it can be used to do inelastic electron tunneling spectroscopy (IETS) to observe vibrational states of individual molecules, it can probe the the density of states (DOS) close to the Fermi level of molecules through scanning tunnelling spectroscopy (STS), and it can be used to manipulate the single molecules (or atoms) on the surfaces, realizing the goal idealized by physicist Richard Feynman in his popular lecture "*There's Plenty of Room at the Bottom*" at the American Physical Society meeting at Caltech on December 29, 1959 [6].

Thus STM is the ideal technique to study surface phenomena at the atomic scale and, in particular, supramolecular structures on metal surfaces.

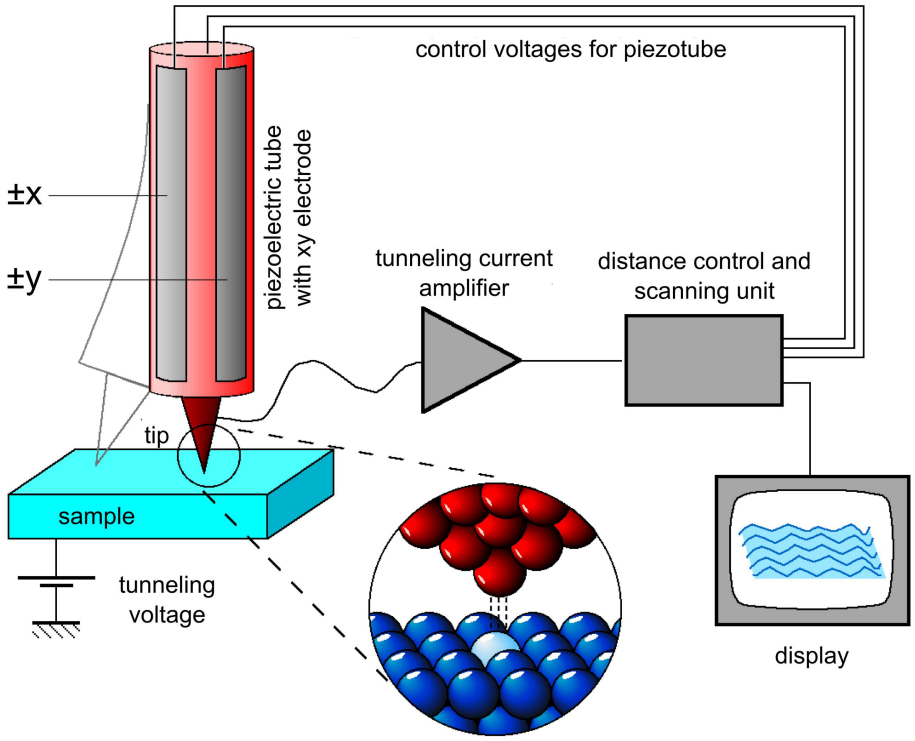

Figure 2.1: The general scheme of a STM: the distance control is the feedback mechanism to control the tip height. Image from [7].

2.1.1 Operating principle

When a metallic tip is approached to a conductive surface, a potential barrier due to the vacuum gap is present between the two objects. If a voltage bias is applied between them, and their distance is small enough, the electrons can tunnel across the potential barrier from the tip to the sample or vice versa, giving rise to a current flow between them, which is strongly dependent on the tip-to-sample distance: this phenomenon is called quantum tunneling.

The STM images are obtained scanning the tip over an area (x,y) of the surface with sub-angstrom lateral resolution and recording the tip heigh z or the tunneling current I. Therefore the recorded (x, y; z(x,y)) or (x, y; I(x,y)) data are displayed in a 2-dimensional plot.

The tip position is controlled via a piezoelectric tube in the (x,y) directions through the electrodes along the tube and in the z direction (tip height) through a feedback mechanism (fig. 2.1). Since the piezoelectric expansion/contraction is controlled with sub-angstrom precision in the (x, y, z) directions, the tip is scanned over an area of the surface with sub-angstrom resolution and high resolution images of the surface of interest can be obtained.

There are two modes of scanning of STM (fig. 2.2):

- **constant height mode:** the tip is kept at a constant height (constant z) while scanning, and the tunneling current I(x,y), which is recorded in every scan point, is color-coded to form the STM image (x, y; I(x,y));
- **constant current mode:** during the scan, the tunneling current is kept constant by changing the tip height z by means of an electronic feedback system, and the STM image (x, y; z(x,y)) is formed by color-coding the tip height z(x,y) at every scan point.

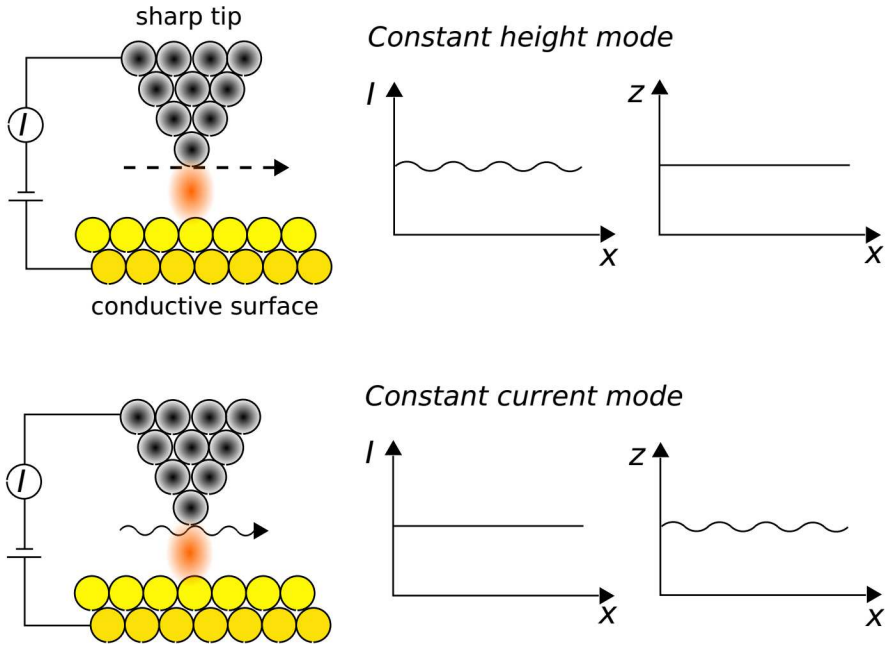

Figure 2.2: The two imaging modes

Comparing the two scanning modes, the constant height mode has the advantage to be faster since the z parameter is held constant and only the current I(x,y) is measured, while in the constant current mode a feedback mechanism (fig. 2.1) is necessary to change the z(x,y) parameter. Nevertheless, the constant height mode can be used only for very plane and regular surfaces since any surface step or irregularity can make the tip crash against the surface. In our experiments we will use only the constant current mode.

The information contained in an STM image is not simply the topography of the surface because the tip is governed by the tunneling current, which depends not only on the geometrical position of the atoms at the surface, but also on the spatial distribution and the energy of the tip/sample electronic states available for the tunneling process, as we will see in the following sections.

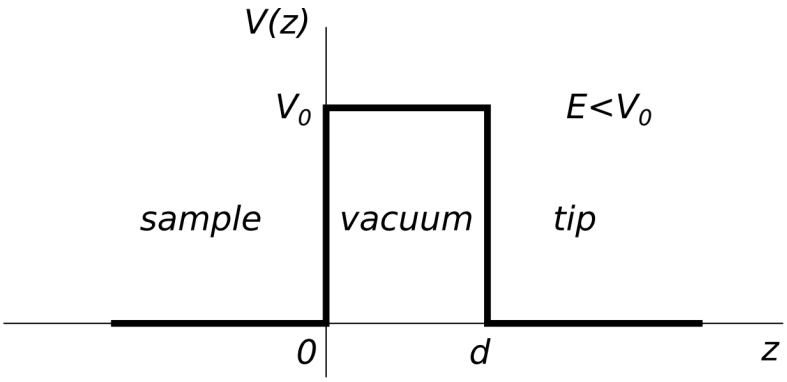

Figure 2.3: The representation of the one dimensional barrier problem.

2.1.2 Quantum tunneling

As mentioned before, the physical principle that make possible the STM is the quantum tunneling. The tunneling of electrons between the tip and the sample across the vacuum barrier, in a first rough approximation, can be thought as a simple tunneling across a rectangular potential barrier in one dimension (fig. 2.3). Therefore, to understand the principle, let's solve this simple quantum mechanics problem: the one dimensional potential barrier which is a typical exercise in a first course of quantum mechanics.

Suppose an electron traveling represented by the wave function $\psi(z)$ in the following potential:

$$\begin{cases} V(z) = 0 & z < 0 \\ V(z) = V_0 & 0 \leq z \leq d \\ V(z) = 0 & z > d \end{cases}$$

Therefore, supposing our electron having an energy $E < V_0$ the Schröedinger equation

$$-\frac{\hbar^2}{2m}\frac{d^2\psi(z)}{dz^2} + V(z)\psi(z) = E\psi(z)$$

has the general solution

$$\begin{cases} \psi(z) = Ae^{i\alpha z} + Be^{-i\alpha z} & z < 0 \\ \psi(z) = Ce^{kz} + De^{-kz} & 0 \leq z \leq d \\ \psi(z) = Fe^{i\alpha z} + Ge^{-i\alpha z} & z > d \end{cases}$$

where

$$\begin{cases} \alpha = \dfrac{\sqrt{2mE}}{\hbar} \\ k = \dfrac{\sqrt{2m(V_0 - E)}}{\hbar} \end{cases} \tag{2.1}$$

Supposing the electron going from the sample to the tip (fig. 2.3), we would have two simplifications:

- $Ce^{kz} = 0$ since it would imply that probability of finding the electron at a distance z from the $z = 0$ plane would increase with z, which is absurd in the case of an electron impinging on the barrier from the left.
- $Ge^{-i\alpha z} = 0$ since in the right part we can have only transmitted wave.

Therefore, to have physical meaning we have to set $C = G = 0$. Doing the matching of the wave functions and their first derivative in 0 and d and making the proper approximations, we get the following solution for $0 \leq z \leq d$:

$$\psi(z) = \psi(0)e^{-kz} \tag{2.2}$$

By locating the sample at the $z = o$ plane and the tip apex at $z = d$ as in figure 2.3, the probability of finding the electron on the tip is proportional to the square modulus of the wave function in d:

$$w \propto |\psi(d)|^2 = |\psi(0)|^2 e^{-2kd} \tag{2.3}$$

The tunneling current is proportional to the probability of electron tunneling. Therefore, if the exponential term in (2.3) is not too small, *i.e.*, if the distance sample-tip is not too big, there is a measurable current flowing through the system sample-vacuum-tip junction without sample-tip contact.

2.1.3 Metal-vacuum-metal tunneling

In the previous section we showed a simple exercise to explain the concept of quantum tunneling; now we want to treat the real case.

If there were no electrical connection between the sample and the tip, each one would have its own Fermi energy E_F and the same defined vacuum level E_{vac} (fig. 2.4a). If we connect electrically the tip with the sample (that's in the STM), the Fermi energy will become equal. It is clear that at $T \approx 0$ K, all the states below E_F will be filled, and no states will be occupied above E_F, then there would be no tunneling since there are no states for the electrons to tunnel to (fig. 2.4b).

Therefore, we have to apply a bias voltage between the tip and the sample to have the tunneling current flow (fig. 2.4c-d). If the sample bias is negative, an electron in a sample state ψ_n with energy E_n lying between E_F and $E_F + eV$, has a chance to tunnel into an empty state of the tip (fig. 2.4c) or vice versa (fig. 2.4d).

For example, we take the case of the sample biased negatively of figure 2.4c. For notation simplicity, we take the sample as reference for our notation and we define $E_F \equiv E_F^S$ and $\phi \equiv \phi_s$. ϕ is the work function of the metal, which is defined as the minimum energy required to extract an electron from the bulk to the vacuum level. If we neglect all temperature effects, the Fermi energy is exactly the upper limit of

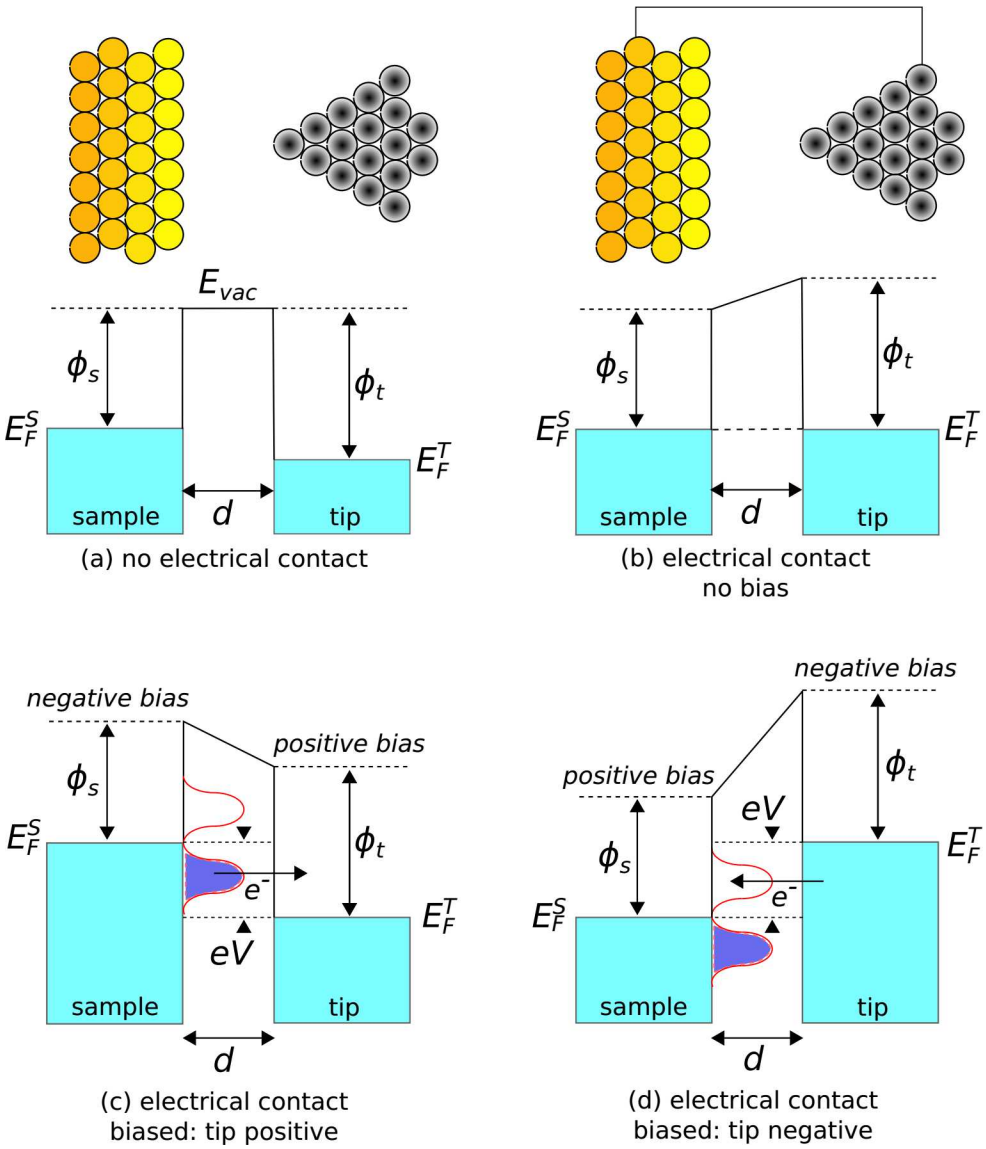

Figure 2.4: (a) No electrical contact between the tip and the sample: the vacuum level is the same for both. (b) Electrical contact but no bias: same Fermi energy ($E_F^S = E_F^T$) but no tunneling. (c) and (d) Electrical contact and bias: tunneling. $E_F \equiv E_F^S$ = sample Fermi energy, E_F^T = tip Fermi energy, $\phi \equiv \phi_s$ = sample work function, ϕ_t = tip work function, V = bias voltage.

the occupied states in a metal; thus, within our model $E_F = -\phi$ (we put $E_{\text{vac}} = 0$). If the bias is small, *i.e.* if $eV \ll \phi$, we can approximate

$$E_n \approx -\phi$$

where E_n is the energy (around E_F) of an electron involved in the tunneling process. Then the probability w for the electron in the nth sample state ψ_n to tunnel in the tip (or vice versa), from equation (2.3), is

$$w \propto |\psi(0)|^2 e^{-2kd}$$

where

$$k = \frac{\sqrt{2m\phi}}{\hbar}$$

since from equation (2.1) $V_0 - E \approx \phi$ (because $V_0 \equiv 0$ and $E \approx E_F \approx -\phi$). Now, since every tunneling electron would contribute to the current flow, the tunneling current is the result of the sum of the contributions of all electrons having enough energy flow from the sample to the tip (*i.e.* energy E_n lying between E_F and $E_F + eV$):

$$I \propto \sum_{E_n = E_F - eV}^{E_F} |\psi_n(0)|^2 e^{-2kd} \tag{2.4}$$

If V is sufficiently small, then the sum in equation (2.4) can be replaced with the local density of states (LDOS) at the Fermi level. The LDOS is the number of electrons per unit volume per unit energy at a given point in space and at a given energy: at a distance z from the sample, the LDOS at the energy E is defined as

$$\rho_S(z, E) \equiv \frac{1}{\varepsilon} \sum_{E_n = E - \varepsilon}^{E} |\psi_n(z)|^2$$

for a sufficiently small ε. By using this expression for the LDOS, the current can be rewritten as [8]:

$$\begin{aligned} I &\propto V \rho_S(0, E_F) e^{-2kd} \\ &\approx V \rho_S(0, E_F) e^{-1.025\sqrt{\phi} d} \end{aligned} \tag{2.5}$$

The equations (2.5) tell us two important things about STM:

- They show that an STM image is a Fermi level LDOS contour of the sample surface.
- The tunneling current is extremely sensitive to very small differences in the tip-sample distance, thus the STM can follow the corrugation of single atoms while scanning above the surface. In fact, if we consider a typical metal work

function $\phi \approx 4$ eV, then we obtain the typical value of the decay constant $k \approx 1$ Å^{-1}: the current decays of a factor $e^2 \approx 7.4$ when the distance changes of $\Delta d = 1$ Å, *i.e.* it's extremely sensitive to small change in tip-surface distance.

Up to now, we have treated one-dimensional systems for simplicity to explain the principle of STM, but obviously the tunneling process occurs in 3-dimensional systems. In 1961, well before the invention of the scanning tunneling microscope, Bardeen developed an extension of the one dimensional tunneling problem to the three dimensional case [9]. Instead of solving the complicated Schröedinger equation for of the entire metal-insulator-metal system, his approach was to initially solve it for two electrodes as separate entities and then calculate their overlap. What he calculated is the M matrix element, *i.e.* the probability of tunneling from a state ψ , on one side of the barrier (*e.g.* sample), to a state χ on the other side (*e.g.* tip):

$$M = \frac{\hbar}{2m} \int_{z=z_0} \left(\chi^* \frac{\partial \psi}{\partial z} - \psi \frac{\partial \chi^*}{\partial z} \right) dS$$

where $z = z_0$ is a separation surface lying entirely within the two electrodes. Following Bardeen's approach, by determining the rate of electron transfer between the two states and by assuming that $k_B T$ is small enough (which is a good approximation in most of experiments) to approximate the Fermi distribution with a step function, we obtain the following expression for the tunneling current:

$$I = \frac{4\pi e}{\hbar} \int_0^{eV} \rho_S(E_F - eV + \varepsilon) \rho_T(E_F + \varepsilon) |M|^2 d\varepsilon$$

Eventually, if the M matrix is assumed to be almost constant within the range of interest, we obtain a final, simplified expression for the tunneling current:

$$I \propto \int_0^{eV} \rho_S(E_F - eV + \varepsilon) \rho_T(E_F + \varepsilon) d\varepsilon \tag{2.6}$$

Then, the tunneling current, within Bardeen's extension of the one-dimensional tunneling problem, is not only a constant LDOS contour at the Fermi level, but rather a convolution of the density of states (DOS) of the two electrodes.

2.1.4 Manipulation of atoms and molecules

As already anticipated, the STM can be used also to manipulate the single atoms or molecules. The manipulation of atoms and molecules on a metal surface consists in using the tip to move a chosen atom (or molecule) to another chosen position on the surface [10, 11] or to induce conformal [12] or chemical [13, 14] modifications of the molecules.

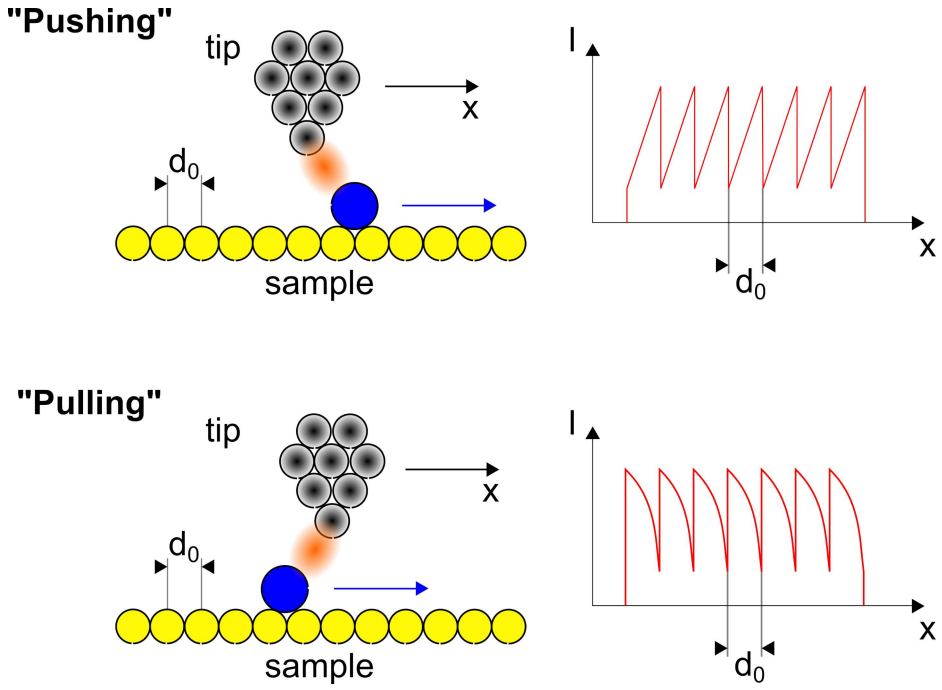

Figure 2.5: The different lateral manipulation modes. The "pushing" mode, where repulsive forces are involved and the "pulling" mode where attractive forces drive the manipulation. The right panels show the typical current signal during the manipulation process. Notice that the periodicity of the signal in this case corresponds to the periodicity of the underlying substrate along the direction of the manipulation path.

To move a molecule in the desired place, one positions the tip above (on top or on the side) the molecule and then, by increasing the set tunneling current, the tip moves towards the molecule to interact (attractive or repulsive interaction) strongly enough to move it through the surface (*i.e.* the interaction energy between the tip and the atom reaches the so called *diffusion activation energy*). Then the molecule is moved by the tip to the desired position, and finally the tunneling current is decreased so that the tip restores to the imaging condition [8].

The molecule can be moved in two ways:

- **Vertical manipulation**: generally refers to the process where a single atom or a molecule is transferred between the tip and the surface, that can also be used to relocate the adsorbates across the surface by pick-up and release.

- **Lateral manipulation**: adsorbates are laterally relocated by means of the tip without losing contact with the substrate. There are two modes: the "pushing" and the "pulling" mode (fig. 2.5). In the "pushing" mode, the tip is laterally approached to the adsorbate and, when the tip-adsorbate repulsive forces are sufficient to overcome the diffusion barrier, the adsorbate hops to the next available substrate site, while at the same time the current signal

drops abruptly. In the "pulling" mode, the process is similar, with the only difference that this time attractive tip-adsorbate forces are driving the hopping of the molecule between the sites.

These are the classical ways to move adsorbates through the surface.

As said before, manipulation includes not only the moving of molecules and atoms, yet also the induction of conformation changes inside molecules or modification of the chemistry of the molecules.

One way to induce modifications in a molecule is to place it in an electric field that modifies the potential on the molecule and, depending on their polarizability, can also induce a dipole moment. To do this one can simply position the tip on the interested adsorbate and set the proper bias voltage that induces the electric field (which depends strongly also on the atomic scale tip apex, which is unknown): this is what we call "**V-pulse**". This manipulation technique is called "electric field-induced manipulation". Moreover, a higher bias means also tunneling electrons with higher energy, which can induce geometrical and chemical modifications of the molecules through inelastic electron tunneling.

2.1.5 Scanning tunneling spectroscopy

Although STM has the great advantage to give us real space atomic-resolution images of the surfaces, it lacks of chemical sensitivity. However, thanks to technical and theoretical development, the STM has evolved so that we can get information about the electronic properties of samples and adsorbates by Scanning Tunneling Spectroscopy (STS) [15, 16] and about vibrational mode of a molecule by Inelastic Electron Tunneling Spectroscopy (IETS). Here we give a brief description of these two techniques.

Following the Bardeen's formalism, and assuming the tip with a constant DOS, from the equation (2.6) the first derivative of the tunneling current gives:

$$\frac{\mathrm{d}I}{\mathrm{d}V} \propto \rho_S(E_F - eV) \tag{2.7}$$

and thus it is possible to probe the DOS of the sample, or molecular states close to the Fermi level, through the tunneling current conductance: this is the scanning tunneling spectroscopy (STS). Since the tunneling current exhibits a dramatic dependence on the tip-sample separation, STS data need to be normalized for comparison. The commonly used normalization is the one proposed by Feenstra and Stroscio [17]:

$$g_N(V) \equiv \frac{\mathrm{d}\,\ln I}{\mathrm{d}\,\ln V} = \frac{\mathrm{d}I}{\mathrm{d}V} \cdot \frac{V}{I} \tag{2.8}$$

called *normalized dynamic conductance*.

The achievable resolution in the dI/dV spectra is strongly temperature dependent and thus, in order to perform STS with high energy resolution, it is necessary

to work at low temperatures. Moreover, working at low temperatures guarantees optimum stability of the tip position, thanks to the reduced thermal drift, and consequently more reliable STS spectra.

To acquire dI/dV spectra, a lock–in amplifier is commonly used to recover the signal of interest from the background noise. In particular, the first harmonic of the lock–in output is recorded, which directly gives the first derivative of the tunneling current. In a typical STS measurement, the tip is moved to a point of interest on the surface, then the feedback loop (the feedback circuit for the constant current imaging mode) is switched off and the voltage is ramped while recording the signal from the lock–in amplifier, producing thus a dI/dV versus V graph.

When characterizing molecules adsorbed at surfaces, however, there are a number of limitations in employing the STS technique. First of all, occupied states of the sample which lie at the upper range of the energy window ΔE available for the tunneling process, represented in figure 2.4c, d, contribute more significantly to the tunneling current (as shown by the arrows) since the barrier height seen by these states is lower. Conversely, low–lying states (*i.e.* far below the Fermi level of the sample) have little contribution to the tunneling current. Therefore, the sensitivity of STS to occupied sample (or adsorbate) states rapidly decreases with increasing energy below E_F [18].

Secondly, the allowed range of the electron energies (*i.e.* gap voltages) is within ±4 eV and ±5 eV since in this limit we approach the typical work function of one of the two metals, where field emission occurs. However, as has been shown by photoemission spectroscopy experiments, interesting features expected for adsorbates often appear out of this range [19]. The range is often further limited by other processes, for instance by molecular dissociation that can occur due to vibrations induced by inelastic tunneling processes, at voltages well below the field emission limit. For these reasons, the STS spectra presented in this thesis are typically within the ±2 eV range. Third, with STS a chemical identification of the molecules requires the support of theoretical calculations [19].

Inelastic Electron Tunneling Spectroscopy (IETS) gives instead a more direct chemical information, since it allows to access the vibrational modes of an adsorbed molecule [19].

For electrons tunneling through adsorbed molecules, in addition to the elastic electron tunneling path (*i.e.* electrons that tunnel between states with the same energy), above a certain bias threshold, a new tunneling path can appear, where electrons lose their energy by exciting a vibrational mode of a molecule. The existence of a threshold is understood by considering that the maximum energy which can be lost by the tunneling electron is eV, thus the process occurs only if $eV > \hbar\omega$, where $\hbar\omega$ is the vibrational quantum.

The opening of the new tunneling channel increases the conductance (dI/dV) for $V > 0$. Since this increase is very small in the conductance, it is more clearly detected as a change in the differential conductivity d^2I/dV^2. In practice, $\mathrm{d}^2I/\mathrm{d}^2V$ spectra are measured by fixing (x, y) tip position over the position of interest, switch-

ing off the feedback and ramping the voltage within the desired range while the second harmonic output of the lock-in amplifier is recorded. In order to improve the signal to noise ratio, many spectra are averaged.

2.2 The low temperature STM

Having described the characteristics of STM technique, we give here a description of our STM instrument: the low temperature STM (LT-STM). The LT-STM is basically a STM designed for working at very low temperatures.

The LT-STM is a ideal technique for studying the structural properties of organic molecules adsorbed on metal surfaces, since low temperatures limit or block the motion of molecules allowing the STM, which is relatively a slow technique, to image them (for some molecules this would be impossible at room temperature). Moreover the LT-STM is capable of intrinsic higher resolution than a room temperature one since low temperatures reduce the vibrational motion of the molecules allowing thus the STM-tip to probe more details. Furthermore at lower temperatures the intrinsic width of the electronic states, which has a $k_B T$ dependence, is narrower, further enhancing the STM resolution.

Our experimental system is based on a commercial Omicron LT-STM with a dedicated Ultra High Vacuum (UHV) chamber, and complemented by a preparation chamber designed and assembled by our group [20].

2.2.1 The LT-STM setup

The Omicron LT-STM head (fig. 2.6b) is a single-tube STM: a piezoelectric hollow cylinder, where the tip is fixed at the top, is covered with four electrodes which split the cylinder in four quadrants. By applying suitable voltage difference between the quadrants and the inner electrode, the piezoelectric cylinder can be bent in order to scan the tip laterally onto the sample (xy plane) with sub-angstrom resolution (fig. 2.1). Moreover, the tip can be moved orthogonally to the sample surface (z direction) with a voltage difference applied between the inner and the outer surface of the cylinder.

As discussed in section 2.1.1, the constant current mode is usually used: during the lateral scan, the current is kept constant by using a feedback loop, which changes the z position of the tip in order to follow the local corrugation of the sample.

Since atoms exhibit corrugations of roughly 1 pm to 10 pm, it is critical to have an excellent mechanical stability of the tip-sample junction. Therefore, for mechanical isolation purposes, the STM head can be suspended below the cryostat by means of three springs. Moreover, an eddy current damping system, provides effective, smooth damping of possible low frequency instabilities. The STM head is mounted on a circular plate which is surrounded by copper alloy "U"s (fig. 2.6b) that are centered within radially distributed small magnets, fixed on the inner part of the internal radiation shield: if the STM stage moves, the movement of the copper conductors within the magnets induces eddy currents in the copper alloy, which in

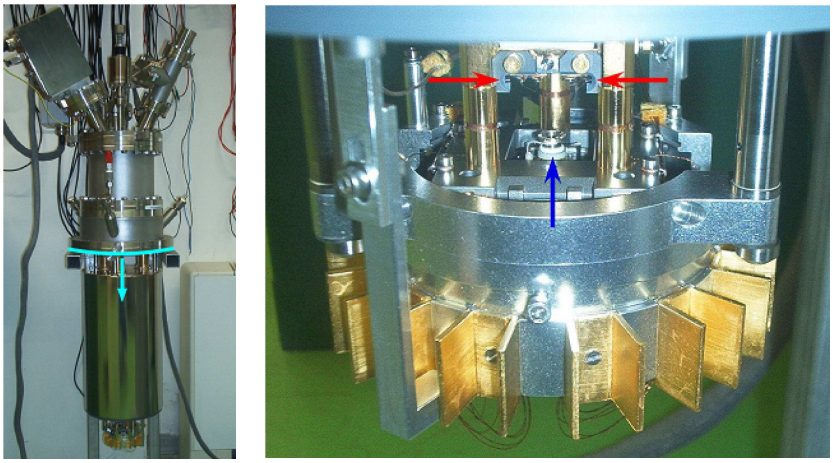

(a) (b)

Figure 2.6: (a) shows the whole LT-STM assembly: the out-of-vacuum part (top part) with the electrical feedthroughs; the blue line indicates the mounting flange and the STM head is visible at the bottom; (b) close-up of the STM head with the slits for inserting and fixing the sample (red arrows) and the top part of the piezoelectric cylinder (blue arrow) where the STM tip is to be fixed.

Table 2.1: Operating temperatures of the LT-STM with the respective cooling methods.

T range	coolant (inner cryostat)
2.5 K <T < 4 K	freezed LHe
4 K <T < 55 K	LHe
55 K <T < 77 K	freezed LN_2
77 K <T< 300 K	LN_2

turn build up magnetic fields that tend to counteract the initial movement of the STM plate.

The operating temperature range of our LT-STM is ideally between 2.5 K and room temperature (RT). To reach temperatures below RT a cooling system made up of two concentric cylindrical cryostats is used (the STM head is fixed below them) and we fill them with cryogenic liquids: liquid nitrogen (LN_2: boiling at 77 K) and liquid helium (LHe: boiling at 4.2 K).

The external cryostat is always filled with LN_2, while the inner cryostat can be filled with LN_2 or LHe according to the desired temperature as described in table 2.1. All the intermediate temperatures can be reached by means of a resistive heater located near the sample stage and powered by a PID temperature controller. The temperature is measured by means of a silicon diode installed behind the sample stage. If no counter-heating is applied, the STM can be kept at 4 K for 24 hours before having to refill the inner cryostat. To reach temperatures as low as 4 K at the sample, the STM head is surrounded by a double shielding mechanism (fig. 2.7a-

(a) (b)

Figure 2.7: The LT-STM radiation shielding: (a) the inner shield which is tightly bolted on the base of the LHe cryostat to ensure a 4 K thermal bath around the STM head; (b) the outer shield is fixed to the base of the LN_2 cryostat.

b), in order to prevent external electromagnetic radiation from limiting the cooling power. A wobble-stick is used to turn the shields in different positions, and it is also used to transfer the samples and the tips from/to the manipulator (see section 2.2.2). All the STM experiments presented in this thesis were performed at 4 K.

2.2.2 The Ultra High Vacuum system

As mentioned in the introduction, if one wants to have an atomically clean surface and to keep it free from contaminants during all the experiment time, it is often necessary to work in Ultra High Vacuum (UHV) conditions [21]. UHV denotes a vacuum regime characterized by pressure lower than 10^{-9} mbar. Moreover, several experimental techniques require vacuum conditions: for example, photoemission experiments (see section 2.3) require vacuum conditions, since at high pressures the emitted photoelectrons would be scattered or absorbed by the gas molecules in the environment. For these reasons, we perform all our experiments in UHV conditions.

The Omicron LT-STM comes with a dedicated UHV chamber equipped with a carousel where tips and samples can be temporarily stored, retrieved and inserted into the LT-STM by means of a wobble-stick. To prevent stray radiation from increasing the final sample temperature, the windows for optical access of the chamber are IR filtered.

The sample preparation chamber, separated from the LT-STM chamber by a gate valve, (see fig. 2.8) is designed around a horizontal manipulator used to position the sample and the STM tip in front of the various instruments. On the manipulator, the sample can be heated up to 1300 K via filament heating and electron bombardment, or cooled down till ~75 K via pumped LN_2 circulation.

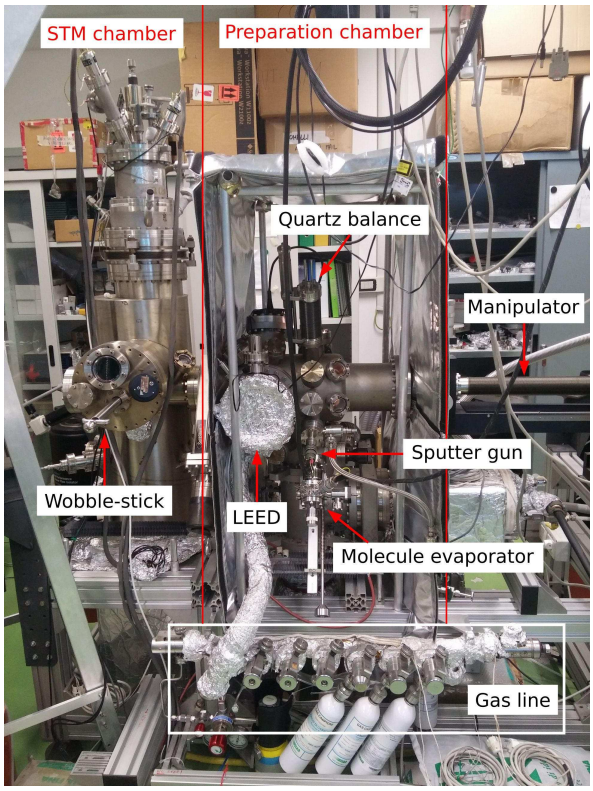

(a) Front view.

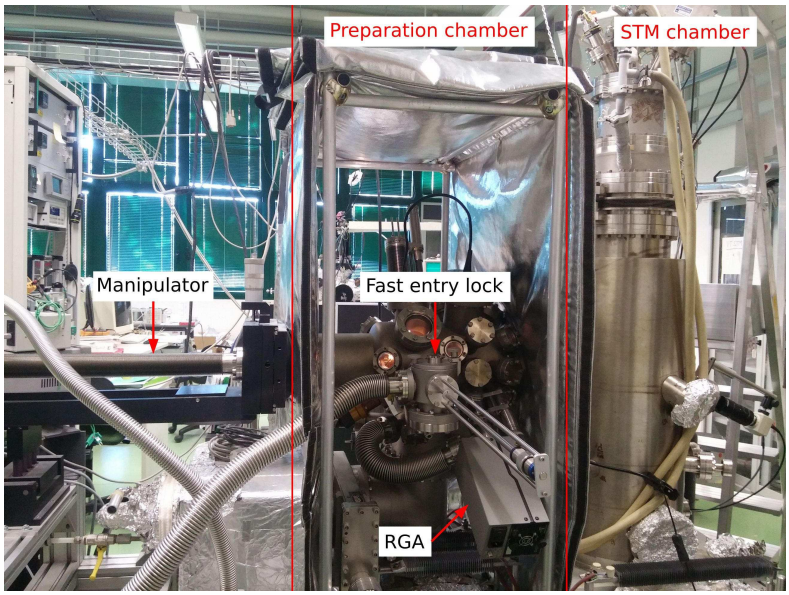

(b) Rear view.

Figure 2.8: Two opposite views of the STM and preparation chamber, showing the position of the various tools and instruments.

The facilities currently available on the preparation chamber are (fig. 2.8):

- a sputter gun, needed in order to clean the samples by bombardment with noble gases (Argon or Neon);
- a residual gas analyzer (RGA), useful for process control and contamination monitoring and for leak testing;
- a Low Energy Electron Diffraction (LEED) system, for a quick structural characterization of the samples prior to the insertion in the STM;
- a molecule evaporator (Kentax) and (eventually) metal evaporators;
- a quartz balance for deposition rate monitoring;
- a gas line, allowing to dose various gases in the chamber background;
- a fast-entry lock system, providing a quick way to insert and extract samples and STM tips from the preparation chamber without breaking the vacuum;

The vacuum is maintained by a 500 l/s ion pump in the STM chamber, whereas the preparation chamber is pumped by a magnetically-levitated turbo pump (450 l/s) together with a smaller ion pump (240 l/s) equipped with a titanium sublimation cartridge and a liquid nitrogen cooled cryopanel. The base pressure in the preparation chamber is about $\sim 1 \div 2 \times 10^{-10}$ mbar, whereas the radiation shields and the cryostats of the LT-STM act as cryo-pumps, ensuring a local lower pressure at the LT-STM head.

2.3 X-ray spectroscopy techniques

2.3.1 X-ray photoelectron spectroscopy (XPS)

XPS is a quantitative spectroscopic technique that measures the elemental composition, empirical formula, chemical state and electronic state of the elements that exist within a material. XPS is widely used in industrial research such as nanotechnology, cosmetics, semiconductor, automotive, agriculture, mining, chemistry and many other fields. XPS is routinely used to determine:

- what elements and the quantity of those elements that are present within the top 1-12 nm of the sample surface;
- what contamination, if any, exists on the surface of the sample;
- empirical formula of a material that is free of excessive surface contamination;
- the chemical state identification of one or more of the elements in the sample and also give information on the local coordination of the atoms;

- the thickness of one or more thin layers (1-10 nm) of different materials within the top 12 nm of the surface;
- the density of electronic states.

A typical XPS spectrum is a plot of the number of electrons detected (Y-axis, ordinate) versus the binding energy (E_b) of the electrons detected (X-axis, abscissa). Each element produces a characteristic set of XPS peaks at characteristic binding energy values that directly identify each element that exist in or on the surface of the material being analysed. Thus XPS has two important properties: chemical and surface sensitivity.

In fact, the photo-electrons binding energies are a clear fingerprint of the chemical elements present in the sample. Moreover, the chemical environment (the chemical bonding, the presence of adsorbates etc...) experienced by the electron prior to the photoemission event affects its E_b, resulting in a characteristic *chemical shift*. For this reason XPS is also known as ESCA (Electron Spectroscopy for Chemical Analysis). A particular kind of chemical shift is the surface core level shift (SCLS), *i.e.* the shift of surface core level electrons with respect to photoelectrons originating from the bulk because of the lower coordination of the top layer atoms: with XPS it is therefore possible to distinguish the surface signal from the bulk one.

The surface sensitivity of XPS is due to the finite inelastic mean free path λ of the photoelectrons. For electrons with intensity I_0 emitted at a depth d below the surface, the intensity I_S of the same electrons as they reach the surface is attenuated as

$$I_S = I_0 e^{-d/\lambda} \tag{2.9}$$

We define *sampling depth* as 3λ so that 95% of all photoelectrons from this depth are scattered by the time they reach the surface. From figure 2.9 it can be seen that, in the energy range from few eV to 1 keV, the electron mean free path in any material is lower than 10 nm and in the 50-100 eV kinetic energy range the mean free path is just few Å: this means that photoelectrons in this kinetic energy range mostly originate form the first few layers of the solid. For this reason XPS is widely used for studying thin films and molecular adsorbates.

Theoretical aspects

XPS is based on the photoemission process: the spectra are obtained by irradiating a material with a X-ray beam while simultaneously measuring the kinetic energy (with a proper detector) and the number of electrons (photoelectrons) that escape from the top 1 to 10 nm of the material being analyzed (fig. 2.10).

The photoemission process takes place when a highly energetic photon interacts with matter, removing one electron from an atomic orbital or from an energy band; this electron then reaches the vacuum level and can be measured by a detector. Soft X-rays are used in general to probe the core levels of a solid.

When a photoemission takes place (see fig. 2.11), the photon transfers its energy $h\nu$ to the photoelectron which leaves the sample with a kinetic energy E^s_{kin}

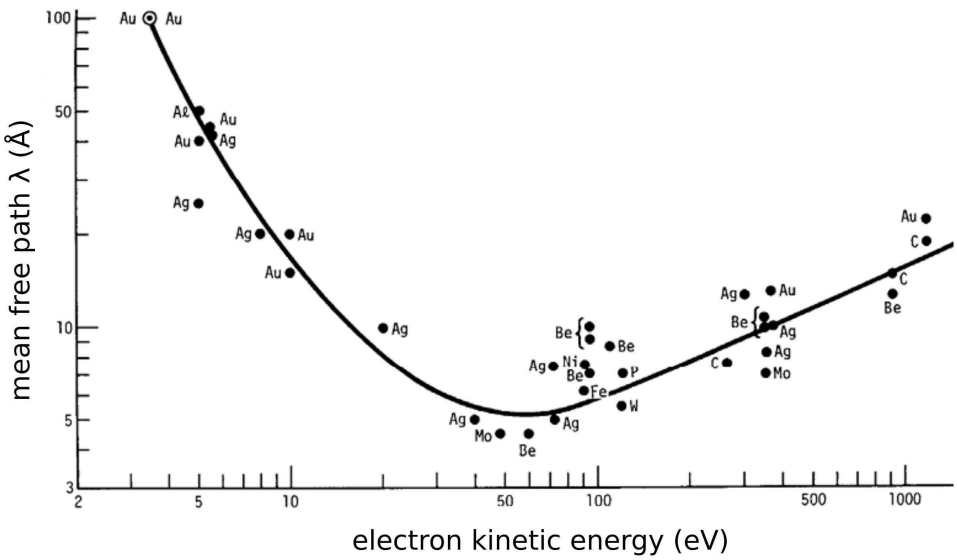

Figure 2.9: Universal curve of the electron inelastic mean free path: the curve is roughly valid for all the materials.

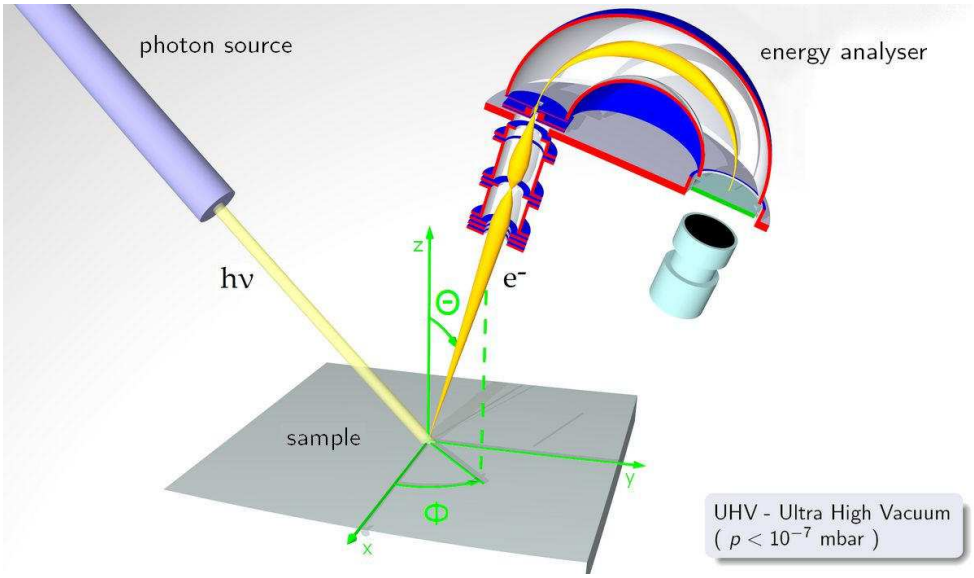

Figure 2.10: The basic scheme of a XPS experimental configuration. Image from [7].

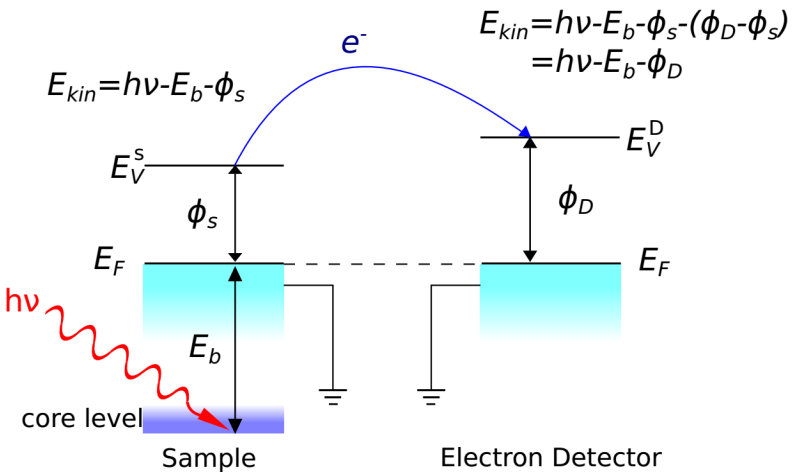

Figure 2.11: Energy diagram of the photoemission process for a core electron.

equivalent to the difference between the energy ($h\nu$) gained from the photon and the energy lost to overcome its binding energy E_b, whose reference is conventionally taken with respect to the Fermi level ($E_F \equiv 0$), and the work function ϕ_s of the sample:

$$E^s_\mathrm{kin} = h\nu - (E_\mathrm{b} + \phi_s) \tag{2.10}$$

then, the photoelectron reaches the detector and has to overcome the work function ϕ_D of the detector, which is grounded as the sample to have the same Fermi level:

$$\begin{aligned} E_\mathrm{kin} &= h\nu - (E_\mathrm{b} + \phi_s) - (\phi_D - \phi_s) \\ &= h\nu - E_\mathrm{b} - \phi_D \end{aligned} \tag{2.11}$$

Therefore, the equation (2.11) gives the kinetic energy of a photoelectron detected the electron detector [22]. Finally, we obtain the electron binding energy:

$$E_\mathrm{b} = h\nu - (E_\mathrm{kin} + \phi_D) \tag{2.12}$$

XPS spectra

The intensity I^p_i of a peak "p" of a selected element "i" in a XPS spectrum can be expressed [22] as

$$I^\mathrm{p}_\mathrm{i} = N_\mathrm{i}\sigma_\mathrm{i}\lambda_\mathrm{i}K \tag{2.13}$$

where N_i is average atomic concentration of element "i" on the surface under analysis, σ_i the photoelectron cross-section for element "i" as expressed by peak "p", λ_i the inelastic mean free path of a photoelectron, and K includes all other factors related

to experimental set-up such as the incident X-ray photon flux and the detection efficiency of the detector.

In a real photoemission experiment, the E_b of the core electron in its ground state cannot be directly probed since the measured E_b incorporates both initial state and final state effects, and the spectral linewidth is broadened by both intrinsic and experimental effects. In general the total spectral broadening [23] can be written as

$$\Delta E = \sqrt{\Delta E_{nat}^2 + \Delta E_{vib}^2 + \Delta E_{in}^2 + \Delta E_{h\nu}^2 + \Delta E_a^2} \tag{2.14}$$

where

- ΔE_{nat} is the intrinsic natural linewidth directly related to the core-hole lifetime τ via the Heisenberg indetermination principle $\Gamma\tau \geq \hbar$. The photoemission event leaves the atom in a highly excited core ionized state, from which it can decay radiatively (fluorescence) or non-radiatively (typically by *Auger* decay).
- ΔE_{vib} is due to the vibrational component produced by the excitation of low energy vibrational modes both in the initial and in the final state.
- ΔE_{in} is the inhomogeneous broadening than can originate from the presence of unresolved core level components in the spectrum.
- $\Delta E_{h\nu}$ is caused by the non perfect monochromaticity of the photon beam (experimental contribution).
- ΔE_a is due to the limited resolving power of the electron analyser (experimental contribution).

For ΔE_{nat}, assuming an exponential decay probability for the core hole in the time domain ($\propto exp(-t/\tau)$), the spectral function will have a Lorentzian shape given by:

$$I_L(E) = \frac{I}{\pi} \frac{\Gamma/2}{(E - E_b)^2 + (\Gamma/2)^2} \tag{2.15}$$

where Γ is the FWHM (Full Width at Half Maximum) of the Lorentzian peak. A Gaussian broadening is used to account for the other terms of eq. (2.14):

$$I_G(E) = \frac{I_o}{\gamma\sqrt{2}} \exp\left(-\frac{(E - E_b)^2}{2\gamma^2}\right) \tag{2.16}$$

An accurate description of the lineshape of the photoemission peaks was formulated by S. Doniach and M. Sunjic [24], who elaborated a modified Lorentzian distribution function by including an asymmetry parameter α, which basically accounts for the excitation of electron-core hole pairs at the Fermi level. The Doniach-Sunjic lineshape is expressed as:

$$I_{DS} = I_0 \frac{\Gamma_E(1-\alpha)}{[(E-E_b)^2 - (\Gamma/2)^2]^{(1-\alpha)/2}} \xi(E) \tag{2.17}$$

where Γ_E is the Euler Gamma function, and

$$\xi(E) = \cos\left[\frac{\pi\alpha}{2} + (1-\alpha)\arctan\left(\frac{E-E_b}{\Gamma/2}\right)\right]$$

The XPS spectra presented in this thesis are fitted using a Doniach-Sunjic profile or a Voigt profile, which is a convolution of a Lorentzian profile and a Gaussian profile.

XPS instrumentation

As shown in figure 2.10, the fundamental parts of a XPS experimental set-up are a source of X-rays, an electron energy analyser (detector) and an UHV chamber.

UHV condition (or at least high vacuum) is required because the electrons must reach the detector, and their mean-free path is too short at high pressures. However, we point out that recently high pressure (*i.e.* up to 10 mbar) XPS has been developed [25] since, for instance, many chemical reactions take place in atmospheric conditions, and therefore a higher pressure experimental system would be desirable for investigating such systems.

The X-ray source can be a conventional laboratory aluminium K_α X-rays or non-monochromatic (polychromatic) magnesium X-rays, or it can be a synchrotron light source. By synchrotron radiation we mean the light generated by relativistic electrons when they are accelerated on a curved trajectory and thus emit a highly collimated photon beam in the tangential direction. The description of the details of synchrotron radiation is beyond the scope of this thesis. However, it is widely treated in literature, for details one can refer to books like ref. [26]. The synchrotron radiation is preferable to conventional sources, for many reasons:

- synchrotron radiation is tunable, so that a wide range of photon energies is accessible by properly adjusting the undulator gap and the monochromator;
- it yields a high brilliance, *i.e.* a high photon flux with a narrow bandwidth;
- it yields a high polarization of the photon beam.

Thanks to these properties, XPS measurements with a synchrotron radiation X-ray source have higher sensitivity to elemental composition, structural and chemical sensitivity, surface sensitivity and faster spectra acquisition.

The electron detector is generally a hemispherical electron energy analyzer (as in our experiments) because of its higher resolution with respect to other types of detector. An ideal hemispherical analyzer consists of two concentric hemispherical electrodes (inner and outer hemispheres of radius R_1 and R_2 respectively) held at proper voltages V_1 and V_2 (see fig. 2.12).

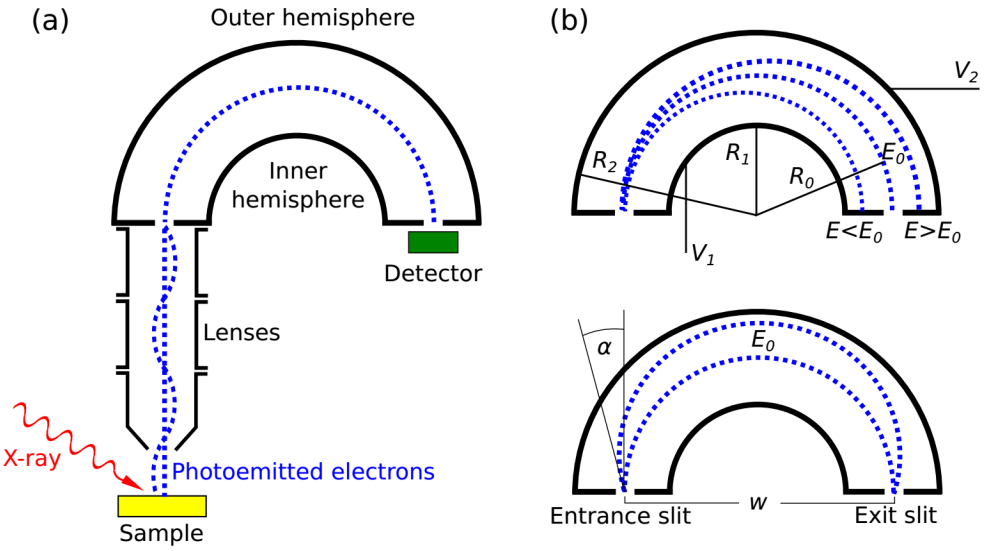

Figure 2.12: The hemispherical electron energy analyzer. (a) Basic scheme. (b) Some details with the main parameters.

It is possible to demonstrate that in such a detector, (i) the electrons are linearly dispersed along the direction connecting the entrance and the exit slit, depending on their kinetic energy, while (ii) electrons with the same energy are first-order focused [27] (fig. 2.12b). This property is used to select the electron energy to detect: only the electrons with a energy E_0 (the so-called *pass energy*) will follow the trajectory of radius $R_0 = (R_1 + R_2)/2$ and then reach the detector at the exit slit, and E_0 is given by

$$E_0 = \frac{e(V_2 - V_1)}{2R_0} \left(\frac{1}{R_1} - \frac{1}{R_2} \right)^{-1} \tag{2.18}$$

where e is the elemental electron charge. The instrumental resolution ΔE is

$$\Delta E = E_0 \left(\frac{w}{2R_0} + \frac{\alpha^2}{4} \right) \tag{2.19}$$

where w is the average width of the two slits, and α is the incidence angle of the incoming photoelectrons (fig. 2.12b). Although the resolution improves with increasing R_0, technical problems related to the size of the analyzer put a limit on the actual value of R_0. Although a low pass energy E_0 improves the resolution, the electron transmission probability is reduced at low pass energy, and the signal-to-noise ratio deteriorates, accordingly. The electrostatic lenses in front of the analyzer (fig. 2.12a) have two main purposes: they collect and focus the incoming photoelectrons into the entrance slit of the analyser, and they decelerate the electrons to the kinetic energy E_0, in order to increase the resolution. When acquiring XPS spectra in *sweep* (or *scanning*) mode, the voltages of the two hemispheres and hence the pass energy are held fixed; at the same time, the voltage applied to the electrostatic lenses is

swept in such a way that each channel counts electrons with the selected kinetic energy for the selected amount of time.

2.3.2 Near edge X-ray absorption fine structure (NEXAFS)

When the X-ray energy is scanned through the binding energy of a core shell, there is an abrupt increase in absorption cross-section. This gives rise to a so-called absorption edge, with each edge representing a different core electron binding energy [28]. The edges are named according to the principal quantum number of the electron that is excited: K for $n = 1$, L for $n = 2$, M for $n = 3$, etc. Due to angular momentum and spin-orbit splitting, the edges split into further more edges like L_1 ($2s$), L_2 ($2p_{1/2}$), L_3 ($2p_{3/2}$) for the L edge (fig. 2.13). X-ray absorption spectroscopy (XAS) refers to the measurement of X-ray absorption cross-section in the vicinity of one or more absorbing edges.

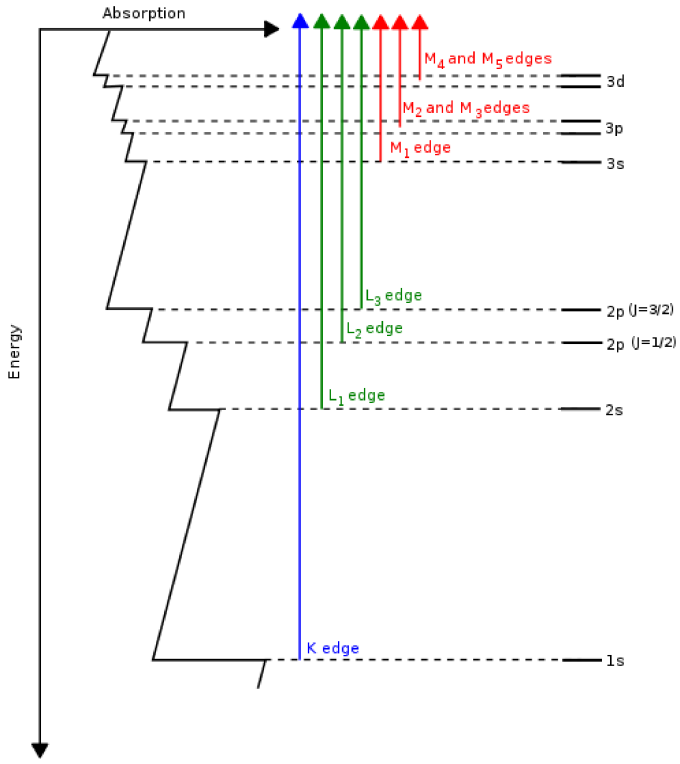

Figure 2.13: Schematic illustration of the transitions that contribute to XAS edges. Image from [7].

Absorption of an ionizing X-ray results in photoelectron ejection, leaving behind a highly excited core-hole state which tends thus to recombine. This can relax by a variety of mechanisms, with the two most important being emission of an Auger electron and X-ray fluorescence (fig. 2.14).

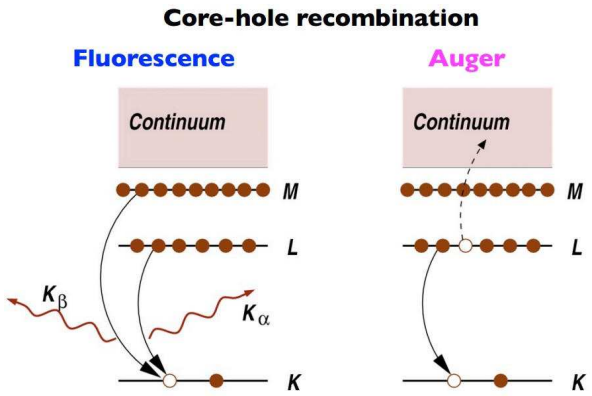

Figure 2.14: Schematic illustration of the two main core-hole recombination processes. Image from [29].

From the experimental point of view, the XAS spectra can be recorded in transmission mode, measuring the intensity of the incident (I_0) and transmitted (I_t) radiation obtaining thus an absorption $A \propto -\ln(I_t/I_0)$, or in fluorescence mode, measuring the fluorescence excitation radiation intensity (I_f) obtaining an absorption $A \propto I_f/I_0$. The fluorescence mode is the most common one because the transmitted intensity is generally rapidly absorbed by the common samples.

Conventionally the XAS spectrum is divided into two regions (fig. 2.15). The structure in the vicinity of the edge is referred to as X-ray Absorption Near-Edge Structure (XANES) or equivalently as Near Edge X-ray Absorption Fine Structure (NEXAFS): the two acronyms should be interchangeable but over the years NEXAFS has become terminology for low Z (atomic number) elements like C, N, O... [30]. Since in this thesis we will present only C, N, and O edges, we call it NEXAFS. The oscillations above the edge, which can extend for 1000 eV or more, are referred to as Extended X-ray Absorption Fine Structure (EXAFS). The distinction between NEXAFS and EXAFS is formally arbitrary, since the same fundamental physical principles govern photoabsorption over the entire XAS region and there is no unambiguous definition that distinguishes between "near-edge" and "extended" structure [28]. However, in practice, the subdivision of these two regions is important because the dominant physical processes are different, and they can give different types of information about the analyzed sample.

NEXAFS

In this thesis we present some NEXAFS measurements, and therefore in this section we give a brief description of this technique.

The NEXAFS region, as shown in figure 2.15, is clearly more complex than simply an abrupt increase in absorption cross-section. There are several weak transitions below the edge (pre-edge transitions) together with structured absorption on the high energy side of the edge. Thus, we can further subdivide the NEXAFS

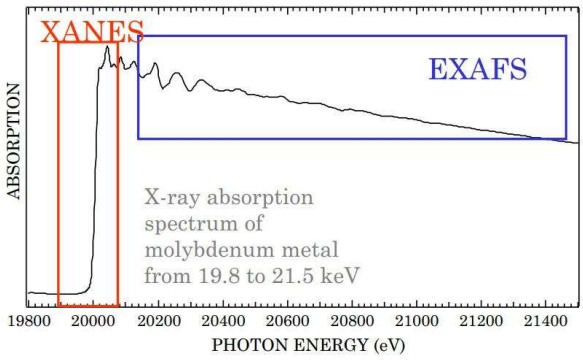

Figure 2.15: A X-ray absorption spectrum, showing the structured absorption that is seen both within ca. 50 eV of the edge (XANES) and for several hundreds eV above the edge (EXAFS). Image from [30].

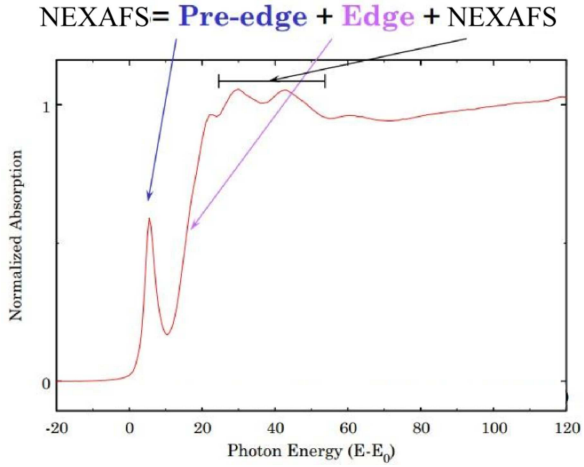

Figure 2.16: A NEXAFS spectrum subdivided into the pre-edge, edge and NEXAFS range. Image from [30].

spectrum into three parts, as indicated in figure 2.16.

Each region has different physical processes involved, and gives different types of information about the sample [30]:

- The pre-edge region features are caused by electronic transitions to empty bound states. The transition probability are controlled by dipolar selection rules. From this region we can obtain information about the local geometry around absorbing atom and information on oxidation state and bonding characteristics (chemical shift).
- The edge region defines ionization threshold to continuum states. This region depends on oxidation state (chemical shift) too, with the main edge shifting to higher energies with increased oxidation state.

- The NEXAFS region is dominated by multiple-scattering resonances of the photoelectrons ejected at low kinetic energy. From this region we can obtain information about the atomic position of neighbors: interatomic distances and bond angles.

Angular dependence of NEXAFS

By employing synchrotron radiation as X-ray source, we can not only acquire standard XAS spectra, but we can also perform polarization dependent measurements. In particular, in some works presented in this thesis, we performed linear dichroism NEXAFS measurements to investigate the orientations of the molecules adsorbed on Au(111).

Stöhr and Outka in their work published in 1987 [31] presented a model for recognizing the molecular orientations on surfaces from the angular dependent NEXAFS spectra. They observed that, in the K-shell (1s) NEXAFS spectra for chemisorbed molecules on surfaces, generally only the transitions to highly localized molecular π^* and σ^* orbitals are not severely perturbed by the interaction with the surface, and therefore they are the main features of the NEXAFS spectra. These π^* and σ^* orbitals are directionally oriented.

Stöhr and Outka demonstrated rigorously their model which gives quantitative results. The detailed description of this model is beyond the scope of this thesis, and can be found in the original article [31]. Here we just give only a very brief explanation of the angular dependent NEXAFS.

The well-defined symmetry of the initial (1s) and the final (π^* and σ^*) states involved in the electronic dipole transitions and the nearly linearly polarized nature of synchrotron radiation are responsible for the strong angular dependence of the resonance intensities. The dipole selection rules dictate that the σ^* resonance is largest when the electrical field vector **E** is along the σ^* orbital, and zero when **E** is perpendicular to the σ^* orbital. The same rules hold for π^*. Therefore, we can change **E** direction (which is perpendicular to the X-ray beam direction) to probe the direction of the π^* and σ^* orbitals. Generally, two different angle measures are enough to understand the bond orientation: a normal **E** (90°, named p polarization) and a grazing **E** (0°, named s polarization) spectrum.

2.3.3 The ALOISA beamline

All our photoemission experiments were performed at the ALOISA (Advanced Line for Overlayer, Interface and Surface Analysis) beamline or at the ANCHOR laboratory at the Elettra synchrotron facility located in Basovizza (Trieste - Italy).

ALOISA [32] is a multipurpose beamline at the Elettra synchrotron facility (in Trieste, Italy) dedicated to the chemical and structural characterization of surfaces, adsorbates and ultra-thin films. The ultra-wide energy range of the beamline and the complete set of detectors in the end-station, allow the users to combine *in-situ* structural and chemical investigation techniques, such as:

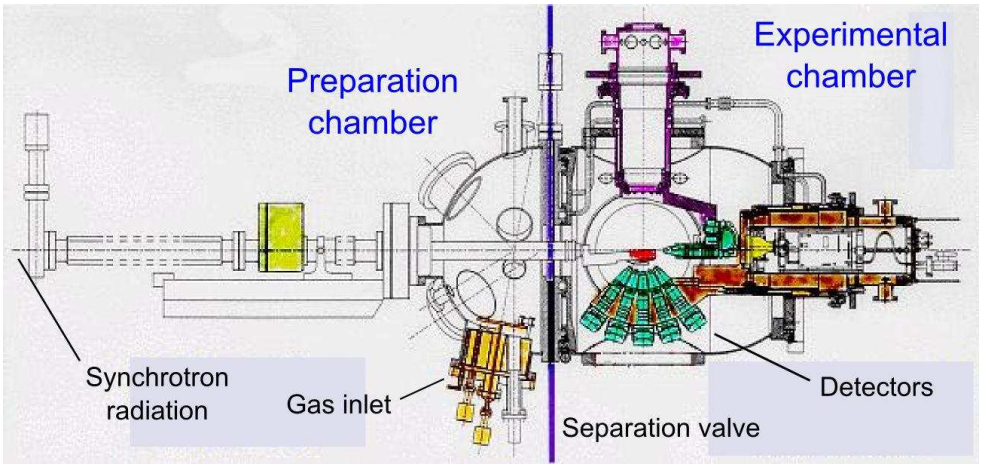

Figure 2.17: The ALOISA chamber. Image from [32].

- X-ray Photoemission Spectroscopy (XPS)
- Near Edge X-ray Absorption Fine Spectroscopy (NEXAFS)
- Photoelectron Diffraction (PED)
- Resonant X-ray Photoemission Spectroscopy (RESPES)
- Resonant X-ray Photoelectron Diffraction (RESPED)
- Surface X-Ray Diffraction (SXRD)
- Auger-Photoelectron Coincidence Spectroscopy (APECS)

A grating-crystal monochromator is employed to cover a wide photon energy range spanning 130 – 1500 eV.

The experimental workstation (fig. 2.17) consists in two UHV chambers separated by a valve: the preparation chamber for the sample cleaning and preparation and the experimental chamber surrounded by a μ-metal shielding to screen the sample from stray magnetic fields which would deflect the electron trajectories. The preparation chamber is equipped with a gas inlet system for the gas doses. The experimental station is equipped with a combination of electron spectrometers and energy-resolved photodiodes for detecting both electrons and photons. The whole set of different detectors is hosted onto rotating frames inside the experimental chamber in order to perform complementary measurements in UHV conditions.

The ANCHOR laboratory

The ANCHOR laboratory [33] has been set up on the brenchline of the ALOISA beamline. The apparatus permits to perform the *in-situ* growth and analysis of thin

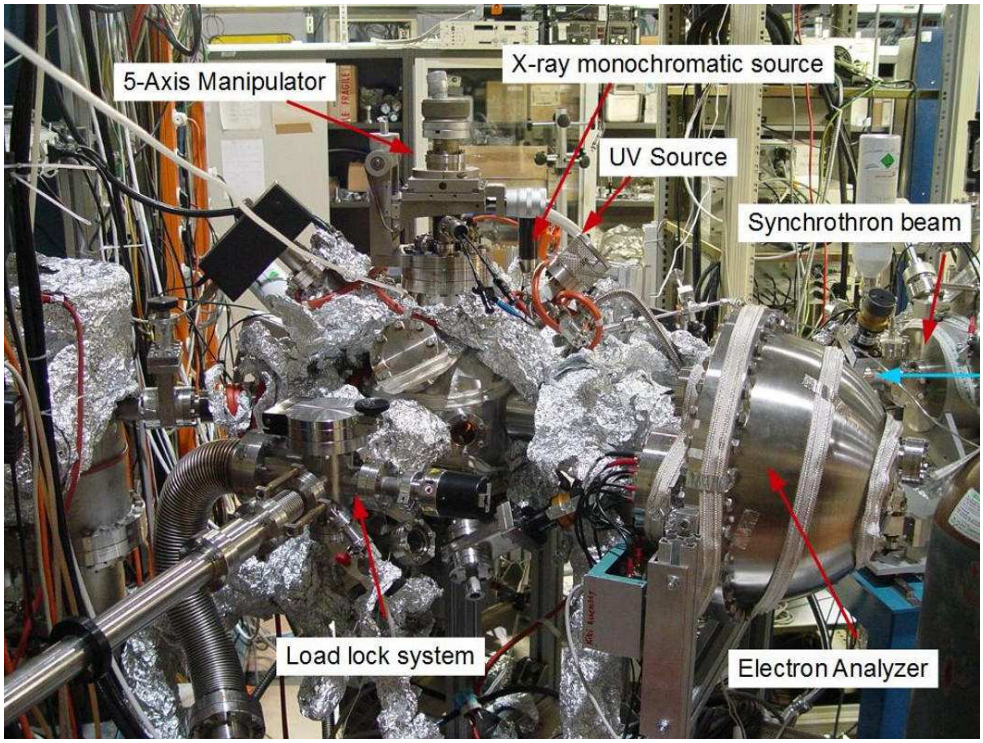

Figure 2.18: The ANCHOR laboratory.

organic films. High resolution XPS, UPS (Ultraviolet Photoelectron Spectroscopy) and NEXAFS experiments can be combined for a complete spectroscopic characterization of the samples.

The chamber is equipped with a monochromatic X-ray source (Omicron XM100), a 120 mm Electron Analyzer (PSP Vacuum - Resolve 120), a Helium Lamp (VG) (the UV source for UPS experiments), and a 5 axis manipulator (VG) (fig. 2.18). The chamber is connected to the brenchline of tha ALOISA beamline so that synchrotron light can be provided in the for variable photon energy measurements (NEXAFS and high resolution XPS). The sample is mounted on a variable temperature (200 – 900 K) sample holder and load lock system is present for fast sample replacement.

Part I

The role of the substrate in the formation of organic 2D structures on Au(111)

Chapter 3

Trapping of charged gold adatoms by dimethyl sulfoxide on a gold surface

The ability to control the structural and electronic properties of (hetero)-organic assemblies on metal surfaces is the key issue for the design of efficient devices in organic electronics, which has triggered a significant effort in the recent years in this field [34–37]. Gold single crystal terminations are often adopted for their inertness to support the growth of 2D supramolecular architectures. In particular, on the Au(111) substrate, when suitable tectons [38] are used, the molecule-substrate coupling is relatively weak, and manifold synthons [39] involving noncovalent [40–43] or metal-organic [44–48] interactions have been exploited to program the desired properties of the final architectures. Moreover, the (111) face of gold is the most stable one, and molecular interactions on and with this substrate are of great importance since in most applications, where polycrystalline gold electrodes or clusters are involved, (111)-terminated facets predominate [3, 4].

Despite being inert ("noble") in its bulk form, gold exhibits rich catalytic properties and ligand chemistry when in the form of small clusters composed by tens of atoms down to single atoms, where gold is undercoordinated with respect to its bulk form [49, 50]. The interest in nanogold chemistry has seen a significant upswing only in the last decades, and nowadays reaches well beyond fundamental research, finding valuable applications ranging from real catalysts for oxidation reactions up to radiosensitization agents in cancer therapy [51, 52]. In particular, heterogeneous catalysts based on highly dispersed gold have been widely investigated, and a remarkable understanding of the structure-activity relationship at the nanoscale, as well as of the role of the catalyst support, has been achieved in the last 20 years [49, 53–55].

At the intersection between these two seemingly opposite worlds, *i.e.*, the inertness of gold substrates and the nanoscale reactivity of gold clusters, an exciting route opens up to novel binding motifs that can encode specific properties of the

supramolecular assemblies, based on gold adatoms as molecular linkers. In fact, on the Au(111) surface, low-coordinated atoms are natively available, since the higher density of gold atoms in the first atomic layer induces a periodic displacement of the atoms out of the surface plane along the soliton walls of the herringbone reconstruction [56, 57]. On this surface, extraction and stabilization of native gold adatoms can be induced by interaction of organic molecules with the Au(111) surface, as observed for instance with molecules containing cyano (CN) groups [47, 48, 58], organophosphorus compounds [59, 60], porphyrin or phthalocyanine derivatives [61–63], and molecules containing very electronegative substituents such as chlorine [64] or sulfur [65, 66]. Apart from thiols (R-SH), which are known to induce deep restructuring of the gold surface by covalently binding to this substrate [67–71], to our knowledge there are only few examples where 2D or 1D supramolecular architectures are stabilized by native gold adatoms as linkers. In these cases, the Au adatoms appear to play the well-known role of transition metal linkers, where reported substituents are often distinctively electronegative [34, 72, 73]. An alternative linkage method that has been recently explored involves alkali metal linkers [74]. Together with providing tunable interfacial electronic properties [75], they also allow more flexible bonding geometries due to the ionic character of the metal-molecule interaction, in contrast to the directional coordination enforced by the shape of the transition metal d orbitals [34, 46]. Gold can be seen as a half-filled s shell element, in analogy to alkali metals: this suggests the idea that undercoordinated gold adatoms could also display ionic behavior, particularly when interacting with polarized but neutral molecules, although this has not been reported to date. However, the observation of such ionic gold linkers by STM experiments could be hindered by the small ionic radius of oxidized Au, and by the Au linker adatoms being possibly located below the plane of the molecular adsorbates and thereby hidden.

In this Chapter, we show how we can substantiate this physical picture by depositing on a gold surface a very simple polar molecule, dimethyl sulfoxide (DMSO - see figure 3.2). By means of XPS and NEXAFS, and by extensive STM measurements of DMSO on Au(111) from multilayer to sub-monolayer molecular coverages, we show how the adsorption of this molecule is characterized by the formation of characteristic molecular complexes composed of three or four DMSO molecules. The latter appear in the STM images to be linked through their negatively charged, and thus presumably mutually repelling, terminations. This puzzling supramolecular structure has been rationalized by comparing the experimental STM images with simulated ones, obtained by DFT calculations. As it will be shown, our results clearly indicate that the majority of the observed complexes can be accurately reproduced if and only if the negatively charged oxygen terminations are linked by one or two Au adatoms, which are "invisible" in the STM images.

This work, where I contributed with most of the STM experiments and part of the XPS and NEXAFS experiments, has been published as Feng *et al.* [76] in *ACS Nano*.

3.1 The Au(111) surface structure

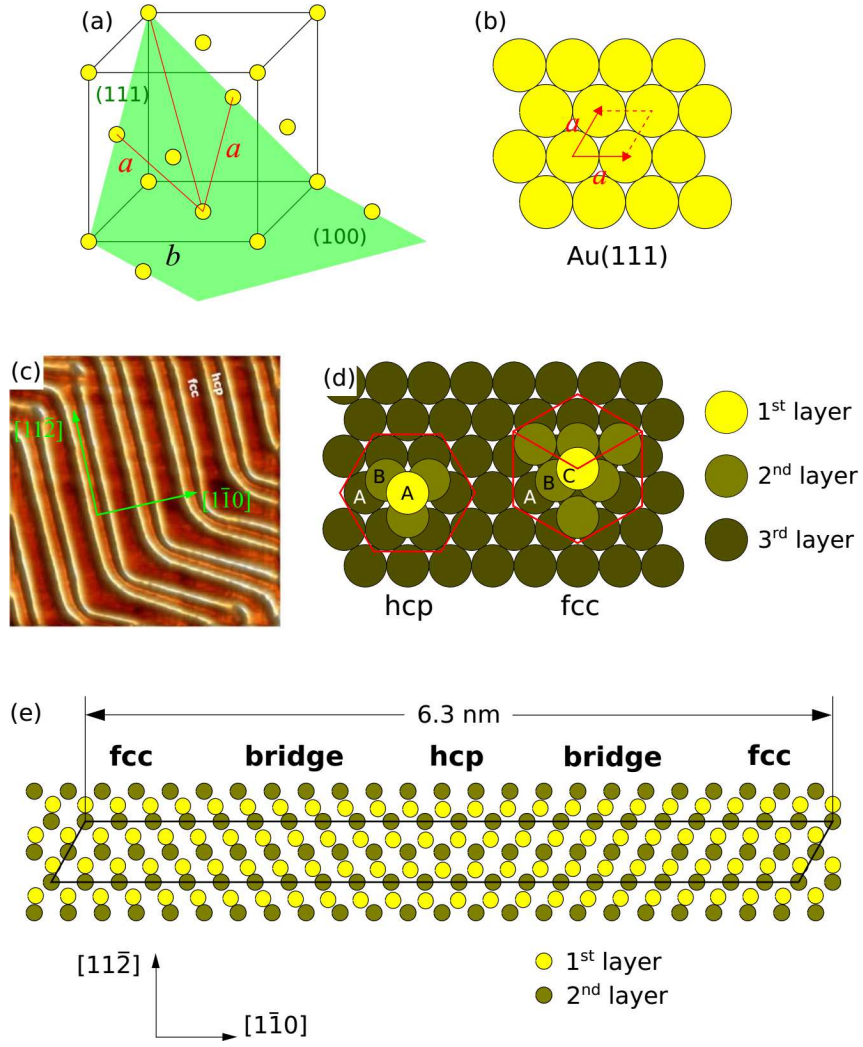

Figure 3.1: The gold crystal structure and its (111) surface. (a) 3-dimentional model of the gold crystal structure, where b = *fcc* lattice parameter, and (b) a = Au(111) lattice parameter. (c) A STM image (35.6×35.6 nm^2) underling the *fcc* and *hcp* regions. The bright strips are the bridge stacking regions. (d) Model showing the difference between the *hcp*(ABA) and *fcc*(ABC) close packing. (e) Model for the herringbone Au(111) reconstruction: a $(23 \times \sqrt{3})$ unit cell is drawn. Along the [1$\bar{1}$0] direction there are 23 gold atoms of the first layer for 22 atoms of the second layer. The first layer goes from *fcc* to *hpc* through regions with bridge sites.

Because of its relevance in the technological applications (as mentioned in the introduction), the Au(111) sample will be used as substrate the supramolecular assemblies in all the works presented in this thesis. Therefore, here we give a description of the Au(111) surface structure.

Gold has a face centered cubic (*fcc*) crystal structure, as showed in figure 3.1a. The lattice parameter is $b = 0.408$ nm, thus the lattice parameter of the two-dimensional (111) surface is $a = b/\sqrt{2} = 0.288$ nm (fig. 3.1a, b). Ideally, the structure of a surface cut through a specific crystallographic plane should preserve the bulk structure. However, in the real case, for many metals the surface can reconstruct. In this sense, the (111) surface of gold is a unique case since it is the only *fcc* metal that reconstructs on its (111) surface [57]. This reconstruction takes the form of a $23 \times \sqrt{3}$ "herringbone" structure which can be easily recognized on STM images by the presence of stacking fault lines (also called discommensuration lines) exhibiting a noticeable corrugation on the surface (fig. 3.1c). The herringbone structure is consequence of the competition between the tendency of Au surface layer to contract to higher surface density to minimize the energy, and the substrate (bulk gold) that tends to keep the top layer in registry with the underlying atomic layers. The contraction, which induces a corrugation of about 0.15 Å[77], takes place because it is strong enough to overcome the potential due to the substrate. It is experimentally demonstrated that the compression gives rise to regions where the stacking changes from *fcc*(ABC) to hexagonal close-packed *hcp*(ABA) (fig. 3.1d, e). Moreover, a secondary structure, [57] where the *fcc-hcp* stripes bend every $\sim$ 30 nm, originate from the herringbone reconstruction (fig. 3.1c).

Theoretical calculations are in agreement with the experimental data. Takeuchi and coworkers [78] calculated from first principles the Au(111) structure, finding good agreement with the experimental results in literature: the *hcp* site is only 1 mRy higher in energy than *fcc* site, thus they are almost degenerate in energy and can pass from one site to the other easily through regions with a bridge site which has only 3 mRy higher energy than an *fcc* site. They found that the top layer contracts about 5% along the $[1\bar{1}0]$ direction, which is compatible with the experimental 4.3% (fig. 3.1e). Note that the surface does not contract in the $[11\bar{2}]$ direction, since some surface atoms would have to climb above the top site, which is energetically very unfavourable since they found the top site to have 14 mRy higher energy than *fcc* site. From figure 3.1c, it's also clear that *fcc* regions are wider than *hcp* ones, and this is consistent with the fact that the *hcp* sites have a slightly higher energy (1 mRy) than *fcc* ones. Since Au(111) has three equivalent directions $[1\bar{1}0]$, there are three equivalent domains rotated by $\pm 120^\circ$ separated by domain boundaries.

In all the sample preparations of the experiments presented in this thesis, the Au(111) surface is cleaned in UHV by repeated Ne^+ or Ar^+ sputtering at 500 eV at room temperature for 10–20 min followed by annealing at 773–873 K for 10–20 min (usually one cycle of sputtering and annealing is enough). Then, the molecule(s) of interest are deposited by evaporation on the clean Au(111) substrate.

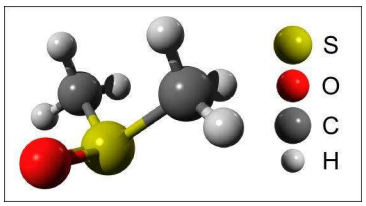

Figure 3.2: Ball and stick model of the DMSO molecule (yellow: sulfur, red: oxygen, grey: carbon, white: hydrogen).

3.2 The DMSO molecule

DMSO is constituted by a sulfinyl (S=O) group and two methyl (CH_3) groups bound to the sulfur atom (figure 3.2), and it is characterized by a large dipole moment (3.96 D) [79]. DMSO is an aprotic solvent, produced as a byproduct of the paper industry and widely employed both in laboratory and in industrial processes. It finds numerous applications in the electronics industry [80, 81], in biology and medicine as a radio- and cryo-protective agent for cells and tissues [82], as well as a percutaneous drug penetration enhancer [83].

DMSO (Sigma-Aldrich, anhydrous, $\geq$ 99%), was dosed on the Au sample by backfilling the UHV chamber through a leak valve connected to a glass vial, where DMSO was transferred under nitrogen atmosphere to prevent water contamination. Before dosing in the UHV chamber, DMSO was thoroughly cleaned by means of several freeze-pump-thaw cycles. The DMSO adsorption phases were prepared by exposing the sample held at 153 K to a background pressure of DMSO of about 4×10^{-6} Pa for about 15 s. This preparation consistently yielded a multilayer phase. Monolayer and sub-monolayer phases were then prepared by simply heating the multilayer phase or by dosing at saturation at a specific sample temperature. We verified that no difference could be observed in the final surface by using the two alternative preparation methods.

3.3 DMSO on Au(111): monolayer

To our knowledge, only very few experimental works have characterized the adsorption of DMSO on metal surfaces, in UHV[84–87] or in solution [85, 88, 89] environments. In particular, on Au(100) and Au(111), the structural properties of the DMSO-gold interface have been probed by STM, but only tentative models were put forward on the basis of poorly resolved features in the STM images [85, 90].

To characterize the adsorption of DMSO on Au(111), we studied by LT-STM films obtained by depositing the molecules at different temperatures T_s of the Au(111) sample in the $153 < T_s < 300$ K range. Due to the weak bonding of the molecules in the multilayer, STM imaging could not be carried out on this phase. Conversely, upon annealing of the multilayer phase at 193 K, a high coverage, compact phase is obtained and, where the compact phase starts to break apart, it exhibits regions

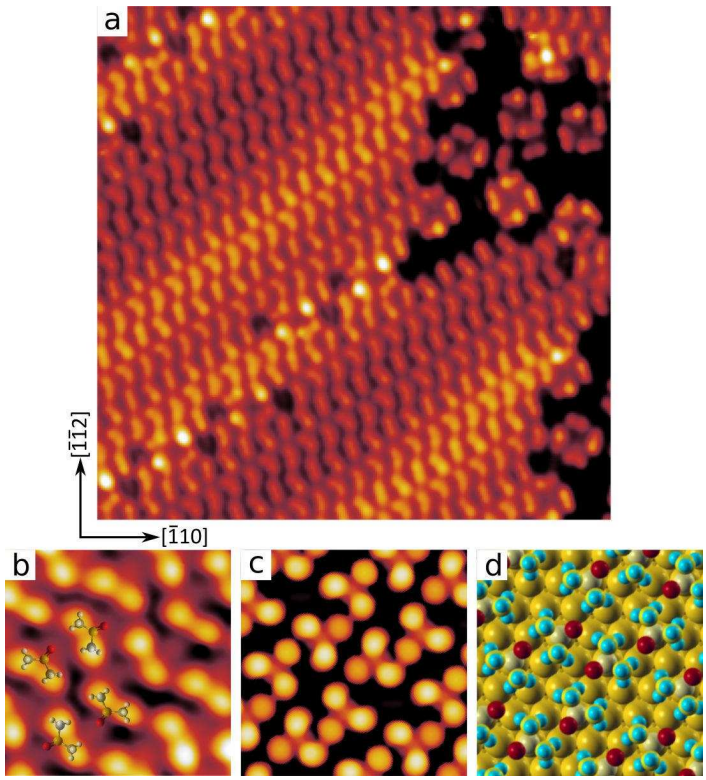

Figure 3.3: (a) Experimental STM image (12.75 × 12.75 nm²) showing the high coverage phase (left part of the image), coexisting with patches of square complexes (on the right), and (b) a high resolution detail of the high coverage phase, where transparent ball and stick models are superimposed to guide the eye in the identification of the single molecules (2.14× 2.14 nm²). (c) DFT-based simulated STM image of this phase, and (d) the corresponding ball model. Image parameters: (a) V_s = 100 mV, I_t = 100 pA, (b) V_s = 50 mV, I_t = 200 pA.

where *square* complexes begin to form, as it is shown in figure 3.3a. The *square* complexes will be discussed hereafter, while first we focus on the compact phase.

From the high-resolution inset (fig. 3.3b) supported by the superimposed stick and ball models, the features corresponding to the molecular structure of DMSO can be straightforwardly identified: there are two brighter protrusions which correspond to the methyl groups, whereas the less intense one can be assigned to the oxygen atom. The appearance also suggests that the molecule is sitting in an "inverted umbrella" geometry, *i.e.* with the S atom directly interacting with the Au surface. In the compact phase, the orientation of molecular rows is found to be approximately ±15° with respect to the directions of the herringbone reconstruction (the [11$\bar{2}$] directions). By measuring the distance between the molecules, it is possible to define the unit cell of the molecular structure, which is described by the $\vec{b}_1$ and $\vec{b}_2$ vectors in the following matrix notation:

$$\begin{pmatrix} \vec{b}_1 \\ \vec{b}_2 \end{pmatrix} = \begin{pmatrix} 3 & 1 \\ -1 & 6 \end{pmatrix} \begin{pmatrix} \vec{l}_1 \\ \vec{l}_2 \end{pmatrix}$$

with the Au(111) unit cell vectors being defined as $\vec{l}_1 = a_0(1;0)$ and $\vec{l}_2 = a_0\left(\frac{1}{2};\frac{\sqrt{3}}{2}\right)$, and a_0 the nearest neighbor distance in the Au lattice (0.288 nm).

The arrangement of the DMSO molecules in the high coverage phase (monolayer) has been also characterized from the theoretical point of view, by means of DFT calculations, performed in collaboration with Dr. S. Velari and Prof. A. De Vita of the University of Trieste, to confirm the hypothesized structure (see the published article of this work [76] for details about the DFT simulations). In figure 3.3d a ball model of the optimized adsorption geometry is shown, while figure 3.3c shows the DFT-based simulation of the STM image, which is in good agreement with the experimental high-resolution image in panel 3.3b of the same figure. Judging from its structure, the stabilizing interaction within this phase is clearly the intermolecular attractive $CH_3\cdots O$ interaction.

3.4 The *square* complex

After annealing the monolayer phase to 233 K, thereby desorbing a large part of the DMSO molecules, the surface appears as shown in the STM image in figure 3.4a. From the high-resolution insets (fig. 3.4b, c), we deduce that the DMSO molecules must be in the same "inverted umbrella" geometry, *i.e.* with the S atom directly interacting with the Au surface, as found in the monolayer phase. From these considerations, the dominant structural motif of this layer appears to be a complex of four DMSO molecules (hereafter referred to as *square*), together with a smaller number of isolated, single DMSO molecules.

Within the square complex, it appears that DMSO favors a geometry where the oxygen atoms are located close to each other, a configuration that should intuitively be relatively unstable, due to mutual repulsion of the oxygen atoms, even though a weak attractive interaction between the methyl groups and the oxygen atoms of adjacent molecules could instead favor the stability of the complex. To investigate the stability of the squares, we performed extensive manipulation experiments, both by scanning at high bias voltages (*i.e.* within 3 V) and by applying voltage pulses on top of the complexes (not showed here).

What we found is that the square can be easily rotated as a whole on the surface plane, but it is impossible to separate its constituent molecules without irreversible damage, *i.e.* the fragments observed on the surface after strong manipulation attempts have completely lost the characteristic appearance, in terms of size and shape, of the DMSO molecules. Therefore, the interaction between the DMSO molecules within the squares appears to be remarkably strong and dominated by the attractive CH_3–O interaction. The issue of the stabilizing interactions within the

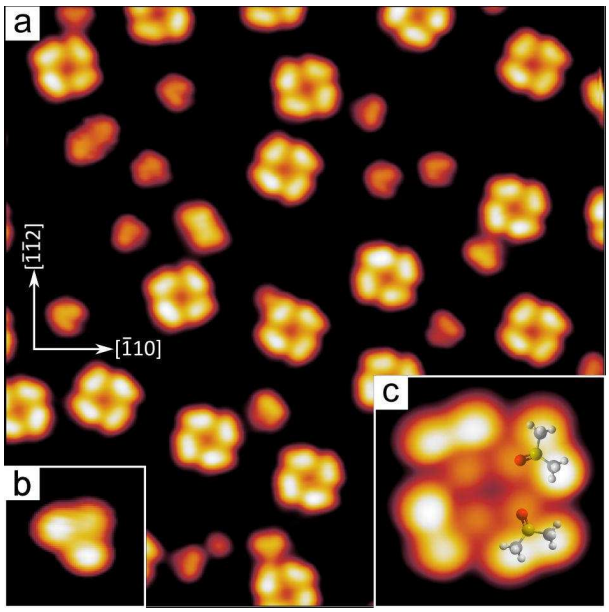

Figure 3.4: (a) STM image (12.82 × 12.82 nm²) showing the square complexes formed by annealing the DMSO/Au(111) multilayer phase to 233 K. Panels (b) (1.00 × 1.00 nm²) and (c) (1.60 × 1.60 nm²) are high-resolution details of a single isolated DMSO molecule and a square complex, respectively. Transparent ball and stick models are superimposed to guide the eye in the identification of the single molecules. Image parameters: (a) V_s = 100 mV, I_t = 100 pA ; (b) V_s = 50 mV, I_t = 100 pA; (c) V_s = 100 mV, I_t = 50 pA.

squares will be tackled later, after discussing the behavior of the system at higher temperatures.

3.5 The *triangle* and *rectangle* complexes

Subsequent annealing of the surface up to 273 K leads to a further decrease in the molecular coverage and to the formation of a variety of new complexes, which are summarized in figure 3.5. In the same figure, high resolution details of the four most common complexes are shown, whereas other minor variants to these configurations can be found on the surface (less than 10% of the total number of complexes). While the arrangement of the DMSO molecules within the complexes in figure 3.5a and d can be readily identified, since the shape of the single DMSO molecules is evident, the complexes in figure 3.5b and 5c are less trivial to understand. More precisely, in the STM image in figure 3.5b, three DMSO molecules can be readily identified, whereas the nature of the brighter protrusion is not straightforward. Similarly, in figure 3.5c, two DMSO molecules can be recognized, whereas the assignment of the two brighter features needs further investigation. For sake of simplicity, from now on we shall refer to the complexes in figure 3.5a to d as the *symmetric rectangle*, *asymmetric rectangle*, *chiral rectangle*, and *triangle*, respectively.

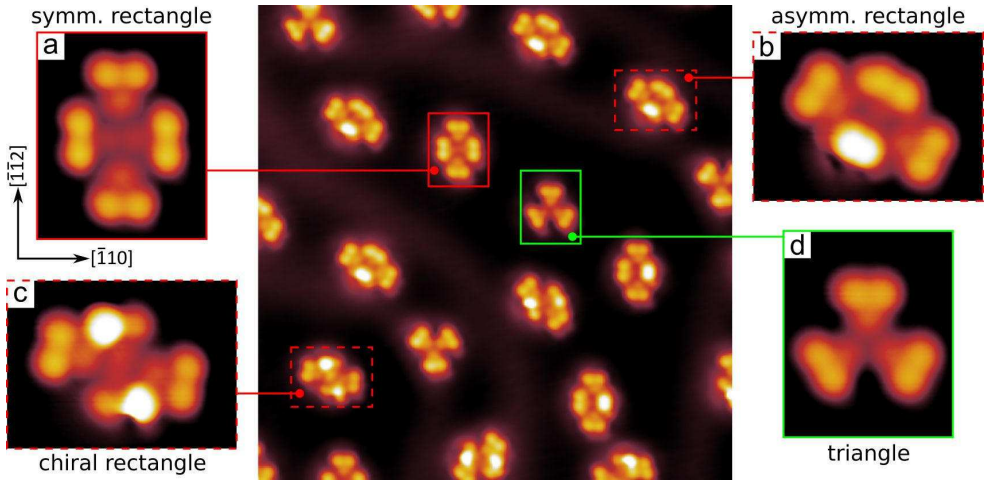

Figure 3.5: STM image (center - 12.94 × 12.94 nm²) showing the various complexes that form on the surface after annealing to 273 K. (a-d) Insets show high resolution details of complexes: (a) the *symmetric rectangle* complex (1.63 × 1.99 nm²), (b) the *asymmetric rectangle* complex (2.21 × 1.62 nm²), (c) the *chiral rectangle* complex (2.21 × 1.62 nm²) and (d) the *triangle* complex (1.63 × 1.99 nm²). All images: 30 mV < V_s < 50 mV, 100 pA < I_t < 200 pA.

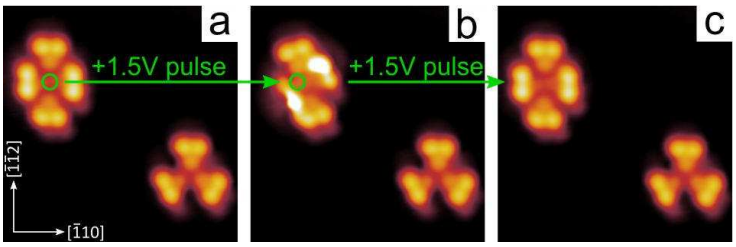

Figure 3.6: Sequence of STM images of the same area, showing the effect of +1.5 V voltage pulses applied with the STM tip at the location indicated by the green marker. A *symmetric rectangle* (a) is converted to a *chiral rectangle* (b) and eventually back to a *symmetric rectangle.* The triangle at the bottom right corner remains immobile in all three images, and acts as a reference. All images: V_s = 100 mV, I_t = 100 pA, 4.20 × 4.20 nm².

To better understand the nature of the observed bright protrusions, we have performed experiments involving the manipulation of the complexes by applying voltage pulses on these complexes. In particular, figure 3.6 shows the result of two subsequent voltage pulses applied at the location indicated by the green markers, in a sequence of STM images acquired from the same area. As can be observed, under voltage pulses, the *symmetric rectangle* can be converted back and forth into the *chiral rectangle*, unambiguously confirming that the constitutive units of both rectangles are the same, *i.e.*, four DMSO molecules.

Similarly, together with various other examples of manipulation experiments, also the *asymmetric rectangle* could be converted to a *symmetric rectangle* and to a *chiral rectangle*, thereby indicating that the protrusion on the side of the former complex is likely a single DMSO in a different adsorption configuration.

3.6 The *triangle* and *rectangle* complexes: trapping of charged gold adatoms

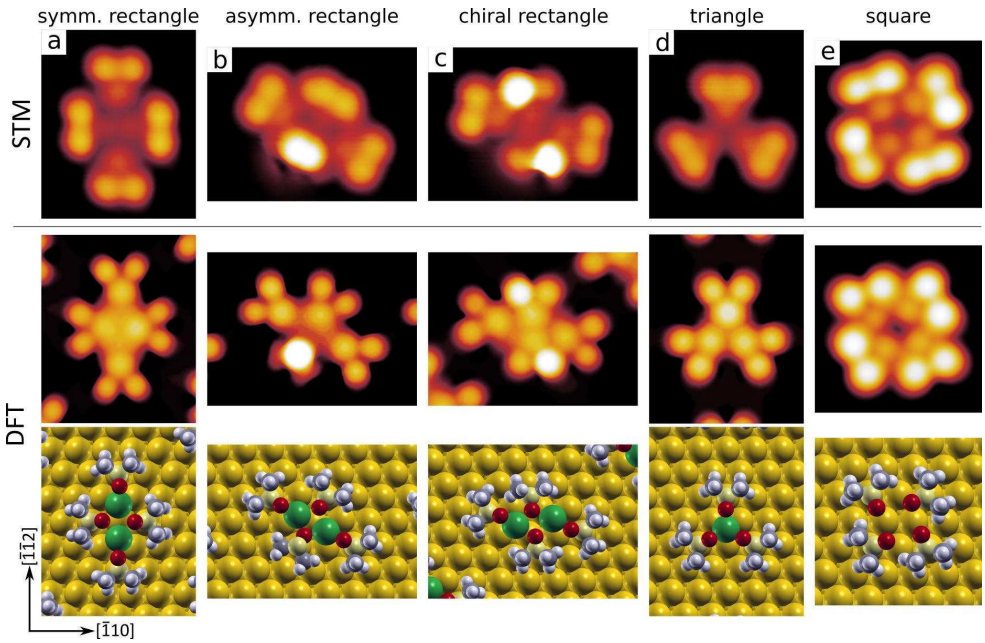

Figure 3.7: (a-e) STM images of the various DMSO complexes from figures 3.5a-d and 3.4c, showing the experimental (top row) and the DFT calculated images (middle row). The bottom row shows ball models of the geometries obtained by DFT calculations, where the gold adatoms are painted in green to ease their identification. The lateral scales of the images within each column are the same, and are the same of figure 3.5a-d and figure 3.4c.

Surprisingly enough, it appears that a common feature of all the described complexes is that the oxygen atoms appear to be preferentially located close to each other, a configuration that should be extremely unfavorable due to the negative

charge on the oxygens. To understand this behavior, we have carried out DFT calculations of the structural, electronic, and energetic properties of the observed DMSO complexes as well as simulations of the STM images.

We started from the simplest complex, *i.e.* the *triangle*. From the experimental STM images, it can be easily inferred that the complex is formed by three DMSO molecules with a measured distance of approximately twice the Au lattice constant between the S atoms. DFT calculations indicate that the most favorable adsorption configuration for a single adsorbed DMSO is the on-top site, with the S atom bound to the metal surface. As expected from the above chemical considerations, a triangle with all three DSMO adsorbed on top is predicted by DFT to be less stable (losing 0.13 eV/molecule) with respect to a single adsorbed DMSO taken as the reference configuration (1.78 eV/molecule). For the details of how the relevant energies are calculated, we refer the reader to the discussion of table 3.1 below. In this *triangle*, upon relaxation each DMSO rotates around the S atom by slightly more than 30°, in order to maximize the O–H interaction, in analogy to the behavior reported for the pure crystalline form [91], thus becoming very different from the complex observed experimentally.

To explain the stability of the structure, we have therefore hypothesized the presence of an Au adatom trapped within the complex, where it could act as an acceptor for the electrons of the oxygen atoms. As a consequence of this ansatz, the *triangle* becomes stable, gaining 0.25 eV/molecule with respect to single DMSO adsorption. In agreement with the experimental STM data, the simulated images clearly show no protrusion related to the adatom at the center of the complex, as can be seen in figure 3.7d. It should be noted that in the experimental STM images the *triangles* can be found pointing in both the $[11\bar{2}]$ and the $[\bar{1}\bar{1}2]$ directions (see fig. 3.5). These two possible adsorption configurations of the *triangle* are consistent with the preferred adsorption site of DMSO (on-top), and with the two possible hollow Au sites for the adatom (*hcp* and *fcc*).

On the basis of the same chemical considerations used for the *triangle*, the stability of the *symmetric rectangle* can only be explained by introducing two Au adatoms, as shown in figure 3.7a, gaining 0.40 eV/molecule with respect to a single adsorbed DMSO. Also in this case, the adatoms are not visible in the experimental STM images, and the absence of protrusions related to their presence is confirmed by the calculated image. The two adatoms are located in *fcc* and *hcp* hollow sites, and consistently with the C_3 symmetry of the substrate, they are observed with the long side oriented in all the three equivalent $[\bar{1}\bar{1}2]$ directions.

With concern to the *asymmetric rectangle* and the *chiral rectangle*, various models have been tested, and the ones that show the best agreement with the experiment in terms of energetics and appearance of the STM images are shown in figur 3.7b and c. The energetic gain, referred to a single adsorbed DMSO, is 0.35 eV/molecule and 0.32 eV/molecule, respectively.

In the *asymmetric rectangle* (fig. 3.7b), the brighter protrusion is originated by a DMSO molecule in an "inverted" adsorption geometry, *i.e.*, with the S atom pointing out of the surface plane and the O atom interacting with the Au adatoms. As in the

case of the *symmetric rectangle*, the two adatoms are located in *fcc* and *hcp* hollow sites, and the complexes can be found on the surface with the same orientations.

The *chiral rectangle* (fig. 3.7c) is again characterized by the presence of two adatoms in *fcc* and *hcp* hollow sites. However, in this case, the two sites are almost aligned along the $[1\bar{1}0]$ direction, with the adatoms located slightly off-site, giving rise to a characteristic angle of $\pm 14^\circ$ of the long side of the complex with respect to the equivalent $[1\bar{1}0]$ directions.

The simulated STM images in figure 3.7a-d are in good agreement with the corresponding experimental images, since the morphology of the main features can be immediately identified, in particular concerning the lack of features related to the presence of the adatoms. However, it is also clear that the methyl groups in the simulated images always appear lower than the experimental ones. This artifact can be traced back to the pseudopotential used in our calculations, which underestimates the S–Au distance, inducing the methyl groups to relax to a slightly lower position, thus yielding a decrease in their contrast which is not observed in the experimental images.

It is to be noted that we have no direct information to pinpoint the process by which the DMSO complexes form, in particular concerning the actual origin of the adatom(s) in the complexes. However, in the temperature range where we observe adatoms trapped within complexes (*i.e.* above 233 K), it is well known that native gold adatoms can detach from step edges, diffuse along them and across the surface itself, as well as be extracted from the herringbone reconstruction and elbow sites [68, 92, 93]. Moreover, it is also well established that molecular adsorption, especially involving very electronegative species, can significantly promote such processes [68, 94]. In contrast to thiols and other molecules that interact strongly with gold, in our case no lifting of the herringbone reconstruction was ever observed, likely because the interaction of DMSO with gold is comparatively weaker (no covalent bonding occurs between the molecule and the metal).

3.7 The *square* complex: adatom?

The case of the square complex deserves a separate discussion. Similarly to the other complexes, the oxygen atoms are quite close to each other, possibly giving rise to a repulsive interaction that could in principle destabilize the complex. However, in this case the molecular arrangement also favors the interaction between the oxygen and the methyl groups of each couple of adjacent molecules. The calculated CH–O angle in the closest H–O couple (2.5 Å) is approximately 140°, and this geometry does in fact favor the formation of a hydrogen bond [95–97]. Additionally, as mentioned above, the square exhibits a remarkable stability upon manipulation with the STM tip. Therefore, the question arises whether or not an adatom is trapped inside the complex, and the contrast of the STM images cannot address this point since we have verified that the trapped adatoms, even when present, are not visible both in the experimental and simulated STM images. To clarify this point, on one side we

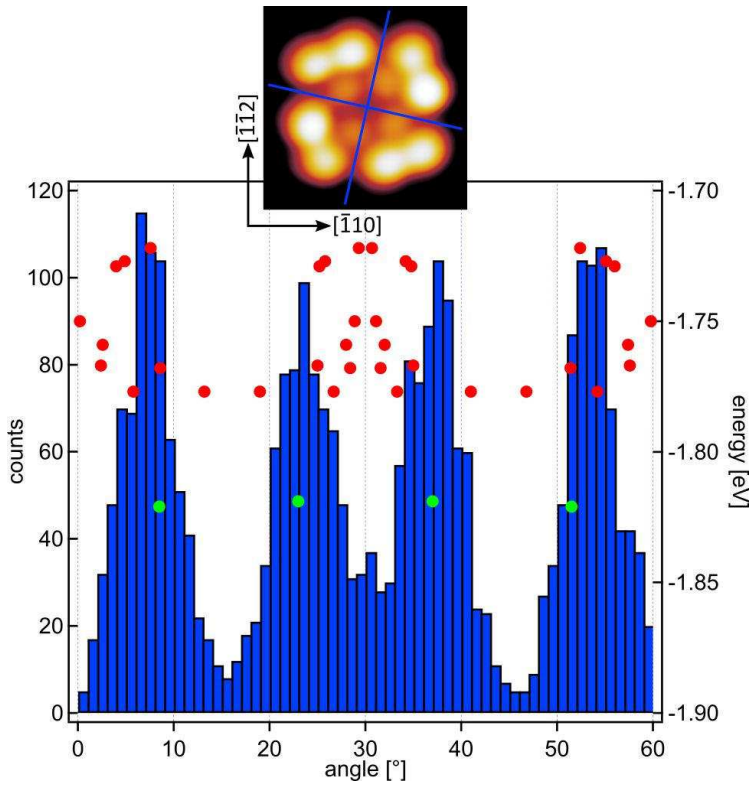

Figure 3.8: Experimental angular distribution of the *square* complexes (blue histogram, left axis) and the adsorption energy per molecule (markers, right axis) of the possible candidate models for the *square* complex with (red) and without (green) the central adatom. The thumbnail above the graph shows the directions taken as a reference to determine the orientation of the *square* complexes.

analyzed the distribution of the characteristic orientations of the complexes with respect to the Au(111) crystallographic directions in the experimental STM images, and on the other we carefully evaluated the energetics of the different complexes as obtained by DFT.

As a starting point, we have measured the orientation of more than 1500 square complexes on the experimental STM images, using as a reference the directions shown as blue lines in the top inset of figure 3.8. By taking into account both the symmetry of the substrate and the symmetry of the *square* complexes themselves, the resulting angular distribution of the complexes falls within 0° and 60° (see the published article of this work [76] for details on the measurement of the angles), and is represented by the blue histogram in figure 3.8 (left axis). It is clear that squares are aligned around four distinct angles, namely 7°, 23°, 36° and 53° with an error of about ±4°. In the same graph, the green and red markers show the calculated energies of various structures composed by four DMSO molecules (right axis), hypothesized as reasonable candidates for the *square* complex, as a function

Table 3.1: Calculated average adsorption (E_{ads}) and cohesion energies (E_{coh}) per DMSO molecule of the various molecular complexes (energies in eV).

Species	E_{ads}	E_{coh}
single DMSO	1.78	-
square	1.82	0.05
triangle	2.02	0.25
symm. rectangle	2.17	0.40
chiral rectangle	2.09	0.32
asymm. rectangle	2.11	0.35

of their characteristic angle with respect to the surface. In particular, the red (green) markers correspond to the models including (excluding) the Au adatom. It is to be noted that relaxation of the models corresponding to the red markers after removal of the adatom consistently yielded one of the structures corresponding to the green marker.

Both analyses indicate that, at variance with the other observed complexes, the *squares* do not include a central gold adatom: First, from the energetic point of view, it is clear that the complexes with no adatom are always more stable (green markers) by more than 50 meV. Second, a clearly different angular distribution should be found if the *squares* included the adatoms (red markers).

3.8 Adsorption energies

Table 3.1 shows the calculated average adsorption E_{ads} and cohesion E_{coh} energies per DMSO molecule of the various molecular complexes. The adsorption energies have been calculated as:

$$E_{ads}(n) = -\frac{1}{n}\left[E(nDMSO/sub) - n \times E(DMSO) - E(sub)\right]$$

where *sub* indicates the substrate, *i.e.*, the clean Au(111) surface, for the single DMSO and the *square*, or the surface with one or two Au adatoms, for the *triangle* and the *rectangles*; *n*DMSO indicates a DMSO complex with n molecules; $E(nDMSO/sub)$, $E(DMSO)$ and $E(sub)$ indicate the energies of the total system (adsorbed complex and substrate), of a gas-phase isolated DMSO molecule, and of the substrate, respectively. The cohesion energy per molecule, defined as

$$E_{coh}(n) = E_{ads}(n) - E_{ads}(1)$$

indicates the energy gain per DMSO molecule in the most stable adsorption configurations of a complex with respect to the adsorption of the individual molecule(s) on the bare Au(111) surface.

The energetics of the various complexes can help to rationalize the experimental observations. The least stable species is the single DMSO molecule (1.78

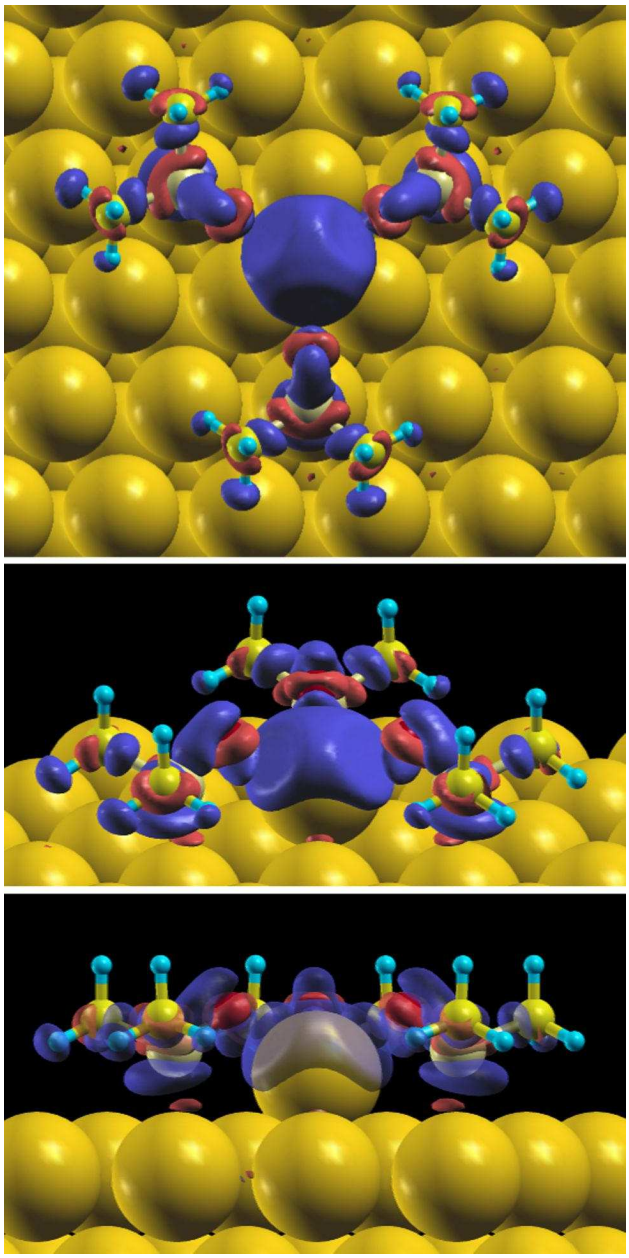

Figure 3.9: Top (top panel) and side (bottom panel) views of the changes in charge density around a gold adatom coordinated by three DMSO molecules (*triangle* complex) on the Au(111) surface with a pre-existing adatom on it. A perspective view (middle panel) is also shown. The accumulation of negative charge is depicted in red, the depletion in blue. The blue lobe surrounding the adatom highlights its cationic behavior.

eV/molecule), that was in fact observed in rare cases. The *square* complex (1.82 eV/molecule) is more stable than the single adsorbed molecule, and is by far the dominant structure, together with the monolayer phase, at temperatures below 233 K. This is apparently in contrast with the fact that all the other complexes are significantly more stable than the *square* itself, and should therefore dominate the surface. However, as shown above, strong energetic and structural evidence indicate that this particular complex is the only one not entrapping one or more Au adatoms. It is reasonable to assume that at temperatures below 233 K a decreased availability of gold adatoms prevents the formation of *triangles* and *rectangles*, and therefore favors the formation of the *squares*. This consideration further strengthens the conclusion that no adatoms are trapped inside the *squares*.

The cohesion energies reported in table 3.1 indicate that the presence of the adatoms in *triangles* and *rectangles* plays a relevant role in the stability of the complexes: molecule-molecule and molecule-adatom interactions (E_{coh}) account for $15\% - 18\%$ of their adsorption energies E_{ads}. Conversely, in the squares, E_{coh}/E_{ads} is only 3%, consistently with the weaker molecule-molecule hydrogen bonding.

DFT calculations also reveal that a peculiar redistribution of the electron density occurs around the Au adatom, as shown for the *triangle* by the charge density transfer plots in figure 3.9. The latter have been calculated as $\rho_{tot}(\mathbf{r}) - \rho_{sub}(\mathbf{r}) - \sum \rho_{mol}(\mathbf{r})$, where $\rho_{tot}(\mathbf{r})$ is the charge density of the total system, $\rho_{sub}(\mathbf{r})$ the density of the gold substrate including an isolated adatom, and $\sum \rho_{mol}(\mathbf{r})$ the density of three non-interacting DMSO molecules in gas phase.

Namely, the density depletion (blue lobe) occurring at the gold adatom suggests that this atom displays a significant degree of cationic behavior. This is confirmed by the calculation of the atomic Löwdin charges [98]: even in the absence of DMSO coadsorption, a single Au adatom in the hollow position is always slightly positively charged ($\approx -0.21e^-$) with respect to an atom of the surface layer, by donating electronic charge to the nearest neighbor surface Au atoms. In the presence of a DMSO complex, the adatom recovers only part of its electronic charge ($\approx -0.08e^-$ relative to the single adatom) and rearranges the occupation of its s, p, and d orbitals. Moreover, at the same time, an increase in the electronic charge occurs on its second nearest neighbor surface Au atoms, which are directly interacting with the sulfur of DMSO. The oxygen atoms surrounding the adatom are polarized in a characteristic double peak-trough pattern: this charge rearrangement pattern favors the coordination of the oxygen terminations of DMSO with the gold adatom, which effectively acts as ionic linker between the otherwise mutually repelling molecular terminations. The observed charge depletion and the proximity of deep p-orbitals associated with the oxygen atom ligands imply the lack of electron states available for tunneling in the STM observations at the Au site. This is consistent with the STM images where the adatom is indeed not visible.

It is to be noted that linker adatoms which cannot be resolved in STM images were also reported in other works, and this effect was accompanied by a reduction of the occupation of the adatom states upon surface complexation [63, 72]. It is important to remark that we have carried out extensive imaging on the complexes

at various sample bias voltages, ranging from −3 up to +1 V. Within this interval, no significant contrast variations could be observed on the complexes, except for degradation of the resolution and broadening of the molecule-related protrusions. This observation gives experimental confirmation that no adatom-related electronic states are available for tunneling in the examined energy range. Measuring at bias voltages outside this range yielded very unstable imaging and easily induced changes in the complexes, even at very low tunneling current set points ($\approx$ 1 pA), pointing out to possible, strong interactions between the tip-sample electric field and the molecular dipole. Eventually, it is to be noted that also the simulated images show no relevant contrast variation within the above-mentioned bias range, and the adatom-projected density of states is negligible in the corresponding energy interval.

Our finding of a significant charge redistribution around the presumably entrapped adatoms is analogous to what was observed by Pawin *et al.* for 9,10-anthracenedicarbonitrile on Cu(111), where a similar effect occurs [99]. Such charging effect could explain the reported increase in the reactivity of Au(111) surfaces covered by PDI metal-organic frameworks with respect to CO_2 and CO adsorption, compared to the bare Au(111) surface [100, 101]. Notably, evidence has been found that charging is at the origin of the reactivity of small gold nanoclusters on metal oxide surfaces, for instance in reactions involving CO [102–105].

Finally, we observe that the ionic character of the DMSO-adatom interaction is consistent with the average Au(adatom)–O distance, which is approximately 2.6 Å, and 30% larger than the same distance in related oxo-gold compounds ($\sim$ 2.0 Å), where the Au–O bond is mainly covalent [106].

3.9 XPS and NEXAFS experiments

XPS. To get chemical fingerprints about the adsorption of DMSO on Au(111), we performed XPS experiments. We have first monitored the O 1s and S 2p photoemission spectral features of films obtained by depositing the molecules at different temperatures T_s of the Au(111) sample in the 153 K $< T_s <$ 300 K range. Curve fitting reveals the presence of multilayer components for $T_s <$ 193 K (top spectra in figure 3.10), whereas a decreasing coverage starting from the full monolayer is observed in the 193 K $< T_s <$ 300 K range. It is to be noted that, in the latter temperature range, both S 2p and O 1s spectra are always characterized by a single component (bottom spectra of figure 3.10), and no significant changes in the profile shapes are observed with decreasing coverage. In the S 2p spectra, minor features are visible below 165 eV, related to X-ray induced damage. In figure 3.10, the deconvolution profiles obtained by the fitting procedure highlight a binding energy shift between the monolayer (blue) and multilayer (black) components, arising from the screening effect of the metallic substrate.

The shift has comparable values, within 0.1 eV, for both the S 2p and O 1s features. Both the S and O atoms of the DMSO molecule have an electron lone pair

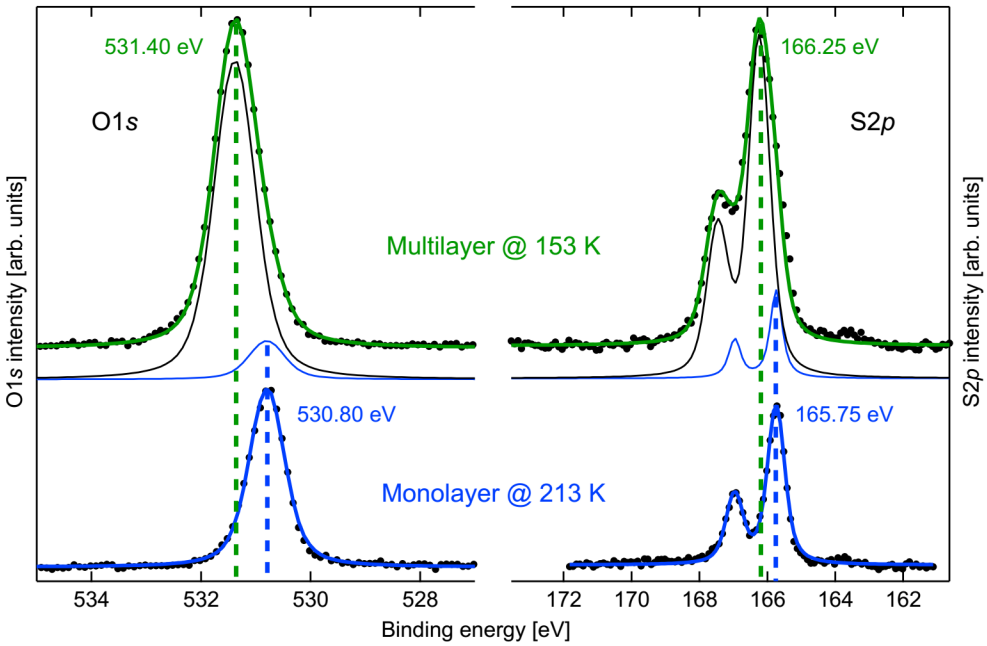

Figure 3.10: O 1s and S 2p spectra ($h\nu$ = 650 eV) acquired on the multilayer (153 K - top spectra - green) and on the monolayer (213 K - bottom spectra - blue) phase. The uncertainty on the absolute binding energy values is ±0.05 eV. Individual components, obtained from the fit, are superimposed on the spectra.

and can therefore act as electron-donors in binding to the substrate or to an adjacent molecule. In the latter case, as compared to a noninteracting molecule, an increase in the binding energy of the donating atom is expected. On these bases, in an early paper, Su and Faller [107] measured the difference between the O 1s and S 2p binding energies, ΔE_b, for several metal-DMSO complexes, attempting to determine from this quantity whether the metal-molecule bonding occurred through the oxygen atom, the sulfur atom or both. This method was adopted to rationalize the XPS data for the adsorption of DMSO on Au(100) and Pt(111) [86, 89], where bi- and mono-dentate configurations have been found, respectively. By adopting this approach, the change in ΔE_b we found ($\approx$ 0.1 eV – not significant within our errors) suggests that, as it occurs on the Au(100) surface, also in the Au(111) case DMSO adsorbs interacting with both its donor terminations to the metal. However, an important aspect, which was not discussed in the cited works, has also to be considered. Indeed, the supramolecular assembly at both monolayer and multilayer stages can be driven by the formation of intermolecular hydrogen bonds, which affects the binding energy of the termination involved in the interaction. If we assume that the structure of the DMSO multilayer resembles the crystalline phase, where oxygen-methyl interactions are present [91], a shift toward higher binding energies is expected in addition to the screening effect of the substrate. The proper reference value of ΔE_b for a noninteracting DMSO molecule should therefore be

provided from spectra acquired in the gas phase, which are not available. Indeed, as suggested by our STM data and DFT calculations, the O–CH_3 affinity drives the assembly of the monolayer phase. These observations indicate that it is not possible to unambiguously infer a bi-dentate DMSO-metal bonding from the observed small ΔE_b, and therefore call for further investigations to characterize the nature of the molecule-metal and molecule-molecule interactions.

Summarizing, according to the interpretation of the XPS spectra by the Su and Faller method, from a negligible shift in ΔE_b (as we observe) a bidentate binding mode (S-metal and O-metal) would be expected at all the temperatures we have characterized. In contrast to this conclusion, our STM and DFT results indicate that at temperatures below 233 K there is no oxygen-metal bonding, but only O–CH_3 hydrogen bonds are formed. This observation points out to a limited applicability of the Su and Faller method, primarily because it does not consider the possibility of types of S- or O- interactions other than with the metal itself. In fact, in our case, it is evident that a similar shift in ΔE_b can be induced by O-metal or O–CH_3 interactions.

NEXAFS. We also investigated the DMSO adsorption geometry at the monolayer stage by means of NEXAFS measurements. Figure 3.11 reports the O 1s light polarization-dependent NEXAFS spectra, measured on a DMSO monolayer grown at 213 K. The fit of the curves reveals the presence of distinct components, showing a clear dichroic effect, thus suggesting that the molecules adsorb on the surface with preferential orientation. It is to be noted that similar conclusions can be drawn from NEXAFS spectra acquired at higher temperatures (which are not showed here).

Our spectra resemble the ones taken in both the gas [108] and liquid phase [109], apart from a finer structure observable in our case, possibly due to the fact that in both non-solid phases the molecules are randomly oriented and dichroic effects are not measurable.

In a nutshell, comparison with gas phase spectra [109, 110] identifies peak 3 (532.7 eV) as due to a transition from the O 1s to the LUMO, which has a π^* character, and is expected to have maximum intensity when the photon polarization is perpendicular to the S=O bond. Conversely, peak 4 (533.5 eV) shows opposite polar dependence and can be assigned to the σ^* transition of the same bond. By comparing the intensities of this peak at the two polarization angles, we determined that the S=O bond is tilted by $25^\circ \pm 10^\circ$ with respect to the surface plane [111]. This value is fully compatible with all the DFT calculated structures, where it lies between 25° and 32°. This result can be rationalized in the context of simple chemical considerations. The sulfur atom of DMSO has a tetrahedral coordination geometry, exposing an electron lone pair at the "tip" of the umbrella structure that characterizes the molecule. The angle between this pair and the S=O bond is roughly 110° for the free molecule. Considering that the binding to the metal substrate typically occurs through the lone pair (as in the case of ammonia [112], for instance), the expected value of the angle between the S=O bond and the surface plane for the adsorbed molecule is about 20°, in agreement with our results.

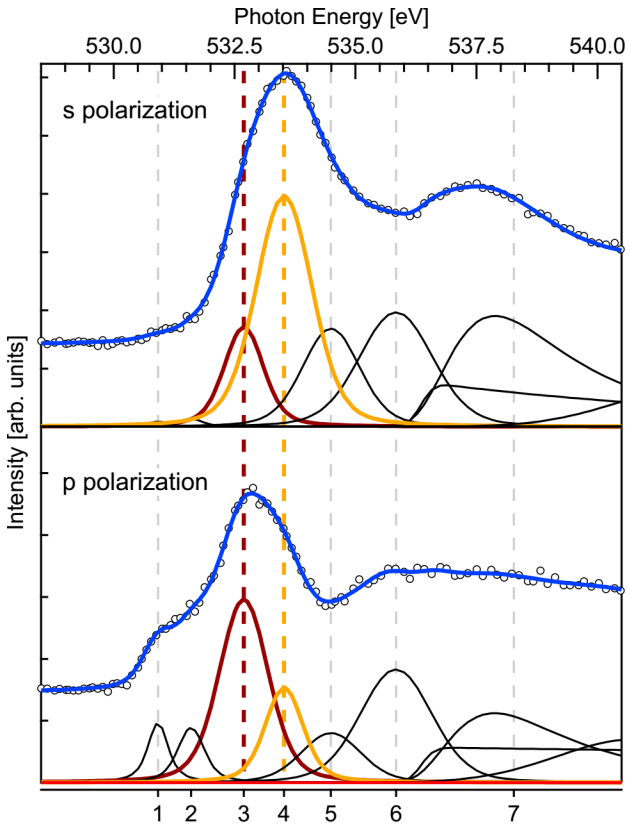

Figure 3.11: Linear dichroism NEXAFS spectra at the O 1s edge for two different synchrotron light polarizations (s polarization: **E** parallel to the surface; p polarization: **E** perpendicular to the surface) of DMSO/Au(111) after annealing at 213 K. The main peaks, 3 and 4, are located at 532.7 eV and 533.5 eV respectively. Peaks 1 and 2 are assigned to impurities or beam induced damage, whereas peaks 5, 6 and 7 are related to oxygen Rydberg states [108].

3.10 Conclusions

In the present work, we have shown that there is a mutual stabilization between a common, polar molecule, DMSO, and native, positively charged adatoms on the Au(111) surface. The existence of these adatoms, for which no directly related features are visible in the experimental data, is strongly supported by the agreement between the measured and simulated STM images, as well as by the observed stability of the complexes, that would remain otherwise unexplained. Further possible experiments which may support our results consist in exploring the concentration of the adatoms, which can be controlled in principle by depositing metal atoms or by exploring the behavior of the DMSO molecules on a different metal surface with a higher adatom population, such as copper.

These adatoms act as ionic linkers between the molecules, a behavior reported up to now only for alkali metal linkers. The broader interest of any such mechanism

stems from the evidence that, even at low coverage, fabricating discrete structures with high size selectivity can be achieved by exploiting more than just attractive short-range intermolecular interactions (*i.e.*, van der Waals, or H^- bonding). In particular, it is gradually becoming clear that monodisperse cluster populations can be obtained if interactions of electrostatic nature are also present, as, for instance, repulsive interactions between parallel dipoles which act on a longer range [113].

The observed mutual stabilization of DMSO and Au is likely related to the strong dipole moment of the molecule and the strong electronegativity of its constituents: further investigations are envisioned on the specific role of the sulfinyl group which could be exploited as a functional group to drive the assembly of more complex tectons through the described electrostatic linkage scheme, based on nondestructive extraction/stabilization of native metal atoms from the substrate.

The nanoscale properties of the Au-DMSO interface are also of great relevance in electrochemistry and, more generally, wet chemistry. For instance, a relatively strong DMSO-Au binding, as originated from our observed bidentate configuration, was hypothesized as a possible origin of the unusual behavior of liquid DMSO at noble metal electrodes [89, 90, 114]. Very recently, the ability of DMSO to act as a "functional solvent" in the synthesis of metal nanoparticles, advantageously providing in a single solvent the ability to both solvate and stabilize the gold aggregates, was tentatively explained by Duggan *et al.* with an enhanced S^- and O^- coordination to gold, on the basis of FT-IR spectra [115]. Clearly, a generalization of our results to the mentioned cases, where liquid-solid interfaces are involved, is far from straightforward, but further investigations at the liquid DMSO-Au interface could benefit from our findings.

Chapter 4

Chemistry of the methylamine termination at a gold surface

The study of the interface between primary amines and metallic surfaces is an important topic in physical chemistry. Amines are involved in several industrial processes, ranging from the denitrogenation of fuels in the oil industry [116, 117], synthesis of polymers [118, 119] and other compounds [116, 120] to the control of food preservation [121]. Therefore, notable efforts have been devoted to the study of the reaction and decomposition of small amines on catalytic metals like Pt [122–124], Ni [125–128], Ru [129, 130], and Pd [131], in order to understand and optimize the aforementioned processes. More recently, the interaction between primary amines and the less reactive Au(111) surface has become a relevant issue as well. This is related to the chemistry of the amino-gold interaction, which is governed by the nitrogen electron lone pair [132–134]. The resulting junction is characterized by a well-defined geometry and electronic structure, thus representing a reliable electrode-molecule contact in single molecule conductance experiments [132]. Interestingly, despite the non-covalent nature of the interaction, ultrafast charge delocalization has been shown to occur at the amino-gold interface [135], which therefore represents a promising prototype for the design of organic-based devices. The self-assembly process of small amino-terminated molecules on the Au(111) surface is the result of the interplay between the molecule-molecule and the amino-gold interactions [134]. The amino-gold bond is weak enough to ensure a high molecular mobility on the Au(111) surface and to promote the formation of intermolecular bonds.

We report here a detailed study on Au(111) of the chemical and morphological properties of ultrathin films of 1-naphthylmethylamine (NMA, fig. 4.1), constituted by a naphthalene unit with a methylamine substituent, combining STM imaging and X-ray Spectroscopies (XPS and NEXAFS) with DFT calculations. The molecule represents a good prototype for studying the properties of the methylamine functionalization of polyacenes and its role in the self-assembly process of these molecules on surfaces. The study describes the chemistry of the molecule on the gold surface as

a function of the sample temperature (T_s). In fact, three distinct phases are obtained at different T_s ranges, characterized by single molecular layers of different density, morphology and chemistry, namely the Flat Phase, the Standing-up Phase and the Condensed Phase. The Flat-Phase provides the aforementioned surface functionalization and is characterized by the molecules being adsorbed with their naphthalene block parallel to the surface. The morphology stems by the interplay between the amino-gold and amino-amino interactions, the latter involving an auto-recognition process based on an amino-amino hydrogen bonding scheme [43]. In particular, we describe by means of DFT the different adsorption geometries that small clusters of molecules can exhibit on the surface, as suggested by STM images. We show that the amino-terminations play a crucial role in the assembly process of the clusters and we relate their different chemical configurations to the measured N 1s NEXAFS features. The obtained results serve then as a reference for a more qualitative description of the other two reported phases. The first is the Standing-up phase, where the molecules are found lying tilted-up with respect to the surface, their assembly being possibly stabilized by the interaction between the amino group and a phenyl ring of adjacent molecules. The second one is the Condensed Phase, characterized instead by a complete deamination of the molecules and their simultaneous condensation in dimers.

This work, where I contributed with most of the STM experiments, has been published in *Chemical Communications* [43] and *The Journal of Physical Chemistry C* [136].

4.1 The NMA molecule

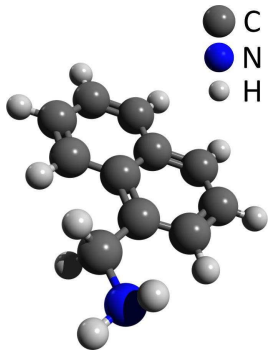

Figure 4.1: 1-naphthylmethylamine (NMA) molecule.

NMA is a naphthalene molecule with a methyl-amino functional group substituting one of the hydrogen atoms in α position, as depicted in figure 4.1. We chose to employ a methylamino-functionalized molecule, not simply amino-functionalized, in order to give enough geometrical freedom to the $-NH_2$ terminations to interact with each other and with the substrate. NMA (Sigma Aldrich, 97%) was evaporated from a Pyrex vial, connected to the experimental chamber through an all-

metal valve. Exposure of the Au(111) sample to the molecule at its vapor pressure ($\sim 5 \times 10^{-8}$ mbar) for 5 seconds yielded a saturation coverage for sample temperatures between 220 and 360 K. The NMA multilayer was obtained at lower temperatures, whereas no molecular sticking was observed above 360 K. The Standing-up Phase was obtained at 220 K $< T_s <$ 250 K; the Flat Phase at 280 K $< T_s <$ 360 K; the Condensed Phase was obtained upon annealing of the Flat Phase to $T_s >$ 360 K.

The DFT calculations, as well as the simulated STM images, have been performed by the group of Prof. Giovanna Fronzoni. Details about the theoretical methods can be found in the published paper of this work [136].

4.2 Flat phase

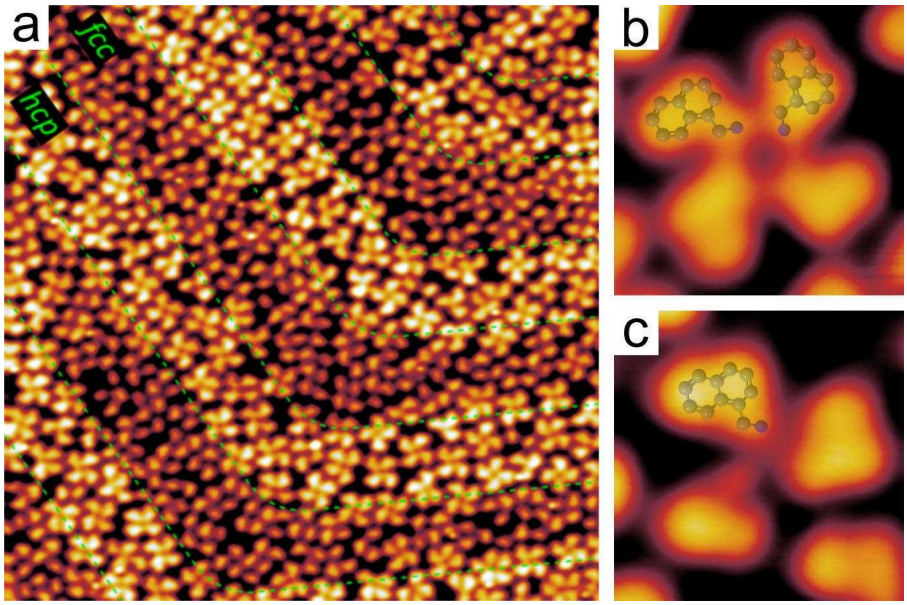

Figure 4.2: (a) Experimental STM image showing the distribution of the NMA complexes in the Flat phase: the *hcp* regions of the herringbone reconstruction of the Au(111) substrate (brighter areas) are covered mostly with (b) 4-leaf clover structures, whereas the *fcc* regions (darker areas) are covered mostly with (c) irregular molecular clusters and single isolated molecules. Image parameters: (a) $V_s = -200$ mV, $I_t = 10$ pA, 30.0×30.0 nm^2. (b) $V_s = +200$ mV, $I_t = 30$ pA, 2.2×2.2 nm^2. (c) $V_s = +100$ mV, $I_t = 50$ pA, 2.0×2.0 nm^2.

STM. We performed several depositions at a sample temperature $Ts \sim 280$ K followed by an annealing of the sample at higher temperatures, in the $280 < T_{anneal} <$ 330 K range. Actually, we also observed that the same film morphologies are obtained by directly depositing the molecules on the sample kept at T_{anneal}, without any further treatment. Both XPS and STM reveal that no multilayer is formed at these temperatures and that the saturation coverage is a function of T_{anneal}, the

NMA SAM being more compact at lower temperatures. STM images (see figure 4.2) reveal that the NMA molecules assemble in n-leaf clover-like clusters, with n = 3-5. The distribution of n values depends on the overall molecular coverage, which is determined by the temperature of the sample T_s. At higher coverage (or lower T_s) the molecules pack in higher n structures, whereas the 3- and 4-leaf clusters are predominantly observed upon preparation at room temperature (RT), $T_s \sim 300$ K.

Figure 4.2 reports the images of a NMA monolayer grown at RT. Interestingly, the distribution of the different structures on the surface is not random but follows the underlying herringbone reconstruction of the Au(111) substrate. The reconstructed Au(111) surface is known to expose sites with different reactivity, due to the different coordination of the gold atoms of the outer atomic plane [137]. Figure 4.2a shows alternating regions of *fcc* and *hcp* areas with lower and higher Au coordination that are decorated with different structures of adsorbed molecules. Irregular clover-like structures or even single isolated molecules are mostly present on the *fcc* regions of the surface, which correspond to the most reactive parts of the herringbone reconstruction. On the contrary, more regular 4-leaf structures populate the less reactive stripes - the *hcp* regions. In the close-up shown in figure 4.2b, details of the clover-like supramolecular assembly can be seen. From the shape of the leaves, the orientation of the molecules can be inferred, indicating that the amino groups are oriented towards the center of the clover. In figure 4.2c an irregular molecular cluster is shown, where two molecules look like the ones in the 4-leaf clover structure, while the third NMA looks different from the others.

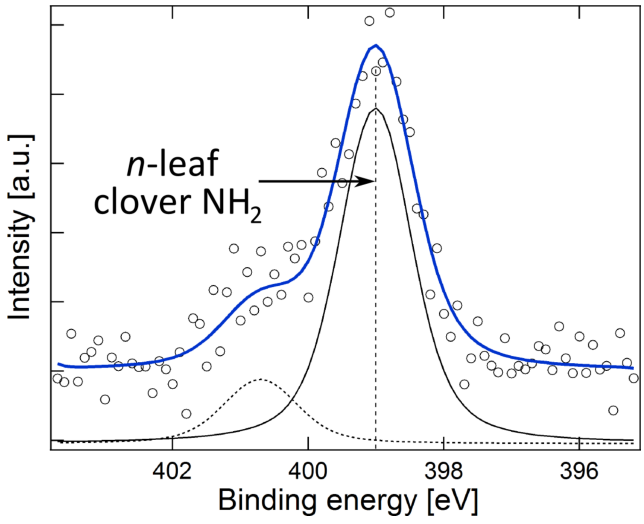

Figure 4.3: N 1s XPS spectrum of the Au_{NMA} surface indicating that the amino groups of most of NMA molecules are in their neutral state.

XPS. The N 1s XPS spectrum in figure 4.3 shows a peak with two components. The position of the main component (399.0 eV) indicates that most of the molecules are in their neutral state (NH_2). The second component at higher binding energy

(400.7 eV) can be related to molecules interacting with the substrate through the amino group. In fact, a shift to higher binding energies of the N 1s peak can be due to the interaction of the primary amines with the gold surface [138] and can be related here for instance to some molecules adsorbed on the more reactive under-coordinated gold atoms at the edges of the terraces.

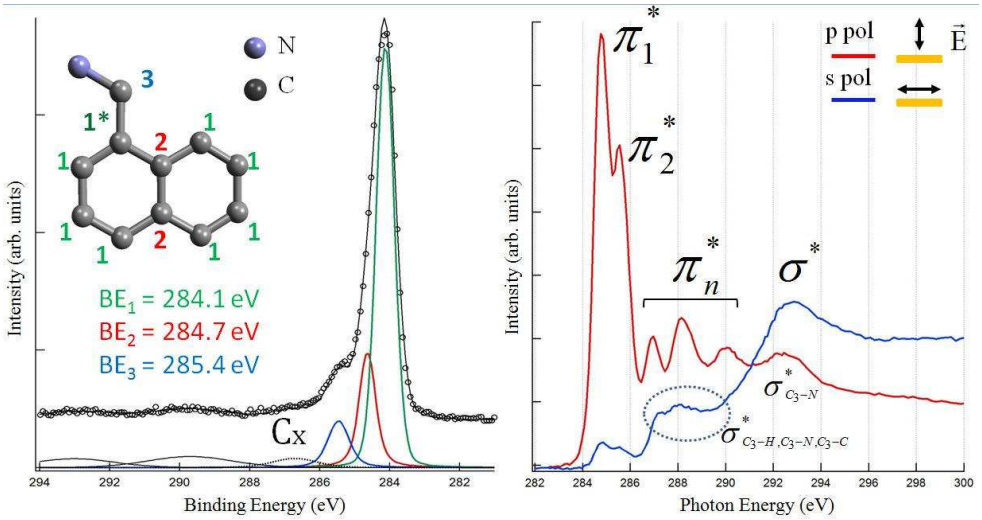

Figure 4.4: Flat Phase. Left panel: C 1s XPS and its deconvolution into the different components, assigned to three inequivalent carbon atoms of the molecule, as indicated in the sketch of the molecule. Right panel: C 1s NEXAFS measured at two different polarization angles, revealing the strong dichroism due to the flat adsorption geometry.

Figure 4.4 shows the C 1s XPS and C K-edge NEXAFS of the flat monolayer phase. The C 1s XPS spectrum is reported in the left panel. Following the fitting assignments adopted for naphthalene [139], the main peak at ~ 284 eV can be properly fitted with two components in a nearly 4 : 1 ratio, corresponding to the chemically inequivalent sets of carbon atoms C1 and C2, as indicated in the sketch of the molecule. To obtain a proper agreement with the experimental curve, a third component is then needed, lying at higher binding energy (285.4 ± 0.2 eV), that we assign to the aliphatic carbon C3. This assignment will be further supported by the study of the Condensed phase we present later. Two other peaks, located at even higher binding energies (~ 289.5 eV and ~ 293 eV), are related to shake-up molecular processes. Finally, the fit reveals a minor component close to 286.7 eV, Cx in the figure, whose nature cannot be unambiguously determined. In fact, it will be shown in the section 4.4 that this component can be likely assigned to a minor fraction of NMA molecules that have undergone de-amination. It has to be pointed out that, due to the presence of the methylamine termination, the symmetry of the naphthalene block, that we assumed to fit the main peak at ~ 284 eV, is lost, as well as the equivalence of the two sets of carbon atoms (C1 and C2). In particular, the atom in α position (indicated as 1^* in the inset of fig. 4.4) could in principle present

different spectroscopic properties because of its bond with the functional group of the molecule. However, the reliable fit we obtained with the previously discussed assumptions indicates that the effects of these differences are not detected by XPS in this case and that the naphthalene assignments are compatible with the NMA naphthyl block.

NEXAFS. On the right panel of figure 4.4, the C 1s NEXAFS spectra acquired at two different polarization angles of the electric field with respect to the surface are shown. P-pol and s-pol geometries refer respectively to the photon electric field normal and parallel to the surface plane. Similarly to the XPS, the NEXAFS spectra closely resemble the ones of the naphthalene molecule [139, 140]. The main two peaks around 285 eV can be assigned to the transitions from the naphthalene carbon atoms to the π_1^* and π_2^* orbitals, respectively. The subsequent three structures visible in the p-pol scan are also related to transitions to π^* orbitals [140]. The strong linear dichroism of the NEXAFS spectra with the π transitions exhibiting a maximum in the p-pol configuration indicates that the molecules adsorb in a flat lying geometry with aromatic ring parallel to the surface, as suggested by the STM images. Notably, while the linear dichroism is almost complete for the first two peaks (I_π(s-pol)/I_π(p-pol) $\rightarrow$ 0, I_π(x-pol) being the intensity of the π orbitals in the x-pol), a residual intensity in the s-pol spectrum is present around 288 eV, even though the corresponding transitions have the same symmetry as the ones occurring at around 285 eV. In the same way, the σ^* feature around 292 eV exhibits a reduced dichroism (I_σ(s-pol)/I_σ(p-pol)), with residual intensity clearly visible also in the p-pol spectrum. In fact, the residual intensity at both 288 eV and 292 eV can be attributed to the contribution of the methyl carbon C3. In the case of gas phase glycine, σ^*_{CH}, σ^*_{CN}, σ^*_{CC} transitions have been observed at 287.7 eV and at 288.4 eV and 289.4 eV, respectively [141]. Moreover, both σ^*_{CN} and σ^*_{CC} resonances have been observed to contribute to the absorption intensity at 292 eV [142, 143]. Here we can therefore accordingly assign these residual features to the amino-methyl termination. Since their contribution is superimposed to the more intense contributions from the naphthalene atoms, we cannot unambiguously evaluate their dichroism. However, they are visible at both polarizations indicating that for at least part of NMA molecules the amino-methyl termination is not perfectly parallel to the surface. This finding is in agreement with our STM images, which show that non-equivalent NMA molecules are present on the surface (fig. 4.2c).

DFT. Interestingly, a certain modulation of the surface reactivity is still present upon the Flat phase formation, as can be evidenced in figure 4.2a. These observations suggest that the interplay between the intermolecular and the molecule-substrate forces is indeed crucial for the formation of the different molecular complexes present on the surface at the monolayer stage. To understand this aspect and to determine the role played by the amino-termination, we performed DFT calculations to describe the most relevant molecular structures observed in the STM images. Moreover, we also simulated the N 1s NEXAFS spectra for the selected

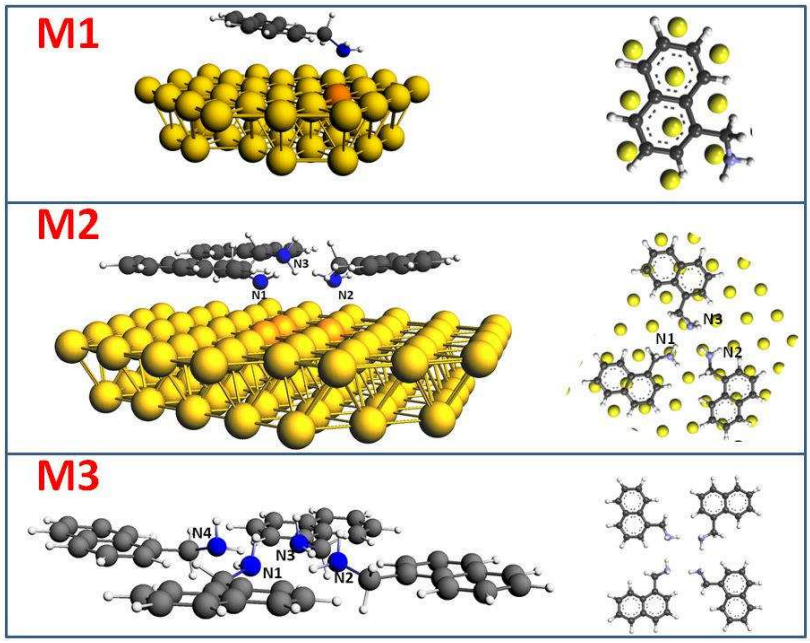

Figure 4.5: 3D and top view of the adsorption models obtained from the DFT calculations. M1 is a single NMA molecule interacting with gold via the amino termination; M2, is a trimer of molecules, where N1 and N2 terminations are interacting with gold whereas N3 termination is far from the surface and is only involved in inter-molecular hydrogen bonds; M3 is a free-standing 4-leaf clover structure of 4 NMA molecules. The Au atoms directly interacting with the N atoms are depicted in dark-gold.

structures and compared them to the experimental data. Several different adsorption configurations of NMA molecules on Au(111) surface have been considered. Some of them were discarded due to the poor agreement between experimental and simulated N 1s NEXAFS spectra and/or STM images. Here, we will discuss the DFT geometries and the simulated STM images while we will not discuss the NEXAFS spectra simulations, which can be found in the published article of this work [136].

We have then selected three configurations that, on one side, give a good agreement with the spectroscopic data and, on the other, can be considered representative prototypes of the different structures observed on the surface (fig. 4.2). The three simulated models are reported in figure 4.5: M1 represents an isolated NMA molecule interacting with the substrate through the amino termination; M2 is a cluster of three non-equivalent molecules, two of which are involved in an amino-gold interaction; M3 is a cluster of four molecules, involved in an auto-recognition process driven by the amino-amino interaction in absence of the gold substrate.

The first two models M1 and M2 were obtained by relaxing a starting configuration where both the naphthyl plane and the N–C–$C_{naphthyl}$ arms of the NMA molecules were parallel to the Au surface. Upon relaxation, in the M2 model two out of three molecules maintain their position almost unchanged with respect to the

Au surface (the N – Au distances increase to 2.56 and 2.58 Å, respectively), while the third molecule moves substantially away from the surface, keeping the parallel-to-surface orientation and reaching a final N – Au distance of 3.64 Å. The N atom (N3) of this latter molecule interacts via H-bond with one of the other two molecules (intermolecular N – H distance: 2.37 Å, close to reported experimental values for other comparable amines [144]).

With the third configuration, M3, we aim at describing the molecules involved in the 4-leaf clusters, as observed in the experimental STM images. These structures are observed almost exclusively on the reconstructed, *hcp* regions (see fig. 4.2a) of the Au(111) surface, which, as mentioned before, exhibit a lower chemical reactivity as compared to the *fcc* regions. From this observation, it can be hypothesized that for them, the surface–adsorbate interaction is relatively weak and the adsorbate–adsorbate forces prevail [137]. On the basis of this observation, we do not include the excessively long-range reconstruction of the Au herringbone in the model calculation but simply relax 4 isolated NMA molecules from an initial planar configuration. In the relaxed gas phase configuration, the four NMA molecules are coplanar and interact via H bonds regularly organized in a fan-like, chiral arrangement (each N atom interacts with the H atom of the neighboring NH_2 group), with the intermolecular N–H distances are about 2.40 Å. Subsequently, to simulate the STM images of the 4-leaf configuration, we manually placed the optimally relaxed assembly of the four isolated NMA molecules on the Au slab without further relaxation; in order to properly account for the weak interaction with the surface, the ensemble of the four NMA molecules was placed at 3.90 Åfrom the surface, an average distance value derived from our calculations on the single NMA (M1) and 3-leaf NMA (M2) complexes, where the structures were fully relaxed on the Au(111) surface.

Figure 4.6 compares in panels (a) and (c) an experimental STM image of the 4-leaf clover with that calculated from the relaxed M3 configuration. The agreement of the molecular contrast is good and highlights the substantial equivalence of the four molecules, where all nitrogen atoms are involved in hydrogen bonds with neighboring molecules.

In contrast to the regularity of the 4-leaf clovers appearing in the Au(111) *hcp* regions, as stated above, the *fcc* regions are characterized by mostly irregular structures: Figure 4.6b shows a high-resolution STM image of the latter regions, highlighting the existence of two inequivalent molecules and their mild tendency to assemble in trimers. The irregularity of these molecular assemblies originates from the interplay between amino-amino and amino-gold interactions. This interplay is governed on one side, as mentioned above, by the increased reactivity of the *fcc* regions (compared to the *hcp* regions) that favors the amino-gold interaction, and on the other, by the rotational degrees of freedom of the methylamine substituent in the NMA molecule, allowing for various, almost iso-energetic conformations. From a computational point of view, it is thus extremely challenging to investigate such disordered and chemically complex surface behavior. However, as discussed above, within a simplified, prototypical system, model M2 accounts for both the amino-

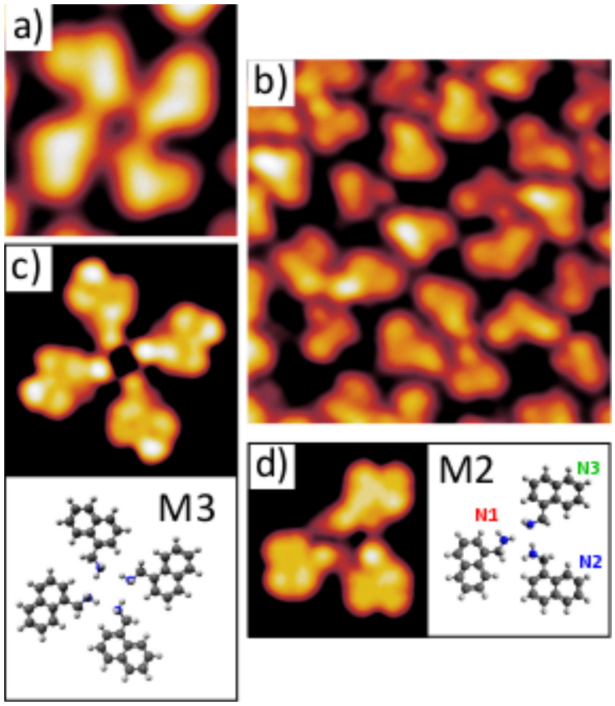

Figure 4.6: Experimental STM images of (a) a 4-leaf clover structure, commonly observed on the *hcp* regions of the Au(111) surface, and (b) the irregular complexes observed on the *fcc* regions. Simulated STM images with the corresponding ball and stick models of (c) the 4-leaf clover M3 and (d) the prototypical cluster of three molecules M2. Labels N1, N2 and N3 identify the different molecular conformations, corresponding to the nitrogen species N1, N2 and N3 in figure 4.5. Experimental image parameters: (a) $V_s = -200$ mV, $I_t = 50$ pA, 2.13×2.13 nm^2; (b) $V_s = -100$ mV, $I_t = 40$ pA, 4.41×4.41 nm^2. Simulated image parameters: $V_s = 408$ mV, ILDOS value: 1×10^{-3} nm^{-3}.

amino and the amino-gold interactions. Figure 4.6d shows the STM simulation of such complex, where two inequivalent morphologies of the molecular protrusions can be clearly identified, related to the orientation of the amino group. The first one corresponds to the NMA molecules with the nitrogen (N1 and N2 of model M2, see fig. 4.5) interacting directly with the gold substrate, and its appearance is characterized by the methylamine termination showing a separate, round-shaped protrusion. Conversely, in the second morphology, corresponding to NMA molecule interacting with the neighboring molecule through amino-amino H-bond (N3 of model M2, fig. 4.5), the main molecular protrusion appears as seamlessly joined with the methylamine protrusion. Indeed, these two distinct molecular appearances can be clearly identified in most of the structures present in the experimental image (fig. 4.6b), albeit participating in disordered molecular assemblies. This confirms that the chemistry governing such assembles consists of amino-amino and amino-gold interactions, which dictate specific orientations of the methylamine terminations giving rise to distinct appearances of the molecules in the STM images.

4.3 Standing-up phase

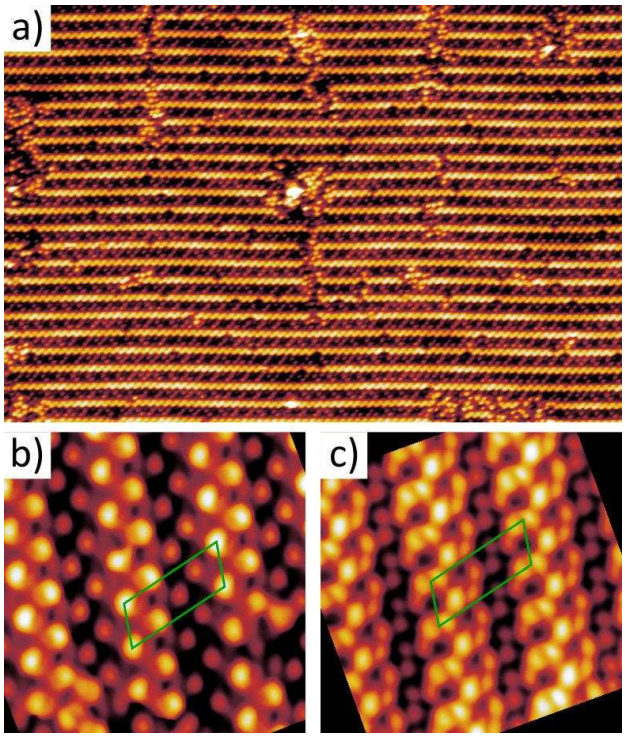

Figure 4.7: Experimental STM images of the Standing-up phase showing (a) the long-range ordered chains with minor areas where the growth of the phase is not complete and (b, c) high-resolution details of the structure of the chains recorded in different areas of the surface and likely in different tip conditions. The green box in (b, c) highlights the molecular unit cell. Image parameters: (a) $V_s = +200$ mV, $I_t = 10$ pA, 60.0×40.6 nm^2; (b) $V_s = +100$ mV, $I_t = 10$ pA, 5.00×5.00 nm^2; (c) $V_s = +25$ mV, $I_t = 10$ pA, 5.00×5.00 nm^2.

The STM images of the Standing-up phase, obtained by depositing the NMA on the sample held at $220 < T_s < 250$ K, are reported in figure 4.7. The surface is characterized by the presence of long range ordered chain-like structures, alternated with regions where the assembly process was not completed (fig. 4.7a). High-resolution images of the molecular chains recorded in different imaging conditions (fig. 4.7b and c) reveal a complex but regular assembly structure (green unit cell in fig. 4.7b). A closer inspection reveals that the structure also exhibits a chiral character (fig. 4.7c). The STM contrast is strongly dependent on the bias voltage (compare fig. 4.7b and c) as well as on the tip conditions, making it extremely difficult to infer a geometrical model for the molecules. The experimental STM image in figure 4.7b strongly resembles the appearance of a 2-Naphthalenethiol standing up monolayer on Au(111), where the different molecular contrasts were attributed to different orientations of the naphthalene rings [145]. Given the similarity of such molecule to NMA and the existence of comparable internal degrees of freedom, a similar con-

trast formation mechanism could be involved also in our case. However, it is clear that the chemistry driving the molecular assembly in the two systems is different, being dominated by the gold-sulfur interaction in the former, and by the amino-Au coupling in the latter case. In fact, the handedness of the structure suggests that the assembly cannot be simply driven by a π-stacking of the phenyl rings.

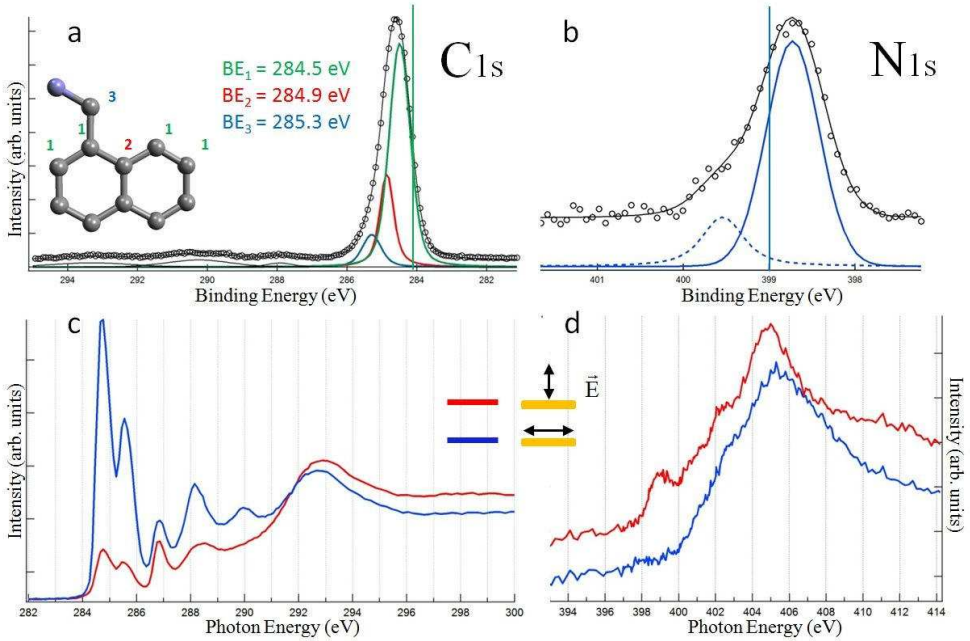

Figure 4.8: Standing-up phase. Upper panels: C 1s and N 1s XPS spectra (panels a and b, respectively). The vertical bars indicate the position of the main components of the two photoemission lines for the Flat phase. Lower panels: C 1s and N 1s NEXAFS (panels c and d, respectively). The dichroism observed at the C 1s edge is compatible with a Standing-up adsorption geometry of the NMA molecules. The nature of the N 1s peak at 399 eV is unknown.

Both XPS and NEXAFS data actually suggest that the amine terminations are directly involved in the assembly process, since their spectroscopic properties are quite different from those expected from neutral, poorly interacting groups [138].

Figure 4.8 reports the C 1s and N 1s XPS and NEXAFS spectra acquired on the Standing-up phase. The C 1s NEXAFS exhibits an inverse dichroism with respect to the Flat phase (I_π(s-pol)/I_π(p-pol) $>$ 1), indicating that the phenyl rings of the molecules are in a Standing-up configuration. From a quantitative evaluation of the dichroism, an inclination of $\sim 20^\circ$ from the surface normal is found. We note, however, that defects of the Standing-up phase may introduce regions of non-uniform distribution of molecular orientation, as can be observed in the STM images (fig. 4.7a). Therefore, we cannot unambiguously assign this angle to the molecular orientation even though we can safely state that NMA molecules are mostly vertical at this stage.

The C 1s XPS spectrum (fig. 4.8a) resembles the one we described for the Flat phase and has been fitted with the same criteria. Still, there are some significant differences. First, the shoulder at higher binding energies attributed to the amino-methyl atom is less pronounced here. Second, there is a shift toward higher binding energies of the entire C 1s peak, as evidenced by the green vertical bar depicted in the graph, which corresponds to the C 1s binding energy in the Flat phase. This can be attributed to a different screening by the substrate. In fact, molecules with increased tilt angle from the surface also increase the average distance of the C atoms within the molecule from the Au image plane, thereby reducing the Au screening of the final core-hole.

Interestingly, an opposite trend is observed on the N 1s, as reported in the figure 4.8b. The XPS peak is characterized by a main feature at 398.7 ± 0.2 eV and a minor component at 399.5 ± 0.2 eV. The latter can be ascribed to part of the molecules in the disordered regions, interacting through the electron lone pair with the substrate or neighboring molecules, which accounts for an increased binding energy with respect to their "neutral state". The position of the main component is unusual. In the Flat phase, the main component is reported at 399.0 eV as indicated here by the blue vertical bar. At the same time, the NEXAFS in figure 4.8d presents a dichroic feature at 399 eV, which is compatible neither with a free amino-group [138] nor with an amino-gold interaction [134]. The opposite shift of N 1s with respect to the C 1s together with the novel feature measured in the NEXAFS suggest that the amino-termination is involved in an interacting scheme different from the usual lone-pair mediated interaction, possibly leading to the donation of positive charge in order to explain the shifts in XPS. A possible explanation can be that a so-called NH$-\pi$ interaction [146] takes place between two adjacent NMA molecules, where the phenyl rings act as acceptors of one of the hydrogen atoms of the amino-groups. This kind of interaction is fundamental in many biological systems [146–149] and represents one of the recognition schemes which the phenyl rings can be involved in. In our system, this recognition process could be driving the assembly of the Standing-up phase. In this view, part of the shift to the higher binding energies we observe in the C 1s peak should be ascribed as well to the intermolecular interactions, instead of being a purely screening-related effect. Albeit suggestive, the NH$-\pi$ interaction scheme cannot be unambiguously confirmed by the interpretation of the complex structures we observed in STM and remains only a plausible explanation of our results.

4.4 Condensed phase

Figure 4.9 reports the STM images and the XPS spectra of the system obtained by annealing an NMA monolayer to 400 K. The n-leaf clover phase is not visible anymore. The morphology of the system is characterized by the presence of novel structures. The naphthalene bodies of the NMA molecules can still be identified. However, most of them are involved in the formation of dimers, as evidenced in the inset of

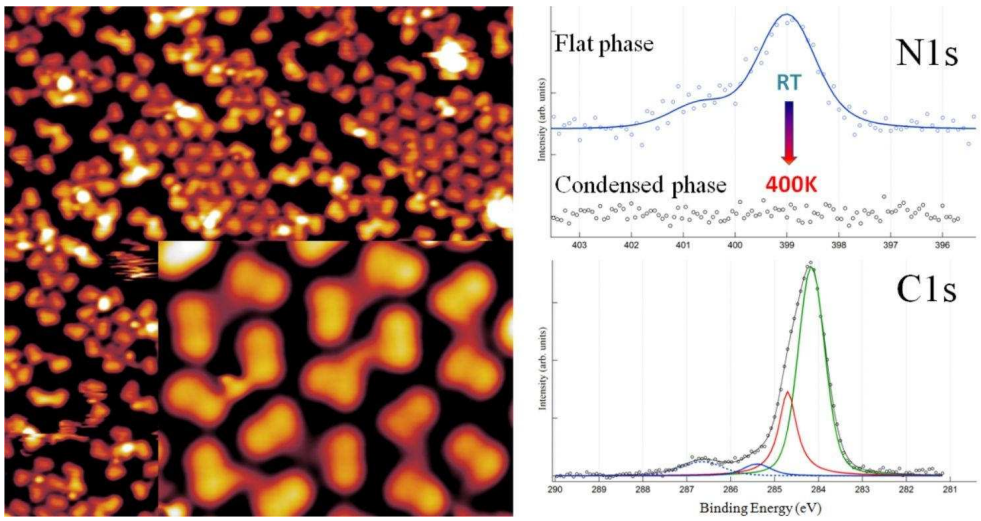

Figure 4.9: The Condensed phase. Left panel: STM image of the Condensed phase. Most of the molecules form dimers (see the inset) even if several morphologically different structures can be observed. Right panel: N 1s XPS spectra acquired on the Flat phase and on the Condensed phase evidence the complete de-amination of the system in the latter. C 1s signal of the Condensed phase reveals two components related to the methyl-termination of NMA (at ~ 286.7 eV and ~ 285.4 eV), possibly indicating different chemical configurations for the dimerized molecules. Image parameters: left panel: $V_s = +100$ mV, $I_t = 20$ pA, 20.0×20.0 nm^2; inset: $V_s = +30$ mV, $I_t = 100$ pA, 4.00×3.10 nm^2.

figure 4.9. From the morphology in the STM images it appears that the dimers are not all equivalent and isolated molecules are also visible on the surface.

The XPS spectra reveal the chemical nature of the structures. No peaks are detected in the N 1s region, as evidenced in the right-top panel of figure 4.9 by the comparison with the Flat phase in figure 4.3. The system has therefore undergone a de-amination process upon annealing at 400 K. The C 1s peak profile has changed with respect to the Flat phase (see fig. 4.4). In particular, the intensity of the methyl component close to 285.4 eV decreased; at the same time the intensity of the component at 286.7 eV, previously detected as a minor component in the Flat phase, is here more pronounced. We relate both components to the de-aminated methyl terminations, involved in different interactions in the non-equivalent species present on the surface. The de-amination on the poorly reactive Au(111) surface has been already reported for the octylamine molecule [150]. In that case, the process was not complete and residual amino-groups were observed after the thermal treatment, probably due to steric constraints of the system.

4.5 Conclusions

The chemistry of the methylamine functional group on the Au(111) surface has been investigated by studying the self-assembly properties of the NMA molecules

at three different phases. The Flat phase (formed at intermediate temperatures) is characterized by the interplay between the molecule-molecule and molecule-substrate interactions. Most of the NMA molecules on the surface are found to form clover-like clusters. By means of NEXAFS spectroscopy and DFT calculations we determined the role of the amino-termination in the assembly. On one hand, an auto-recognition process takes place between the amino-groups of NMA molecules, driving the formation of the clover structures. On the other hand, the formation of this hydrogen-bonding scheme can be affected by the direct interaction between the $-NH_2$ group and the gold substrate, resulting in irregular molecular clusters, as evidenced by the STM images. The occurrence of amino-gold interaction is confirmed by both NEXAFS spectroscopy and DFT calculations. We also show how the growth of an NMA monolayer at low temperatures (Standing-up phase) leads to a quite complex architecture: from the value of the N 1s binding energy, we propose an interacting scheme where the amino groups act as proton donors to the phenyl groups of the adjacent molecules. Finally, we identified a third phase (Condensed phase) obtained upon thermal annealing of the Flat phase, in which the complete de-amination of the NMA molecules is observed, with the formation of covalently bound molecular dimers.

The results we presented describe the different interacting schemes the methylamine termination can be involved in, on a poorly reactive substrate. In particular, we demonstrated how the functional group can be first exploited to drive the assembly of the molecules and then thermally activated so that the molecules are de-aminated and a covalent intermolecular interaction can be promoted. We believe that this on-surface condensation process can be extended to other molecules with a methylamine termination, representing an efficient and promising method to grow stable organic templates on poorly reactive metal surfaces. As last remark, as we will show in the next Chapters 6 and 7, the understanding of the behaviour of a methylamino-terminated molecule on Au(111) is at the basis of novel hetero-organic supramolecular assemblies.

Chapter 5

Aminophenyl porphyrin chains on Au(111)

Among all the molecules employed for potential applications in the field of organic electronics (such as catalysis, solar cells, sensors, and electrochemistry [2, 151]), porphyrins have attracted particular attention. As organic semiconductors, porphyrins exhibit good properties in terms of both stability and electronic transport. Moreover, the inner part of the heme group is constituted by a porphyrin: the assembly of these molecules can therefore mimic important biological processes like the delivery of oxygen in the tissues. Porphyrins can also be functionalized with a wide range of terminations and they can incorporate at their center a metal atom, which can tailor their electronic properties.

Single molecules and self-assembled monolayers of porphyrins on metal surfaces have been widely studied in literature from both the structural and the electronic points of view. In particular, STM is used to characterize *in situ* single porphyrins on surfaces, while X-ray spectroscopic techniques are used to characterize the electronics and chemistry of self-assembled monolayers or thin films. However, to realize molecular electronic devices, nonperiodic assemblies of molecules may be required [152]. For this reason, in the last decade researchers made an effort to understand how to control the assemblies of molecules into the desired organic architectures [151–153]. In particular, one-dimensional molecular chains have attracted interest because they are promising candidates to be employed, for instance, as organic wires into organic circuits. The possibility to functionalize porphyrins makes them suitable to be used as building blocks to produce any sort of assembly, especially organic chains. Several studies have reported many properly functionalized porphyrins forming chains through hydrogen bonds [41, 154, 155], covalent bonds [156, 157], or metal-organic bonds [155, 158–161]. The functional groups and the interaction of porphyrins with the metal substrate determine the geometric and electronic structure of such organic chains. Moreover, porphyrin molecules have been proposed as single molecule switches, where inner hydrogen tautomerization [162, 163] or molecule conformational changes [12, 164, 165] on a metal substrate

are at the basis of the molecular conductance switch.

Hydrogen bond based organic chains are of fundamental importance since they can represent precursors to covalent or metal-organic bonded chains. In particular, as we have learned from the NMA on Au(111) system in Chapter 4, primary amines ($-NH_2$) can establish hydrogen bonds with each other and can interact with a metal substrate via weak bonds involving the electron lone pair of their amino group. The N–Au donor-acceptor bond has been employed to form molecule-gold junction for single molecule conductance studies [132, 134, 166], and charge transfer between amines and gold substrates has been proved to be promising, showing a very fast N–Au charge delocalization [135].

In this Chapter, we study the behavior of an aminophenyl-functionalized porphyrin on the Au(111) surface to investigate the role of the amino-amino and amino-gold interaction in the assembly of this macromolecule. Our combined STM experiments and DFT calculations reveal that these porphyrins form chains via their amino-terminations through a donor-acceptor mechanism. Moreover, we demonstrate that these porphyrins in the acceptor configuration tend to trap at their center charged gold adatoms, intrinsically available on the gold substrate (as we showed with DMSO/Au(111) in Chapter 3).

Furthermore, we investigated the switching properties of each TAPP molecule within these wires. We find out that the donor TAPPs can undergo two different types of switching, both being binary: hydrogen tautomerization when partially deprotonated (with only one inner hydrogen), or a two-state conformational change when fully deprotonated (with no inner hydrogen). By means of combined STM experiments and DFT calculations, we show that also the switching related properties are strongly influenced by aminopehnyl-terminations of the molecules.

This work, where I contributed with most of the STM experiments, is in preparation for submission to a journal.

5.1 The TAPP molecule

In figure 5.1a the chemical structure of 5,10,15,20-tetra(4-aminophenyl)porphyrin (TAPP), commercially available from PorphyChem (purity 98%), is shown. TAPP is basically a tetraphenylporphyrin functionalized with four amino terminations. TAPP was evaporated from a Knudsen cell at 520 – 570 K on a clean monocrystalline Au(111) sample at room temperature. Before evaporating TAPP on Au(111), several hours of outgas at 500 – 520 K are needed to purify the molecule from contaminants.

Figure 5.1b shows a STM image of TAPP molecules on Au(111), where TAPP form chains along the herringbone reconstruction of the substrate. After a closer look to these chains (fig. 5.1c), two questions arise: What is the interaction linking TAPPs in the chain? Why do TAPPs appear in the STM images alternately different in the chain?

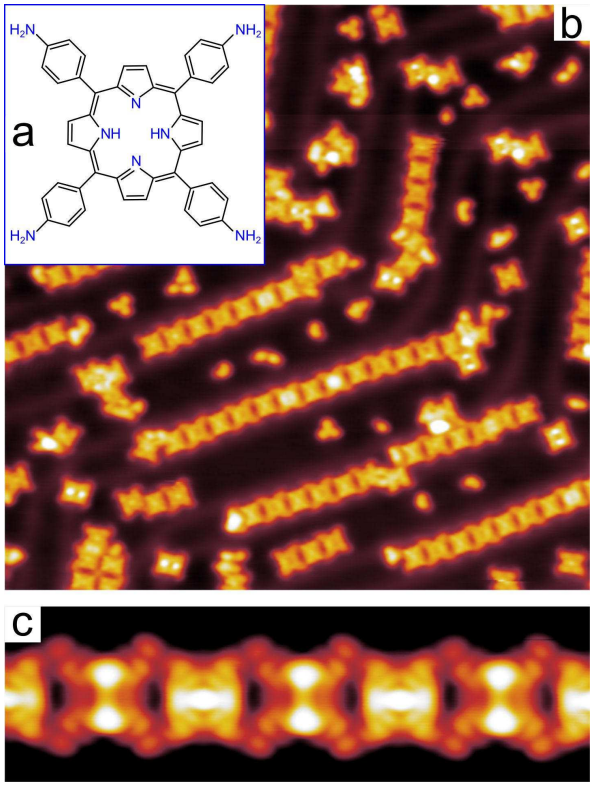

Figure 5.1: (a) Chemical structure of 5,10,15,20-tetra(4-aminophenyl)porphyrin (TAPP). (b) TAPP chains on Au(111), the length of these chains being limited by the herringbone reconstruction of the surface. (c) High resolution image of a TAPP chain, where the alternated appearance of the molecules is evident. Image parameters: (b) $V_s = -0.2$ V, $I_t = 0.2$ nA, 40×40 nm^2; (c) $V_s = -1.0$ V, $I_t = 0.3$ nA, 10.0×3.0 nm^2.

5.2 TAPP chains: the donor-acceptor model

The most intuitive answer to the first question is that TAPPs form chains via some hydrogen bonds between their amino terminations. The length of these chains is limited by the herringbone reconstruction of the substrate (see fig. 5.1b), suggesting some weak interaction between the molecules, which form instead a compact monolayer at high coverage for steric effects (see fig. 5.4a). Moreover, it is possible to separate one by one each TAPP from the chains by STM manipulation (not shown). This fact further supports the hypothesis of a weak hydrogen bond between TAPPs. Each N atom of an amine has an electron lone pair which can interact with one hydrogen atom of a neighbor amine, or with the gold substrate [43, 134].

To understand how such bonds are formed, we performed DFT simulations on this system, in collaboration with Dr. Simone Velari and Prof. Alessandro De Vita of the University of Trieste (see also ref. [76] for details about the DFT calculations). First, a single TAPP on Au(111) surface is modelled. DFT suggests that the most

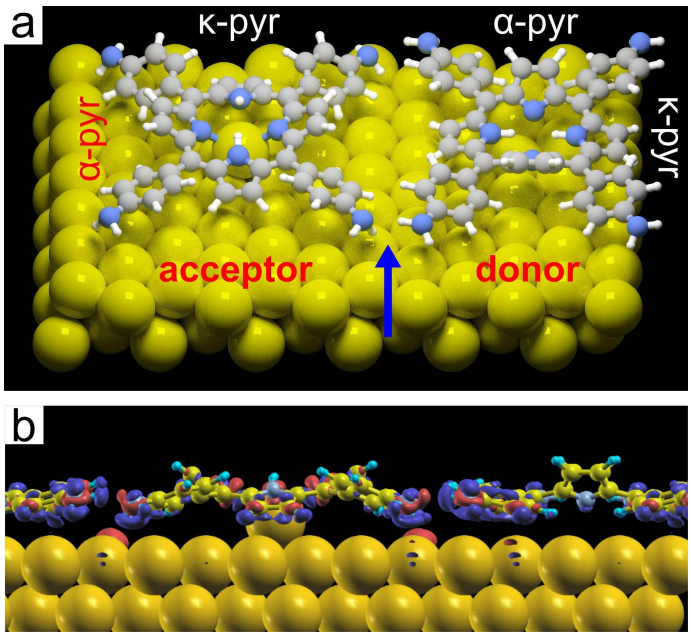

Figure 5.2: (a) Stick and ball model obtained by the DFT calculation of a TAPP chain, where a blue arrow indicates an acceptor-donor hydrogen bond between two amino terminations. Notice the "orthogonal" disposition of the acceptor with respect to the donor, meaning that the two opposite κ-pyrroles directions inside the two saddle-TAPPs are perpendicular, and the gold adatom at the center of the acceptor. (b) Lateral view of the changes in charge density in a TAPP chain. The accumulation of negative charges is despicted in red, the depletion in blue.

stable geometry is characterized by a saddle-shaped macrocycle, where the two N atoms of opposite pyrrole rings are tilted upwards, which (following the notations in ref. [163]) we call κ-pyrroles, or downwards, which we call α-pyrroles. The two inner hydrogens are located on the two κ-pyrroles. The aminophenyl terminations are slightly twisted with respect to the surface plane. This is the most stable configuration for a single TAPP on Au(111), and we call it the saddle-TAPP (see also fig. 5.2a, where the "donor" TAPP has a geometry very similar to the isolated saddle-TAPP). We point out that the saddle-shaped macrocycle and the tilted phenyls are geometries typical of phenylporphyrins in gas phase or adsorbed on metal surfaces, as widely reported in literature [154, 163, 167–170].

Subsequently, as shown in figure 5.2a, we simulate a system consisting of two TAPP molecules on Au(111): because of the periodicity of the unit cell, this represents an ideal endless TAPP chain. We put two TAPPs close to each other, at a distance compatible with the experimental one. After comparing many possible configurations, we conclude that the best model (shown in fig. 5.2a), *i.e.* the energetically most stable and with the simulated STM images that best match the experimental ones, is obtained by placing two saddle-TAPPs one perpendicular to the other, meaning that the two opposite κ-pyrroles directions inside the two saddle-

TAPPs are perpendicular. Upon DFT relaxation, starting from this configuration the aminophenyl terminations tilt into a geometry that favors the interaction between the NH_2 terminations of the two neighboring molecules. The DFT simulations confirm thus our initial hypothesis, showing the lone pair of a N atom of the TAPP on the left (fig. 5.2a) interacting with a proton of the amino group of the TAPP on the right, as indicated by the blue arrow in figure 5.2a, thereby establishing an amino-amino hydrogen bond. We point out that a similar alternate change in the molecular orientation along a molecular chain has been recently observed also in Fe-porphyrin metal-organic chains on Au(111) [171].

Therefore, at the point indicated by the blue arrow in figure 5.2a, the TAPP on the right is donating a proton to the TAPP on the left, and both molecules must have the same behavior on all their four aminophenyl terminations since, as suggested by figure 5.1c, each TAPP is symmetric with respect to both its vertical and horizontal axes. Thus, in the TAPP chains, each molecule behaves alternately as an acceptor (fig. 5.2a, left) or as a donor (fig. 5.2a, right) as a whole, *i.e.*, TAPP has an amphiprotic behavior within such chains.

In figure 5.2b the changes in charge density around the TAPP – gold interface are shown, calculated as $\rho_{tot}(\mathbf{r}) - \rho_{sub}(\mathbf{r}) - \sum \rho_{mol}(\mathbf{r})$, where $\rho_{tot}(\mathbf{r})$ is the charge density of the total system, $\rho_{sub}(\mathbf{r})$ the density of the gold substrate, and $\sum \rho_{mol}(\mathbf{r})$ the density of non-interacting TAPP molecules in gas phase (the same formula used in section 3.8). The charge density changes are mostly located around the aminophenyl terminations, where the interaction between the amines takes place.

5.3 TAPP chains: trapping of gold adatoms

To answer the second question, *i.e.*, the reason why TAPPs in a chain appear alternately different, we hypothesize the presence of a gold adatom at the center (underneath) of the acceptor TAPP, as one can notice in the model in figure 5.2a (TAPP on the left). Indeed, as will be shown in the following, the donor-acceptor states alone cannot explain such a difference in the appearances (density of states) of the acceptors and donors in the STM images. We remind that it is well known that native gold adatoms on Au(111) can detach from surface steps and diffuse across the surface terraces where, due to their charged state related to their undercoordination, they can interact with molecules with cyano (CN) groups [47, 48, 58, 161, 172], sulfur [65, 66], or small solvents [43], as we showed in Chapter 3 with DMSO trapping gold adatoms.

Figure 5.3a shows an experimental STM image where two acceptors have different appearances: the first one, which we name acceptor-1, appears similar to its neighbor donor TAPP (rotated by 90°), while the second one, which we hypothesize has an adatom underneath and we name acceptor-2, has a bright protrusion at its center. Most of the acceptors found on the sample have the bright protrusion at their center (acceptor-2), while the ones without the bright protrusion (acceptor-1) are rarely found. Therefore, our hypothesis is that the particular geometry and elec-

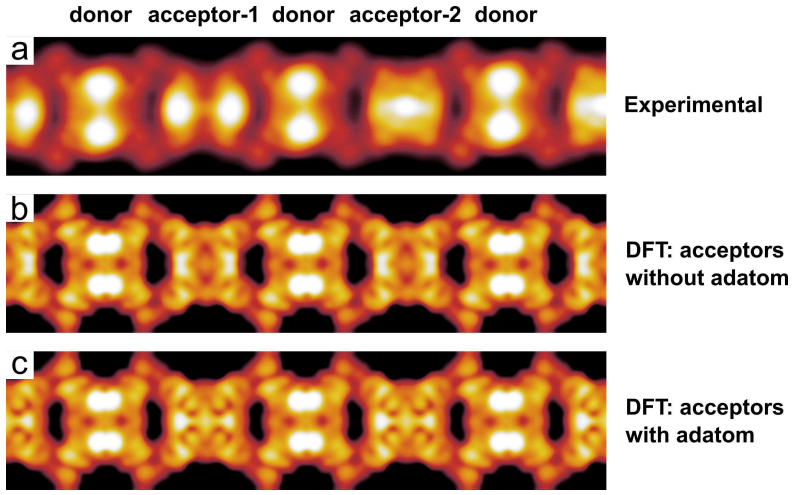

Figure 5.3: Comparison between an experimental STM image with two simulated ones. (a) Experimental image of a TAPP chain showing an acceptor-1 and an acceptor-2. (b) Simulated STM image of the model with the acceptors without adatom at their center. (c) Simulated STM image of the model with the acceptors modeled with an adatom at their center. Image parameters: (a) $V_s = -1.0$ V, $I_t = 0.2$ nA, 10.0×2.3 nm^2.

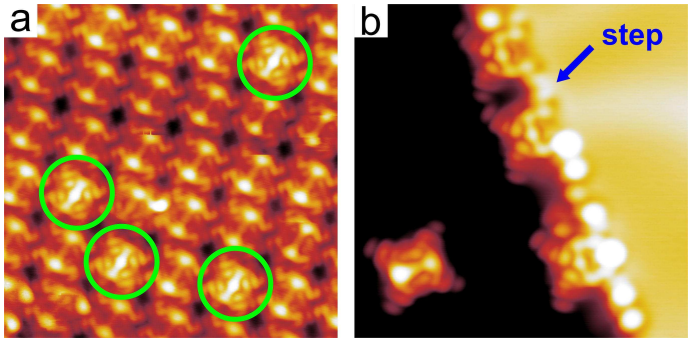

Figure 5.4: (a) TAPP in compact monolayer phase, where some molecules with a bright protrusion at their center are circled. These have the same appearance as acceptors-2 and have likely an adatom at their center. (b) TAPP at a surface step all having a bright protrusion, while on the terrace a single isolated TAPP does not have the same bright protrusion. Image parameters: (a)$V_s = -1.0$ V, $I_t = 0.5$ nA, 9.0×9.0 nm^2; (b) $V_s = -1.0$ V, $I_t = 0.5$ nA, 8.0×8.0 nm^2.

tronic structure of TAPPs in the acceptor state allow them to trap adatoms at their center. Figure 5.3b shows a simulated STM image where acceptors have no adatoms trapped, while Figure 5.3c shows a simulated STM image where each acceptor has an adatom underneath. By comparing these images with figure 5.3a, it is clear that the acceptor-1 is similar to the acceptors in figure 5.3b, while the acceptor-2 is more similar to the ones in figure 5.3c. Therefore, the simulated images support our theory: the bright protrusion at the center of the acceptors-2 must be associated to a

gold adatom underneath each of them. We stress that the simulated images in figure 5.3b, c are in good agreement with the experimental images, where also the donors and the aminophenyl terminations are well reproduced.

The metalation process of porphyrins has been widely studied in literature, especially their self-metalation on metal surfaces, such as Cu, Fe or Ni [173–178], and their direct metalation by evaporating metal atoms on the surface [179–181]. To metalate, porphyrins need to undergo a partial dehydrogenation process, *i.e.*, lose their two inner hydrogens. However, in our case, TAPP acceptors-2 do not metalate (the model in fig. 5.2a has still the two inner hydrogen atoms), but rather trap one gold atom underneath, via a coordination bond between the N atoms of the two α-pyrroles and the adatom. Indeed, the simulated STM image of the model in which the acceptor is metalated does not match the experimental ones (not shown).

In the literature, no study of direct metalation of porphyrins with gold atoms on surfaces has been reported till now, likely because the size of gold atom prevents its spontaneous metalation into a porphyrin. In a recent work, Mielke *et al.* [61] demonstrated that gold adatoms can be trapped underneath porphyrins on Au(111). In their STM images, they find two types of porphyins: "bright" and "dark", and they show that the "bright" porphyrins have a gold adatom underneath. This is similar to what we observe in our STM images: TAPP acceptors-2 are "brighter" than acceptors-1 because they trap one gold atom underneath (actually, the relative brightness strongly depends on the bias). When the TAPP coverage is high enough, they assemble into a compact phase (in analogy with simple tetraphenylporphyrins [61]) for steric effects, as shown in figure 5.4a. In this compact monolayer we find two types of TAPP, one similar to the donor or acceptor-1 of TAPP chains while the other, having a bright protrusion at their center, appears similar to the acceptors-2. This is exactly what Mielke *et al.* observe for tetraphenylporphyrins on Au(111), where brighter molecules are demonstrated to have gold adatoms underneath. Furthermore, the acceptors-2 and the bright TAPPs in the compact phase appear very similar to the TAPPs adsorbed at the surface steps, where adatoms are likely to be entrapped at the center of the molecule lying across the steps (fig. 5.4b). Indeed, as mentioned in the work regarding DMSO in section 3.6, native gold adatoms on Au(111) can easily detach from the surface steps [68, 92, 93], and therefore it is reasonable that TAPPs at steps have adatoms underneath. This fact further supports our hypothesis of an adatom trapped at the center of the acceptor TAPPs.

5.4 TAPP chains: binary switch

To be potentially suitable for devices, a molecule must exhibit electronic properties such as switching [20, 163, 182] or rectification [183]. In this context, porphyrin molecules have been proposed as single molecule switches, where inner hydrogen tautomerization [162, 163] or molecule conformational change [12, 164, 165] on a metal substrate are at the basis of the conductance change. Therefore, after characterizing the structure of the TAPP chains, we investigated the possible switching

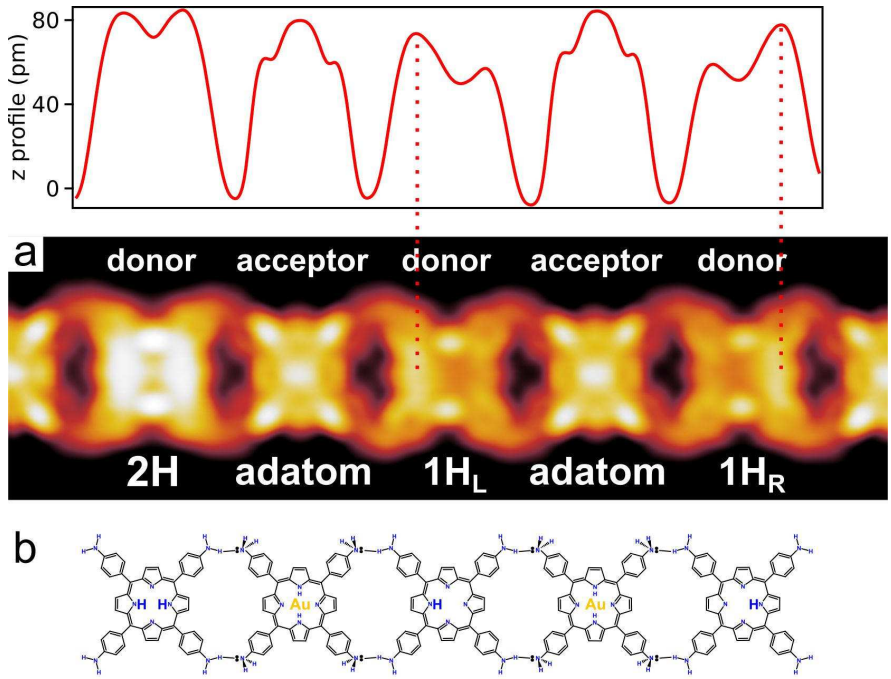

Figure 5.5: (a) High resolution STM image of a section of a TAPP chain at a bias of −0.2 V, with its z-profile, acquired along the horizontal symmetry axis of the chain, that highlights the asymmetry of the 1H-TAPPs. (b) The chemical structure model of the same TAPP chain, where the donor-acceptor model and the different internal structures of each TAPP are showed. From left to right: donor with both inner hydrogen (2H), acceptor with one gold adatom, donor with one inner hydrogen on the left κ-pyrrole ($1H_L$), acceptor with one gold adatom, donor with one inner hydrogen on the right κ-pyrrole ($1H_R$). Image parameters: (a) $V_s = -0.2$ V, $I_t = 0.5$ nA, 10.0×3.0 nm^2.

properties of each TAPP molecule within the chains.

The high resolution STM image in figure 5.5a shows details of five TAPP molecules in a chain, whose z-profile (acquired along the horizontal symmetry axis of the chain) highlights the different symmetries of each TAPP. The two acceptors have the same symmetric z-profile, and the donor on the left is characterized by two identical peaks, whereas the other two donors have two different asymmetric profiles. By comparing our STM images with previous results from the literature, we hypothesize that the asymmetric TAPPs are partially deprotonated molecules, which have lost one inner proton (see also fig. 5.5b), which we name thus 1H-TAPP. In all the works in literature, when there is an asymmetry due to the presence of hydrogen atoms, in the STM images the higher (brighter) side will correspond to the presence of the hydrogen atom(s) [163, 184, 185]. Therefore, in figure 5.5a, as shown in panel b from left to right, we suppose that the first donor TAPP has both two inner protons (2H), the second donor has a single inner proton on the left κ-pyrrole ($1H_L$), and the last donor has a single inner proton on the right κ-pyrrole

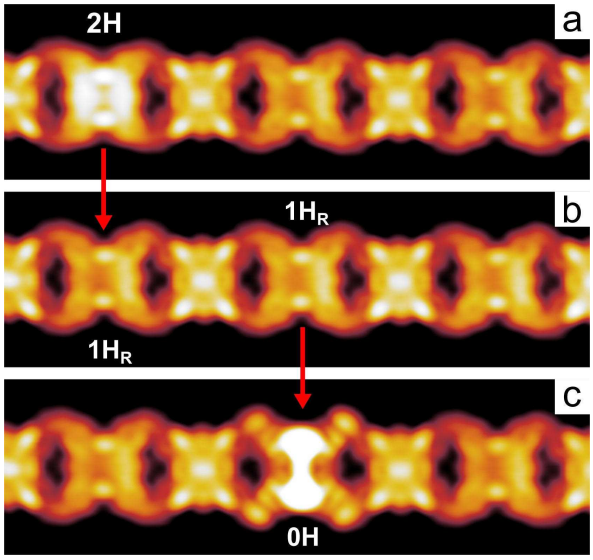

Figure 5.6: Sequential deprotonation of single TAPP molecules in a TAPP chain on Au(111). (a) A 2H-TAPP is deprotonated into (b) an 1H-TAPP by applying a −1.2 V bias on the center of the molecule. (b) An 1H-TAPP is deprotonated into an (c) 0H-TAPP by applying a −2.0 V bias on the center of the molecule. Image parameters: $V_s = -0.2$ V, $I_t = 0.5$ nA, 10.0×3.0 nm^2.

(1H$_R$). We point out that the different appearance of TAPPs in figures 5.1c and 5.5a is due to a different bias voltage: In figure 5.5a, at a bias of −0.2 V, the asymmetry due to the inner protons is better highlighted.

STM manipulation: deprotonation. Figure 5.6 shows a sequence of three STM images where controlled deprotonation of TAPP donors was obtained by centering the STM tip above the molecule and increasing the bias voltage over a certain threshold [163]. A 2H-TAPP (fig. 5.6a) is deprotonated into an 1H-TAPP (fig. 5.6b) by applying a −1.2 V bias onto the center of the molecule. Subsequently, an 1H-TAPP (fig. 5.6b) can be deprotonated into a 0H-TAPP (fig. 5.6c) by applying a −2.0 V bias onto the center of the molecule as well. Such deprotonation reactions seem to be irreversible, since we have never observed a re-hydrogenation reaction. We must point out that, actually, the first stage deprotonation, *i.e.* from 2H-TAPP to 1H-TAPP, is also induced thermally when TAPP is evaporated at 520 − 570 K from the UHV evaporator. Indeed, in our images we find most of the donors as 1H-TAPP, *i.e.* already partially deprotonated, while 2H-TAPPs are less commonly found. However, 0H-TAPP are never found spontaneously on Au(111), suggesting that the thermal energy is insufficient to overcome the barrier to remove also the second proton. We point out that, when TAPPs undergo deprotonation, a hydrogen atom is likely removed, although no satisfactory experimental proof of this hypothesis has been reported so far. However, even if just a proton is removed, the deprotonated TAPP would be a stable molecule since its charge would be balanced by the gold substrate.

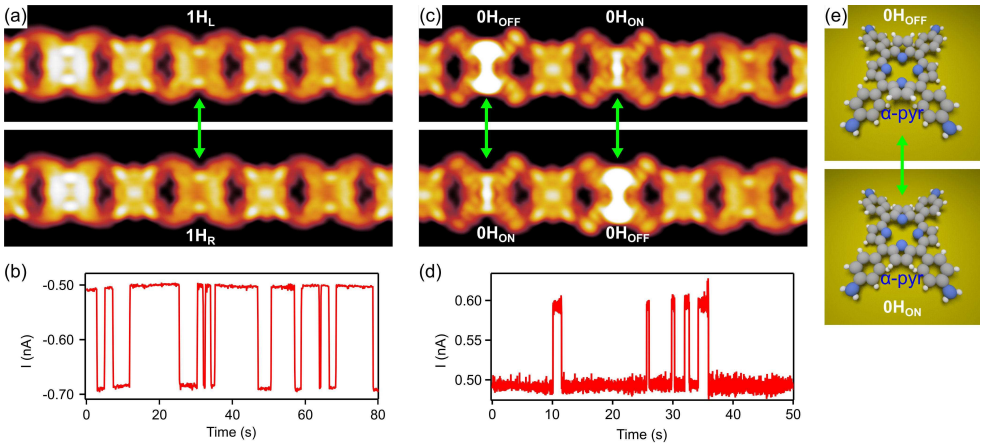

Figure 5.7: Switching in 1H-TAPP and 0H-TAPP. (a) Binary H-tautomerization in the central 1H-TAPP and (b) $I(t)$ trace recorded on it at bias of -1.5 V, with the tip in a slightly asymmetric position with respect to the molecule center. (c) Binary conformational switch in two 0H-TAPPs and (d) a typical $I(t)$ trace recorded at their center at bias of $+1.0$ V. (e) Tentative model illustrating the conformation switch of a 0H-TAPP, where the two α-pyrroles change their angle tilt. Image parameters: (a) and (c) $V_s = -0.2$ V, $I_t = 0.5$ nA, 10.0×3.0 nm^2.

STM manipulation: tautomerization. We therefore studied the hydrogen tautomerization, *i.e.* the flip of the inner protons in different sites, in each TAPP within such chains. The reaction can be induced by positioning the STM tip above the molecule and increasing the bias voltage below the HOMO or above the LUMO resonance of the molecule [162], while simultaneously monitoring the current signal in the constant height mode, *i.e.* recording the current versus time $I(t)$ spectra. In this way the tautomerization reaction is induced by excitation via inelastic electron tunneling into the molecules [162, 186], and different current values are associated to different proton positions. In the acceptor TAPPs no H-tautomerization switching was found, likely due to the presence of the adatoms which hinder this process. In the donors we find no switching in 2H-TAPPs, while we find a binary H-tautomerization in 1H-TAPPs where the inner hydrogen atom can "jump" only between the κ-pyrroles, as shown in figure 5.7a.

These findings are in contrast to what found so far in literature, where the 2H-porphyrins are found to be readily switchable [163, 186–188] and 1H-porphyrins can switch into all the available pyrroles sites [163]. Apparently, here, in the donors, the α-pyrroles cannot bind any hydrogen atom. It is known that the molecule-substrate interaction can strongly influence the conformation of the molecules [189], and thereby also the possible tautomerization reactions [162]. In our case, the observed restriction of the tautomerization to only two sites (the κ-pyrroles) can be explained by our DFT model in figure 5.2a: the two protons in the donor 2H-TAPP are located on the two κ-pyrroles, while the two α-pyrroles are bent towards the surface thereby

Table 5.1: HOMO-LUMO and gap in each type of TAPP. Multiple Gaussian peaks are fitted to the spectra to determine the HOMO and LUMO positions.

TAPP type	**HOMO** (eV)	**LUMO** (eV)	**Gap** (eV)
Isolated 2H-TAPP	−0.40	+1.36	1.76
Acceptor with adatom	−0.68	+1.56	2.24
2H-TAPP	−0.84	+0.52	1.36
1H-TAPP	−0.54	+1.16	1.70
0H-TAPP OFF	−0.18	+1.72	1.90
0H-TAPP ON	−0.21	-	-

interacting through their nitrogen atom with the substrate, likely preventing them from binding hydrogen atoms. In the two previous sections we have showed that the interaction between the NH_2 terminations of the TAPP molecules is responsible for the chain formation and trapping of gold adatoms by the acceptors. Since the geometry of the TAPPs within the chains is also dictated by the aminophenyl terminations, and two H-switching channels in each molecule are inhibited by the geometry of the TAPPs, we deduce that the aminophenyl functionalization indirectly influences also the H-switching within the molecules.

STM manipulation: conformation switch. Interestingly, also the fully deprotonated 0H-TAPP is found to be reversibly switchable in two different states, which we call $0H_{OFF}$ and $0H_{ON}$, as showed in figure 5.7c. This switch cannot be due to tautomerization since there are no inner protons left. Therefore, the observed change in the appearance is likely related to a conformational change. It is known that porphyrins can undergo a conformational switching under the electric field or inelastic electron tunneling [164]. Here, due to the geometrical constraint imposed to the molecule by the amino-amino and amino-gold interaction, the conformational change is likely due to the α-pyrroles since there is a strong contrast change at their position after a switch, as one can see from figure 5.7c.

Figure 5.7b shows a typical $I(t)$ (current versus time) trace recorded on a 1H-TAPP at bias of -1.5 V, where the two current values indicate the binary switching between $1H_L$ and $1H_R$. The switching rate and ratio between the two states depend on the bias applied and tip position on 1H-TAPP. Figure 5.7d shows a typical $I(t)$ trace recorded on the center of a 0H-TAPP at bias of +1.0 V, where the two current values indicate the binary switching between $0H_{OFF}$ and $0H_{ON}$. Here, the $I(t)$ trace suggests that one state is less stable than the other, since there is no asymmetry argument to justify it. By comparing the STM images before and after the $I(t)$ traces we conclude that the most stable state is $0H_{OFF}$.

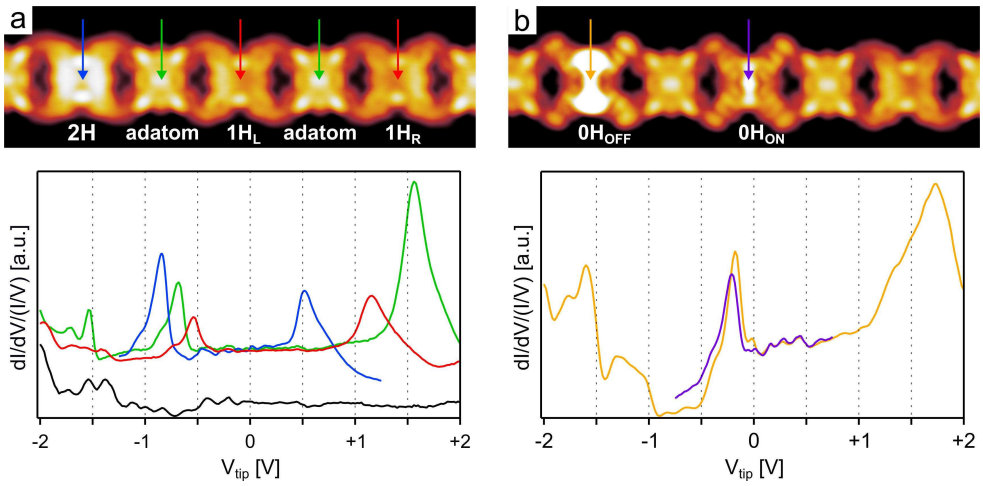

Figure 5.8: dI/dV spectra recorded at the center of single molecules in TAPP wires, where each color indicates a different type of TAPP. (a) dI/dV spectra of 2H-TAPP (blue), acceptor TAPP trapping an adatom (green), and 1H-TAPP (red). The blue spectrum is limited in the $[-1.25; +1.25]$ V range, otherwise 2H-TAPP undergoes deprotonation. The black spectrum at the bottom is acquired on the Au(111) substrate for comparison. (b) dI/dV spectra of oH_{OFF} (orange) and oH_{ON} (violet). The violet spectrum is limited in the $[-0.75; +0.75]$ V range because for higher bias oH_{ON} switches to oH_{OFF}.

5.5 TAPP chains: STS spectroscopy

The different donor-acceptor and 2H-, 1H-, oH states of TAPPs have different geometrical and electronic structures. Figure 5.8 shows dI/dV spectra recorded at the center of single molecules within the TAPP wires, while table 5.1 summarizes the HOMO-LUMO peak positions and gaps of each spectrum. Clearly, every TAPP in a wire has a different electronic structure with respect to single isolated TAPP molecules (see table 5.1). In particular, 1H-TAPP (both $1H_L$ and $1H_R$) has both HOMO and LUMO shifted towards higher energies (fig. 5.8a) with respect to 2H-TAPP and, moreover, has a wider HOMO-LUMO gap, suggesting that the deprotonation affects the transport properties. Similarly, oH-TAPP (oH_{OFF}) has both HOMO and LUMO shifted towards higher energies and a wider HOMO-LUMO gap with respect to 1H-TAPP (fig. 5.8b). Interestingly, the acceptor TAPP trapping one adatom has the largest HOMO-LUMO gap; this is probably due to the cationic nature of the gold adatom [43] (see also section 3.8) which acts as an acceptor for the electrons of the TAPP, and thus deeply modifies the electronic density of the porphyrin.

5.6 Conclusions

In conclusion, in the present work, we studied an aminophenyl-functionalized porphyrin (TAPP) on Au(111), and we have shown that the interplay between the intermolecular amino-amino interaction and the molecule-gold interaction is responsible

of the TAPP assembly into molecular chains. Our combined experimental STM images and DFT calculations demonstrate that TAPPs interact via amino-amino bonds of their terminations to form such chains, where each TAPP behaves alternately as a hydrogen donor and acceptor as a whole. Moreover, in the STM images, most of the acceptors have a bright protrusion at their center, which, by comparing experimental and simulated STM images, we demonstrate to be associated to a gold adatom located just below their center. The TAPP molecule is coordinated to the adatom via the N atoms of the two pyrroles without the proton terminations (α-pyrroles).

Furthermore, we have investigated the switching properties of each TAPP, namely H-tautomerism and conformation change, in these molecular wires. The partially deprotonated 1H-TAPP is found to be characterized by a binary H-tautomerization switch on the κ-pyrroles along the TAPP wire. Moreover, the fully deprotonated 0H-TAPP is showed to be switchable into two different conformational geometries. The interplay between the amino-amino and amino-gold substrate interaction dictates the geometry of each molecule and thereon the number of switch channels available for the H-tautomerization reaction and conformational change.

Finally, we have reported the dI/dV spectra which show that the donor/acceptor states (and thereby the adatom trapped by the acceptor), and the different switching states have very different electronic structures (HOMO-LUMO levels). Our studies reveal for the first time how the competitive amino-amino and amino-gold interaction can modify the geometry and electronic structure in a porphyrin, as well as control the symmetry of the possible tautomerization pathways and conformational switching. These properties highlight the amino-terminations as an intriguing functionalization for molecules employed in the research on organic electronics and devices.

Part II

Amino-carboxylic hetero-architectures on Au(111)

Chapter 6

A competitive amino-carboxylic hydrogen bond on a gold surface

The supramolecular assembly on surfaces has been widely investigated in the last decade as a key towards an effective device engineering at the nanoscale. Organic architectures on metal surfaces can be obtained by exploiting both covalent and non-covalent bonds between the molecules or by building metal-organic frameworks [34–36, 157, 190]. The interplay between molecule-substrate and molecule-molecule interactions drives the formation of the (hetero-)organic architectures and determines the morphological and chemical properties of the systems. A proper control on the self-assembly process is therefore the mandatory requirement to obtain systems with the desired properties. One possible strategy is to lock the molecules in a hydrogen bonded network, taking advantage of the chemical affinity between their functional groups. This approach mimics the organic 3D crystal growth mechanisms, based on the formation of supramolecular synthons [39]. In this context, several carboxylic molecules have been shown to assemble on surfaces in highly ordered architectures based on the formation of carboxylic homo-synthons [40, 41, 191–193], the molecular auto-recognition being favored by the intrinsic hydrogen donor (O–H) - acceptor (C=O) nature of the –COOH groups. In the synthesis of 3D crystals, the carboxylic group has been successfully exploited also in the formation of hetero-synthons, with the growth of organic co-crystals based on the hydrogen bond with the amines of a second molecular species [194–197].

In the previous three chapters, we have described the adsorption of three different molecules on the Au(111) surface. In particular, we studied amino-functionalized molecules on Au(111) (NMA and TAPP), and showed that the delicate interplay between the amino-amino and amino-substrate interaction governs the self-assembly of these molecules and the geometrical conformation of each molecule. In this chapter, as a further step, we exploit our knowledge on amino-functionalized molecules on Au(111) to build a novel supramolecular assembly based on the amino-carboxylic (A-C) interaction.

In surface science, the A-C affinity has been extensively exploited in the 2D homo-molecular self-assembly of amino-acids. It drives the formation of very long range ordered molecular chains with the molecules in their zwitterionic state on poorly reactive surfaces like Au(110) [198, 199], Au(111) [200], Ag(111) [34, 201], whereas it is inhibited by the stronger carboxylic-substrate interaction on more reactive surfaces like Cu(110) [142, 202], Cu(111) [201], and Cu(100) [203], where deprotonation of the carboxylic group occurs. Conversely, 2D hetero-organic assemblies based on the A-C interaction have been poorly explored. Recently, Cossaro and coworkers have shown that the chemical affinity between the two functional groups can drive the anchoring of a carboxylic molecule on top of an amino-terminated Self Assembled Monolayer, obtaining a vertically stacked hetero-organic structure [204]. On the other hand, so far we are not aware of examples of in-plane hetero-molecular coupling based on the interaction between these two groups.

Here we present a method for steering the assembly of a carboxylic molecule on surface. Our approach consists in modifying the metal substrate before the adsorption of the carboxylic molecules by depositing a second species of molecules, characterized by an amino-termination and a high surface mobility. In this way, we introduce a competitor to the well-known self-recognition of the carboxylic species, which modifies the molecular bonding scheme of the film. A similar approach has been reported in ref. [205, 206], where the amino-groups of melamine interact with the carbonyl oxygens of perylene derivatives forming a supramolecular template. The description of the morphology and the chemistry of the intermolecular bonding scheme paves the way to further investigations on the A-C interaction on surfaces and provides a novel method for steering the assembly of carboxylic molecules on surfaces.

This work, where I contributed with most of the STM experiments, has been published as Feng *et al.* in *Chemical Communications* [43].

6.1 Terephthalic acid (TPA)

To fulfil our high-mobility requirement we adopted the previously studied NMA molecule (see Chapter 4) to treat the Au(111) surface before the deposition of the carboxylic species. For the latter, we have chosen to employ the terephthalic acid (TPA) (figure 6.1a), whose assembly on the bare Au(111) surface represents a simple, prototypical system and has already been characterized by means of STM [40] and X-ray spectroscopies [207]. As usual, the preparation of the samples and the measurements have been performed under UHV. NMA was deposited on Au(111) as described in Chapter 4. TPA was evaporated in UHV from a standard Knudsen cell at a temperature of 390 K for few seconds (typically 10 s) on the sample at room temperature.

The TPA molecule on Au(111) assembles in a very compact 2D structure, formed by molecular chains placed side by side (fig. 6.1b), whose building block is represented by two head-to-tail aligned TPA molecules. This arrangement is driven by

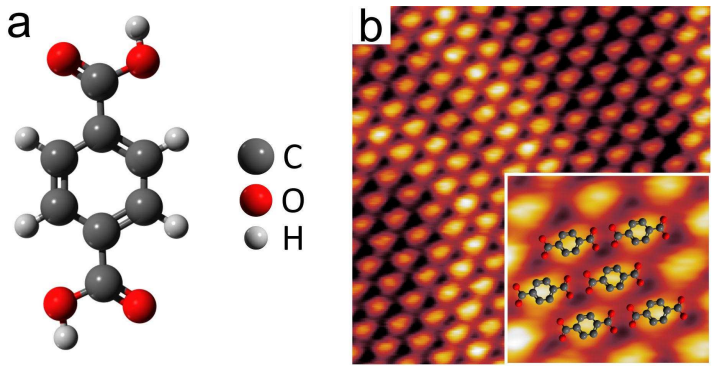

Figure 6.1: (a) Terephthalic acid and (b) it self-assembly on Au(111) with the inset showing a superimposed model on a zoomed image. STM image parameters: (b) V_s = +100 mV, I_t = 0.5 nA, 10.0 × 10.0 nm^2.

the hydrogen bond between the carboxylic groups, as revealed by XPS spectra. In particular, O 1s spectra (see figure 6.3b, top spectrum) showed that the two non-equivalent species of oxygen atoms of the molecule are indeed involved in a donor-acceptor hydrogen bond [207].

6.2 NMA-TPA competitive amino-carboxylic bond

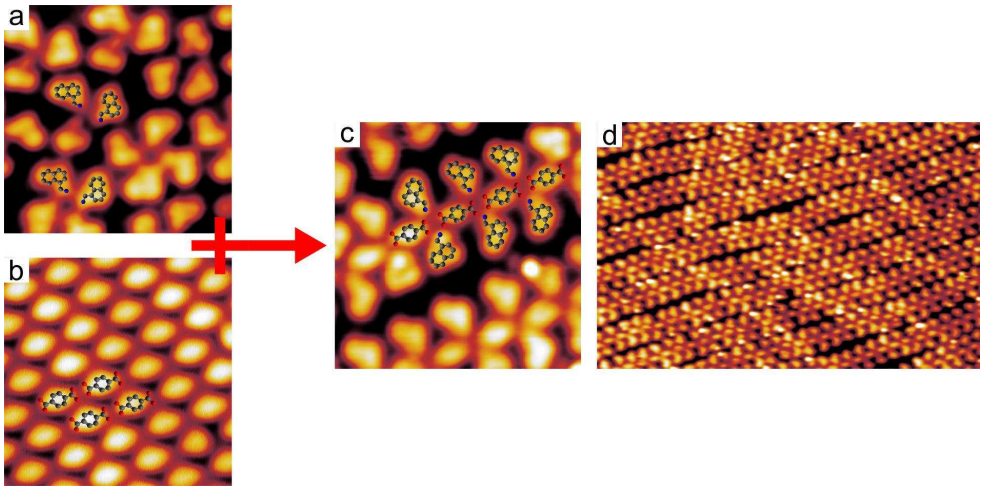

Figure 6.2: (a) The NMA and (b) TPA self-assemblies are mixed together (c) to form hetero-organic nanowires whose central backbone of TPA is decorated by lateral NMA molecules. (d) A wide STM image shows that, if dosed in 2 : 1 NMA/TPA ratio, NMA and TPA mix completely without phase separation. STM images parameters: (a) V_s = +100 mV, I_t = 50 pA, 4.6 × 4.6 nm^2; (b) V_s = +50 mV, I_t = 100 pA, 4.6 × 4.6 nm^2; (c) V_s = +200 mV, I_t = 20 pA, 5.0 × 5.0 nm^2; (d) V_s = +200 mV, I_t = 10 pA, 29.4 × 18.9 nm^2.

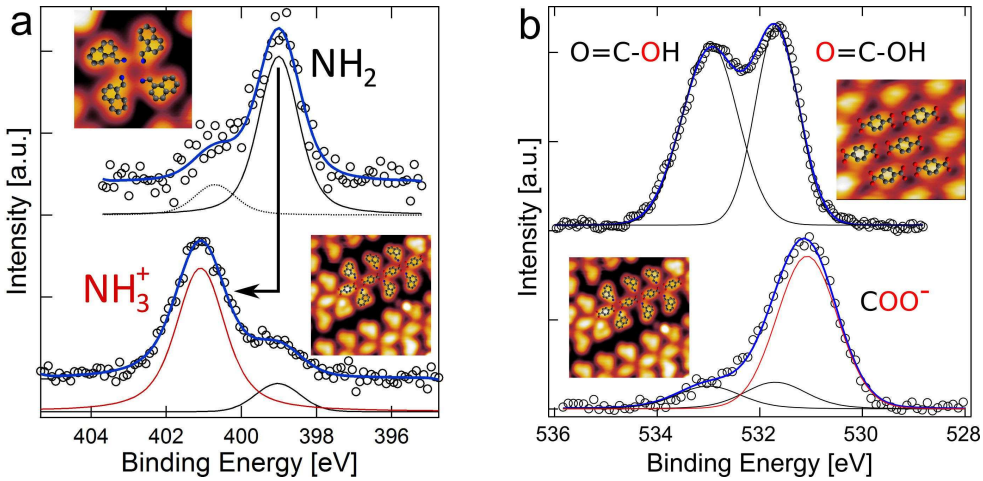

Figure 6.3: (a) N 1s XPS spectra show the chemical conversion of the amino groups of NMA from the neutral (top) to ionic state (bottom) when interacting with TPA. (b) Simultaneously, O 1s XPS spectra show the chemical conversion of the carboxylic groups of TPA from the homo-monolayer (top) to the mixed hetero-phase (bottom).

As anticipated in the introduction, to build the supramolecular assembly, we first modified the Au(111) by depositing NMA (amino-functionalized) with coverage below one monolayer, and then evaporated TPA (carboxylic-functionalized) onto the sample, thus introducing a competitor (NMA) to self-recognition of the carboxylic TPA molecules.

Upon the deposition of TPA on the NMA covered Au(111) sample, long hair-like structures are found on the surface, as shown in STM images in figure 6.2c, d. The N 1s XPS spectrum in figure 6.3a shows that the amino groups of the NMA undergo a chemical conversion, with the N 1s binding energy going from the neutral state at 399.0 eV (only NMA, fig. 6.3a top spectrum) to 401.1 eV (NMA-TPA, fig. 6.3a bottom spectrum), a value compatible with the ionic NH_3^+ chemical state [208]. A residue of neutral component is still found at 399.0 eV, due likely to residual NMA molecules non mixed with TPA. At the same time, the oxygen atoms of TPA undergo a chemical conversion as well. Figure 6.3b shows the O 1s XPS spectra of TPA/Au(111) (top spectrum) and of NMA-TPA mixed phase (bottom spectrum). The first spectrum exhibits two peaks associated to the two non-equivalent species of oxygen atoms of the molecule involved in a donor-acceptor hydrogen bond in its self-assembly, while the second exhibits only one main peak suggesting that the oxygen atoms are all equivalent and the carboxylic groups are in their anionic state COO^- [204]. Therefore, both the STM imaging and XPS show that the nature of the TPA intermolecular hydrogen bond has been deeply modified by the presence of the NMA molecule.

In the STM close-up of figure 6.2c, the details of the hair-like structure can be distinguished and the different molecules in the structure can be easily recognized, as suggested by the superimposed ball and stick model. Indeed, although NMA

and TPA sizes are similar, in the STM images they can be easily identified from their shapes: NMA has an irregular triangle shape, while TPA has a rhombus-like shape. It can be seen that the TPA molecules are aligned in rows similar to the ones observed when TPA is adsorbed individually on the bare Au surface; here, however, two NMA molecules participate in each TPA intermolecular bond in a novel bonding scheme.

6.3 NMA-TPA wires: multi stranded structures

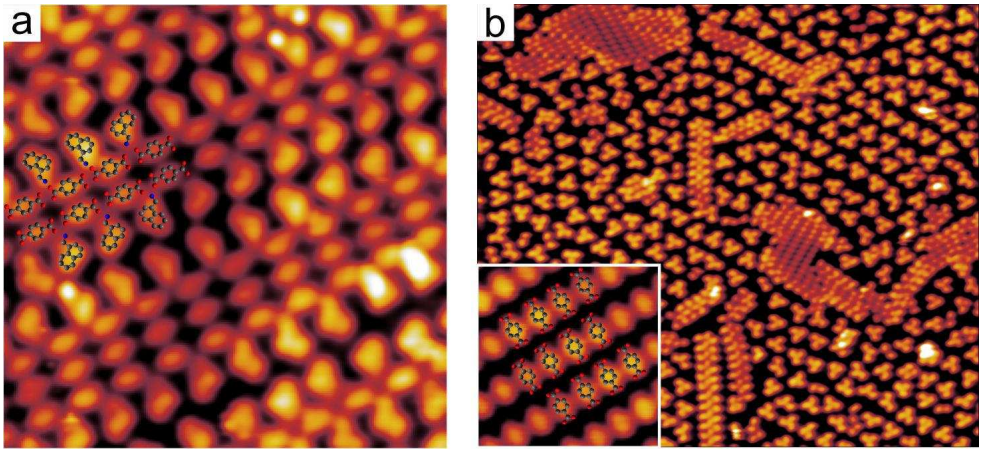

Figure 6.4: The NMA-TPA assembly depends on the NMA/TPA concentration. (a) An excess of TPA molecules promotes the assembly of multi-stranded hair structures. (b) With a low NMA coverage, the formation of 2D islands of TPA is observed. For both (a) and (b), the interaction with the NMA of the outer TPA molecules of the architectures also affects the pairing of the inner TPA rows. Image parameters: (a) $V_s = +200$ mV, $I_t = 20$ pA, 9.3×9.3 nm^2. (b) $V_s = +200$ mV, $I_t = 10$ pA, 50.0×44.0 nm^2.

We also verified that the sample temperature during deposition plays an important role: if TPA is deposited at lower sample temperatures ($T_s < 270$ K) no ordered structures are observed and STM imaging is very difficult probably due to the presence of second layer molecules. We hypothesize that the mobility of the molecules in this case is too low to drive the formation of the hair-phase bonding scheme. More interestingly, both TPA deposition at higher temperature ($T_s > 330$ K) or an annealing of the hair phase to the same temperature promote the formation of a hair-phase with double- or multi-TPA central rows, as shown in figure 6.4a. In fact, a minority of TPA molecules assembled in 2D structures can be found also on a surface with a highly ordered hair-phase. It can be argued that, since a $2:1$ ratio between the coverage of NMA and TPA is required for the formation of the hair-phase, the formation of 2D TPA assemblies occurs when this ratio decreases towards excess TPA. Notably, the TPA assembly in the double- and triple-stranded hair reported in figure 6.4a is different from the one found on bare Au(111). The TPA rows

join by aligning the phenyl groups of the molecules instead of building the usual honeycomb structure, indicating that the NMA-TPA interaction in the outer row of the strands modifies the pairing of the inner row. Starting with even lower NMA coverage, larger 2D islands of TPA were detected, as shown in figure 6.4b. In this case TPA was deposited at T_s = 300 K on a low coverage NMA/A(111) sample. As for the hair-phase with multi-TPA central rows, the TPA assembly in the islands is different from the one found on bare Au(111), the latter being more compact (see fig. 6.1b and 6.2b compared to fig. 6.4).

6.4 Conclusions

In conclusion, we have shown how the assembly of carboxylic molecules can be steered by treating the surface with a small amino-terminated molecule, leading to the formation of well-defined hetero-organic architectures. The A-C chemical affinity introduces a competition in the intermolecular hydrogen bonding and determines peculiar supra-molecular assemblies. The method we developed represents a valuable opportunity to explore alternative assembly morphologies of carboxylic-terminated molecules and yields a novel A-C motif of potential interest in the synthesis of co-crystals based on hetero-synthons. Furthermore, the heteromolecular architecture we characterized represents an ideal prototypical system for further investigations on the A-C interaction at surfaces.

Chapter 7

A chemical guest-host supramolecular assembly driven by the A-C recognition

In the previous Chapter we showed that the competitive A-C hydrogen bond can be exploited to build a supramolecular hetero-organic assembly of two small prototypical molecules on Au(111). In this Chapter, as a further step, we want to exploit this bond to build a novel guest-host supramolecular assembly based on this chemical recognition.

Organic templates are successfully synthesized on surfaces as both non-covalent and covalent (COFs) organic frameworks and as metal organic frameworks (MOFs) [36, 190, 209–213]. Guest-host approach on surfaces has been successfully applied to grow 2D arrays of fullerenes [205, 214, 215], coronene [216], small biomolecules [215], clusters of alkenthiols [217]. The adsorption of the guest molecules is driven by their shape matching with the template pores, which in fact limits the efficiency of the method in terms of the guest recognition. Moreover, little is known about how the guest-host interaction affects the properties of the guest molecules. In 3D architectures, the interaction between molecule and pores, based on non-covalent bonds, stabilizes the system and, as it was shown for MOFs, affects its chemical properties [218].

The chemistry of the 2D systems has not been investigated as far as we know. It has been shown that the guest-host interaction can be tailored by modifying the molecular building blocks of the template, obtaining a functionalization of the nanopores [219]. Likely, being the guest molecules interacting both with the pores and with the substrate, their chemical properties could be remarkably affected by the hosting process. Guest-host recognition and interaction do not represent an issue in the anchoring of molecules on surfaces, if the control of the morphology of the system at the nanoscale is not required. In this case, in fact, the surface is first functionalized with a properly terminated Self Assembled Monolayer (SAM) and then the molecules are deposited on top, the assembly process being driven by the

chemical affinity between the SAM and the molecule termination. The method is successfully employed both in solution, where selective covalent bonding between SAM and molecule is obtained through a click-chemistry approach [220–222] and under UHV, where the recognition process is based on hydrogen bonds [204, 207]. In both cases, the distribution of the anchoring points on the surface is ruled by the morphology of SAM, usually formed by alkanethiols derivatives and exhibiting intermolecular distances of few angstroms, thus preventing a controlled distribution at the nanoscale of the guest species. To overcome this limitation, a modulation of the chemical properties of the hosting SAM can be obtained by means of AFM-based patterning techniques [223–226]. The spatial resolution of the patterning of a template is however limited to tens of nanometers by the mechanical nature of method.

We report here a novel approach to the molecular anchoring at surfaces. Our guest-host strategy relies on the chemical affinity the carboxylic functional group we showed (Chapter 6) to exhibit towards primary amines on Au(111) [43]. Here we show how, with the same recognition mechanism, a regular 2D distribution of carboxylic groups on a surface can act as a template for the growth of amino-terminated molecules, the entire procedure being obtained under UHV conditions. No shape matching is required for the guest-host coupling, which is entirely based on the chemical affinity between two functional groups.

This work, where I contributed with most of the STM experiments, is in preparation for submission to a journal.

7.1 The carboxylic-functionalized host molecule: CTPP

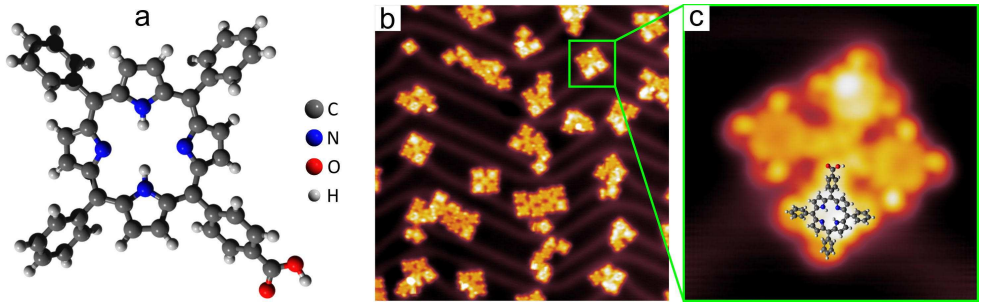

Figure 7.1: (a) 5-(4-carboxyphenyl)-10,15,20-(triphenyl)porphyrin (CTPP). (b) STM image of a low coverage of CTPP on Au(111), where CTPPs assemble in complexes of (c) four molecules via their carboxylic terminations. We point out that in panel (c) the carboxyphenyl terminations involved in the hydrogen bond can be easily identified because of their flatter appearance with respect to the phenyls. Image parameters: (b) $V_s = -0.5$ V, $I_t = 0.2$ nA, 40×40 nm^2; (c) $V_s = -0.5$ V, $I_t = 1.0$ nA, 6.0×6.0 nm^2.

As anticipated in the introduction, we want to employ a regular 2D self-assembly

of carboxylic molecules on a surface as a template for the growth of amino-terminated molecules. For this purpose, our 2D template is constituted by a self-assembled monolayer of a carboxylic-terminated (−COOH) phenyl porphyrin, CTPP (fig. 7.1a), grown on the Au(111) surface. CTPP molecules were evaporated from a Knudsen cell at a temperature of 520 K and deposited on Au(111) at room temperature. A sketch of the molecule is reported in figure 7.1a, together with STM images (fig. 7.1b, c) of a low coverage sample, showing that CTPPs assemble in complexes of four molecules via their carboxylic terminations in a cross-like structure. We point out that, while the phenyls of tetraphenylporphyrins on metal surfaces are generally tilted with respect to the surface plane [154, 167–169], the carboxyphenyl terminations here, in order to establish the hydrogen bond, appear flatter than the other phenyls, and can be thus easily recognized, being their phenyl ring resolved by STM (fig. 7.1c).

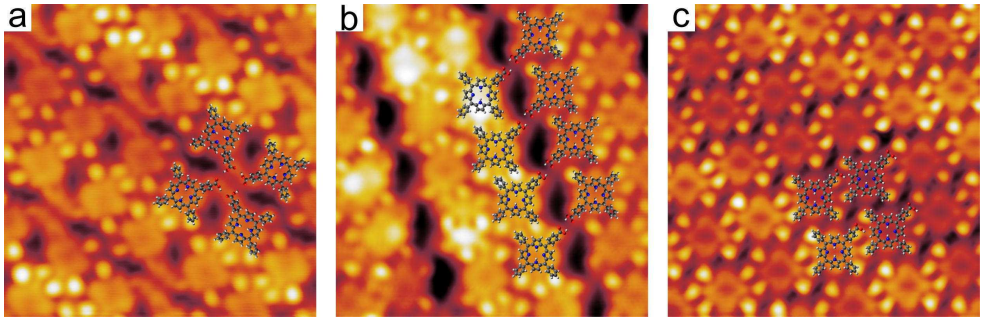

Figure 7.2: Three different phases of the self-assembly of CTPP on Au(111). (a) Phase A where four molecules bind via their carboxylic terminations like the complexes found at low coverage. (b) Phase B with paired CTPP bonded via their COOH terminations. (c) The most compact phase C, where no carboxylic-carboxylic bond is established. CTPP models are superimposed on the STM images to ease their identification. Notice that in (a) and (b) the carboxyphenyl terminations involved in the hydrogen bonds can be easily identified because they appear flatter than the phenyls. Image parameters: (a) $V_s = -0.5$ V, $I_t = 0.5$ nA, 8.0×8.0 nm^2; (b) $V_s = -0.5$ V, $I_t = 1.0$ nA, 8.0×8.0 nm^2; (c) $V_s = -0.5$ V, $I_t = 2.0$ nA, 8.0×8.0 nm^2.

As we mentioned in Chapter 6, the carboxylic self-recognition is known to play a determinant role in the assembly process of molecules on surfaces and is widely exploited for the formation of 2D hydrogen bond architectures [40, 41, 210, 216, 227]. Also here, the pairing of adjacent CTPP molecules is driven by the chemical affinity between their COOH groups. At high coverage, the molecules assemble in three different phases, as showed in figure 7.2, two of which characterized by the presence of carboxylic networks involving four (panel a, called phase A) or two molecules (panel b, called phase B), which resemble the ones observed for other carboxylic terminated porphyrines [41, 228]. In the compact phase C in figure 7.2c the carboxylic terminations are not involved in any auto-recognition process and the self-assembly is similar to the SAM of non-functionalized tetraphenylporphyrins on (111) metal surfaces [61].

The three phases coexist on the surface and their relative population depends on the SAM growth conditions: for high deposition rates (> 0.1 ML/min) the compact phase in panel c is prevalent, while for lower deposition rates the carboxylic-carboxylic bonded phases A and B are dominant, with the phase C almost disappeared. This is likely a dynamical process where a slow deposition rate preserves the carboxylic-bonded complexes during the SAM formation.

The CTPP SAM phases A and B are here employed as a carboxylic-functionalized 2D template to host smaller amino-terminated molecules. The carboxylic groups of the system, however, are here involved in the recognition process between adjacent CTTP molecules, which could inhibit the preferential adsorption of amines under an amino-carboxylic anchoring scheme. We point out that here, in analogy with the low coverage CTPP complexes, the carboxyphenyl terminations in figure 7.2a, b, being involved in the hydrogen bond, appear flatter than the other phenyls and can be thus easily identified. Therefore, to test the chemical properties of the CTTP template, we chose two different small amino-terminated molecules as hosts.

7.2 The amino-functionalized guest molecules: AMC and NMA

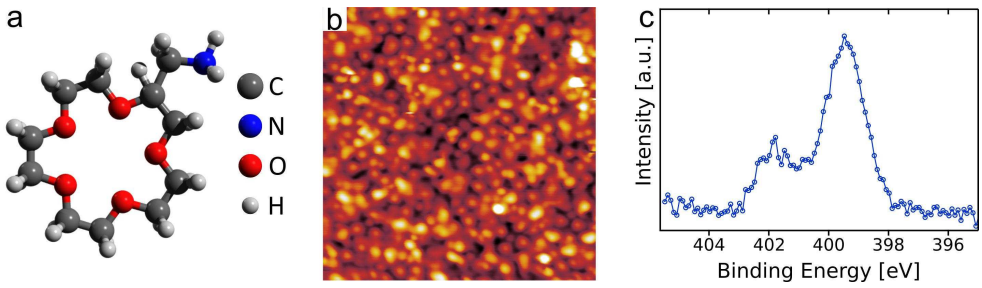

Figure 7.3: (a) 2-Aminomethyl-15-crown-5 (AMC). (b) STM image of the disordered monolayer of AMC on Au(111). (c) N 1s XPS spectrum of the AMC monolayer on Au(111) where the presence of many peaks suggests a not well defined chemistry. Image parameters: (b) $V_s = -0.2$ V, $I_t = 20$ pA, 15×15 nm^2.

The first molecule we chose is 2-Aminomethyl-15-crown-5 (AMC), which is basically a cyclic pentamer of ethylene oxide (called crown ether) with an aminomethyl termination (fig. 7.3a). AMC (Sigma Aldrich, 95%) was evaporated from a Pyrex vial, connected to the experimental chamber through an all-metal valve. Exposure of the Au(111) sample held at room temperature to the molecule at its vapour pressure ($\sim 5 \times 10^{-8}$ mbar) for 10 minutes yielded a saturation coverage.

Crown molecules invest a relevant importance in coordination chemistry, basically because of their affinity for metal ions, which allows for obtaining metal-organic complexes as well as ion sensors [229–231]. However, to our knowledge, no examples of their employment on supramolecular assembly on surfaces are found.

The reason can be attributed to the poor self-assembly properties they exhibit when deposited on metal surfaces. Figure 7.3b reports the STM image of a monolayer of AMC on the Au(111) surface. No ordered structures are observed.

An XPS study (fig. 7.3c) of the system shows that the molecules are involved in a quite complex chemistry on the surface, revealed by the presence of multiple components of the N 1s signal given by their amino-termination. The chemistry of crown molecules is determined by the electron lone pair of oxygen atoms, which give the reactivity to the molecules. On the surface, this reactivity possibly promotes the formation of molecular clusters and prevents an ordered distribution of the molecules.

As a second molecule to host into the CTPP template, we chose to employ NMA, whose self-assembly on Au(111) has been already studied in Chapter 4 and NMA-TPA supramolecular assembly studied in Chapter 6. We point out that both AMC and NMA are aminomethyl-functionalized, not simply amino-functionalized, because the aminomethyl termination gives a higher geometrical degrees of freedom to the NH_2 to interact with the carboxylic terminations.

7.3 AMC intercalation into the CTPP template

Figure 7.4 shows the AMC-CTPP supramolecular self-assembly after depositing AMC onto the 2D template of CTPP. Two coexisting phases are found on the surface: one with AMC/CTPP molecules ratio of 1 : 1, the other with AMC/CTPP of 1 : 2. In both phases, AMC is regularly intercalated into the CTPP template, as one can see in figure 7.4; in the STM images, CTPPs have the same appearance as in figure 7.2, while AMCs look like irregular bright spots because of their several geometrical degrees of freedom.

These two phases resemble somehow the two ones of the CTPP template. In particular, the AMC/CTPP 1 : 2 phase in figure 7.4b looks similar to the CTPP SAM phase B (fig. 7.2b) with the AMC molecules filling the empty holes left by the CTPPs. Instead, the 1 : 1 phase in figure 7.4a, where CTPP molecules are in a two by two assembly, does not resemble clearly the CTPP SAM phase A (fig. 7.2a), although we can speculate that the competitive amino-carboxylic bond modifies the cross-like four carboxylic-terminations assembly to accommodate the AMC molecules. Indeed, we have already showed in Chapter 6 that the presence of an aminomethyl-molecule, NMA, modifies the TPA-TPA carboxylic-carboxylic self-assembled structure, even if NMAs only decorate TPA islands [43]. We stress that, although these two phases resemble the two CTPP SAM phases, we cannot infer certainly that they come directly from the CTPP SAM since we have not performed any dynamical characterization of the intercalation process.

Now we know that AMC intercalate regularly into the carboxylic CTPP template, but with only STM images we cannot infer what kind of interaction drives this intercalation. Therefore, as we did for NMA-TPA wires (section 6.2), we performed XPS measurements to obtain chemical information on our system. Figure

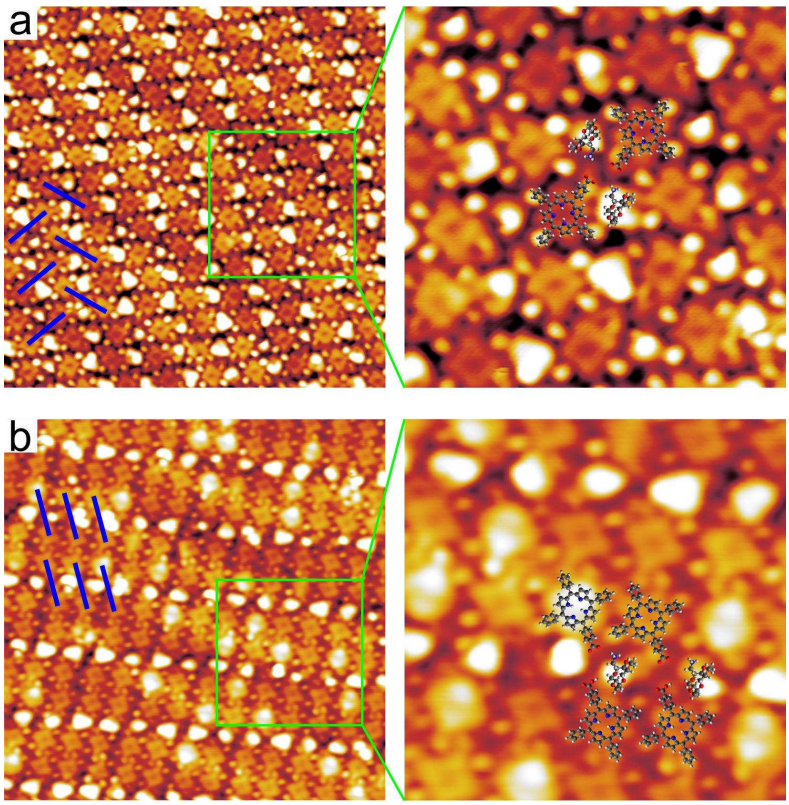

Figure 7.4: STM images of the two coexisting phases the AMC-CTPP self-assembly. (a) AMC/CTPP 1 : 1 phase and (b) AMC/CTPP 1 : 2 phase. The blue lines help to identify the periodicity of the supramolecular architectures. For each image, on the right there is a zoomed image with superimposed models of AMC and CTPP to help the reader to identify each molecule. Images parameters: (a) $V_s = -0.2$ V, $I_t = 2.0$ nA, 20×20 nm^2 (7.5×7.5 nm^2 zoomed); (b) $V_s = -0.1$ V, $I_t = 0.2$ nA, 20×20 nm^2 (7.5×7.5 nm^2 zoomed).

7.5a shows a N 1s XPS spectrum of the CTPP SAM, which exhibits two typical peaks associated to the iminic (397.2 eV) and pyrrolic (399.3 eV) internal nitrogen atoms of the porphyrins. Upon deposition of AMC, the N 1s spectrum exhibits a new component at 401.3 eV (fig. 7.5b, yellow peak), a value compatible with the ionic NH_3^+ chemical state [43, 208], which is a fingerprint of the A-C hydrogen bond.

By comparing our STM images with the XPS N 1s spectra, we conclude that here the competitive A-C bond drives the intercalations of AMC molecules into the 2D network of CTPPs. Indeed, similarly to what we found for the NMA-TPA wires, here the AMC molecules "decorate" laterally the carboxyphenyl-carboxyphenyl bonded terminations of CTPPs in order to establish the hydrogen bond.

We stress that no shape matching is required here for the guest-host (AMC-CTPP) coupling, which is entirely based on the chemical affinity. As showed in figure 7.6, the unit cell of the AMC/CTPP 1 : 2 phase (right panel) is different from the CTPP phase B SAM unit cell (left panel), with the latter slightly smaller. The

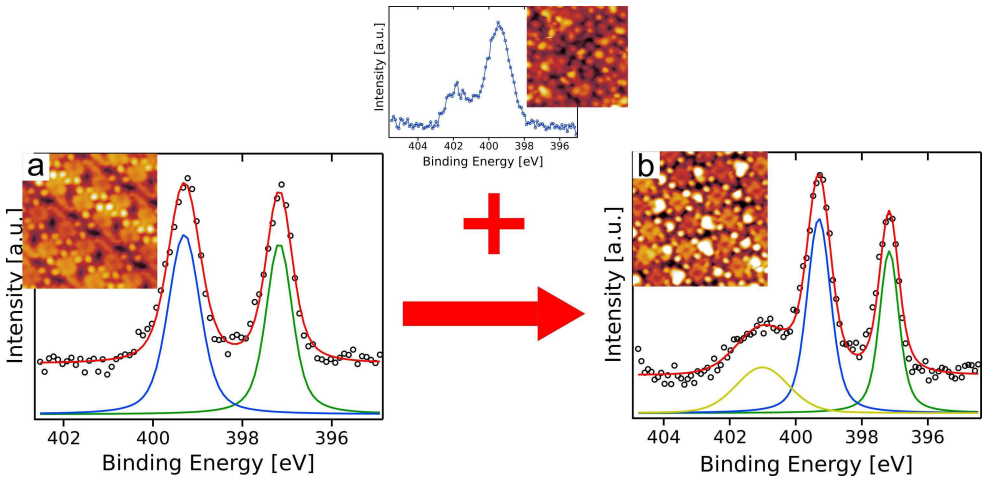

Figure 7.5: (a) N 1s XPS spectrum of the CTPP SAM exhibiting two typical peaks associated to the iminic (397.2 eV) and pyrrolic (399.3 eV) nitrogen atoms of the porphyrin. (b) After deposition of AMC onto the CTPP SAM, in the N 1s XPS spectrum appears a new peak (yellow) at 401.3 eV, which is associated to the $-NH_3^+$ of AMC in the competitive A-C hydrogen bond.

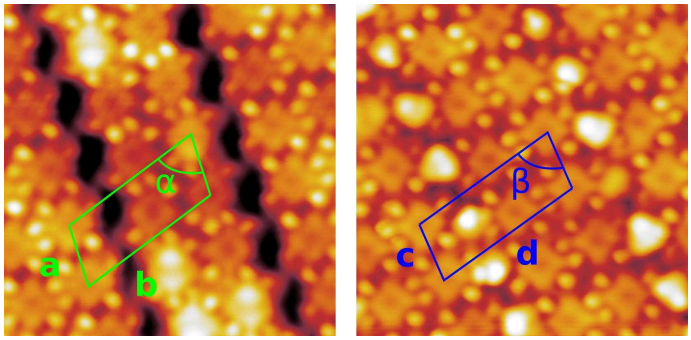

Figure 7.6: Comparison of a CTPP SAM phase B unit cell (left panel) with an AMC-CTPP SAM unit cell (right panel). Angles: $\alpha = 73°$, $\beta = 80°$. Lattice parameters: $a = 1.48$ nm, $b = 3.60$ nm, $c = 1.50$ nm, $d = 3.70$ nm.

chemical affinity is strong enough to modify the preexisting CTPP template in order to accommodate the AMC molecules. This is even more evident if we consider the AMC/CTPP 1 : 1 phase (fig. 7.4a) which is deeply different from any CTPP SAM phase (fig. 7.2).

Within this picture, the AMC intercalation is possible only if the starting CTPP template is not a full monolayer SAM, typically 0.9 ML. Indeed, if we employ a full monolayer of CTPP, the STM experiments (not showed) suggest that the AMC molecules cannot intercalate into the template since the CTPP molecules do not have enough space to displace themselves to accommondate the AMC molecules.

As last remark, we verified also that we could remove the intercalated crown

molecules by heating our sample: after annealing our sample to 470 K, the STM images show that almost all the crown molecules have desorbed, while the CTPP template is still perfectly intact, ready to host new molecules. Therefore, with our method the host template can be easily reset.

7.4 NMA intercalation into the CTPP template

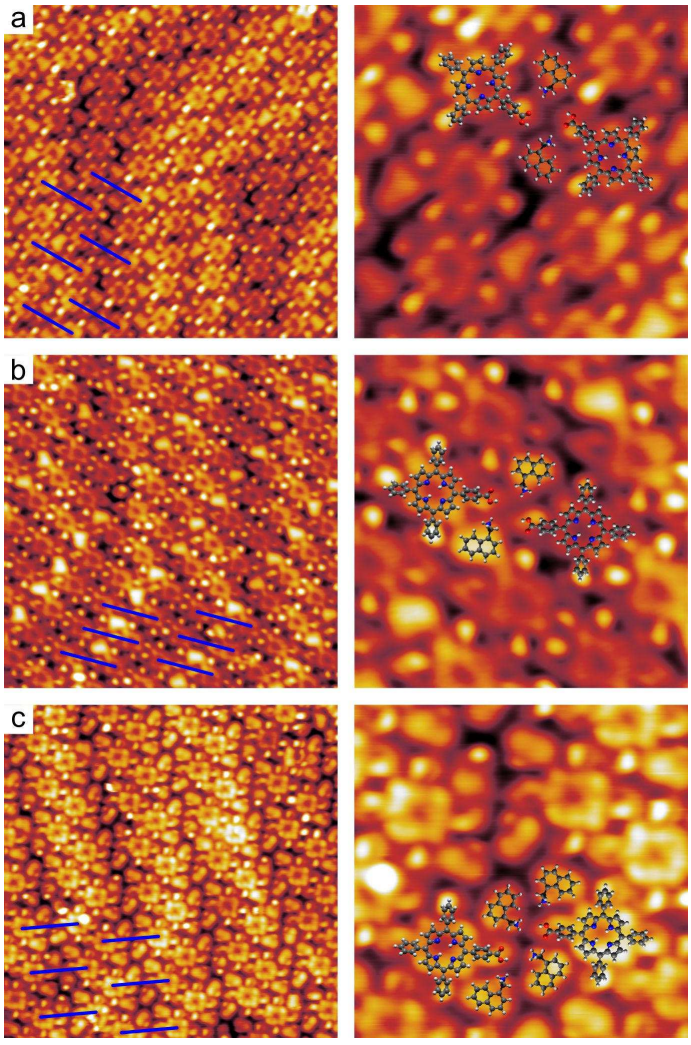

Figure 7.7: STM images of the different coexisting phases the NMA-CTPP self-assembly. The blue lines on the images help to identify the periodicity of the supramolecular architecture. For each image, on the right there is a zoomed image with superimposed models of NMA and CTPP to help the reader to identify each molecule. Images parameters: (a) $V_s = -0.1$ V, $I_t = 0.2$ nA; (b) $V_s = -0.1$ V, $I_t = 0.3$ nA, 15×15 nm^2; (c) $V_s = -0.1$ V, $I_t = 70$ pA. All images: 15×15 nm^2 (5.0×5.0 nm^2 zoomed).

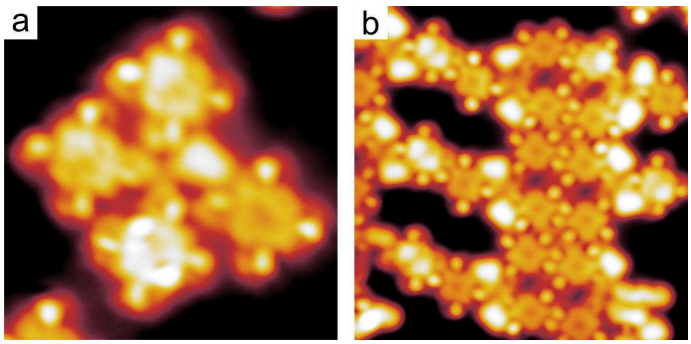

Figure 7.8: (a) A cross-like four CTPP complex where one CTPP is displaced by a NMA molecule to establish the A-C bond. (b) A wider image of NMA deposited on a low coverage (~ 0.5 ML) CTPP SAM. Images parameters: (a) $V_s = -0.1$ V, $I_t = 0.3$ nA, 5.0×5.0 nm^2; (b) $V_s = -0.1$ V, $I_t = 0.5$ nA, 10×10 nm^2.

The deposition of NMA molecules onto the CTPP template yields an NMA-CTPP supramolecular assembly similar to the AMC-CTPP one. Figure 7.7 shows three different coexisting phases of the NMA-CTPP assembly. The first two phases are NMA/CTPP 1 : 1 and 1 : 2 phases, in figure 7.7a and b, respectively, and they are equivalent the two AMC/CTPP phases (fig. 7.4a and b, respectively).

Interestingly enough, there is a further NMA/CTPP 2 : 1 phase (fig. 7.7c), which does not correspond to any AMC/CTPP phase. In this phase there are 4 NMA molecules for each couple of CTPP-CTPP, and we hypothesize that all the 4 NMAs have their $-NH_2$ terminations interacting competitively with the COOH-COOH bond of CTPPs (fig. 7.7c, zoomed image). The presence of this phase, not found for AMC/CTPP, is likely due to the molecular size of NMA which is considerably smaller than AMC, and therefore is able to establish a 4 NMA to 2 CTPP bonding scheme. As mentioned above, this last bonding scheme requires CTPP displacement to leave enough space to the NMA molecules to intercalate, and thus the occurrence of NMA/CTPP 2 : 1 phase depends also on the initial CTPP template coverage.

As we did with the crown molecules, we verified that our template can be renewed by removing the guest molecules: after annealing the sample to 420 K, all the NMA molecules have desorbed, leaving the CTPP template perfectly intact and ready to host new molecules.

As last remark, we studied the adsorption of NMA onto a low coverage (~ 0.5 ML) CTPP/Au(111) sample, as showed in figure 7.8. The high resolution image in panel a suggests how the NMA molecule, thanks to the A-C affinity, can displace one CTPP from the cross-like CTPP complex. From this image we can hypothesize that, as mentioned above, the CTPP SAM in phase A can be turned into the NMA/CTPP 1 : 1 phase in figure 7.7a. Indeed, we can infer that, in a more compact CTPP phase A, the adsorption of two NMA molecules can displace two CTPP from the cross-like structure making these two CTPP rotate and form COOH–COOH bond with other neighboring CTPP molecules. The wider image in panel b shows how to displace-

ment mechanism works at a larger scale. These images give us a hint about the dynamics of the NMA-CTPP (and similarly AMC-CTPP) hetero-assembly and help to understand how the CTPP phase A (fig. 7.2a) can transformed into NMA/CTPP (AMC/CTPP) 1 : 1 phase figure 7.7a (fig. 7.4a). These findings might suggest that in the CTPP-NMA SAM the role of the guest and the host can be swapped, since at low coverage we can obtain TCPP-NMA self-assembled islands also by depositing NMA before CTPP. However, we point out that the CTPP template dictates the geometry of the hetero-organic architecture and a full monolayer of CTPP-NMA can obtained only by first building the CTPP SAM, which therefore can be reasonably considered the host molecule.

7.5 Conclusions

In conclusion, we have shown that the competitive A-C recognition can be exploited to build a novel guest-host strategy based on the chemical affinity rather than shape matching between the host and guest molecules. In particular, we showed that two small aminomethyl-functionalized guest molecules, AMC and NMA, whose self-assemblies on Au(111) do not show any long-range ordered structure, can be regularly deposited and intercalated into the ordered 2D template of CTPP (carboxylic-host), driven by the A-C chemical affinity. No shape matching is required for the guest-host coupling, which is entirely based on the chemical affinity between two functional groups, which is also strong enough to modify the preexisting template of CTPP to accommodate the guest molecules. The A-C recognition is a powerful tool to build novel supramolecular motifs, and the method we developed here represents a valuable example of how this bond can be exploited.

Chapter 8

Conclusions and outlook

In this thesis work several homo- and hetero-organic supramolecular assemblies have been investigated on Au(111) by means of STM, XPS, and NEXAFS in UHV conditions. In Part I we described the role of the gold substrate in the formation of molecular architectures by presenting three different studies where we explain the interplay between molecule-molecule and molecule-substrate interactions driving the assembly processes.

As a first case, we studied the adsorption on Au(111) of a commonly used solvent, DMSO. Our combined STM imaging and DFT simulations reveal that DMSO forms complexes of 3 or 4 molecules, unexpectedly trapping one or two positively charged gold adatoms, natively available on Au(111), to which DMSO coordinates by its oxygen atom via a bond of ionic nature. Although not visible in the STM images, such adatoms are crucial for the stability of the observed DMSO complexes. With this work we have showed that the interaction between a polar solvent (DMSO) and a gold substrate cannot be neglected, since peculiar solvent-gold interactions can be present even at room temperature. The nanoscale properties of the gold-solvent interface are of great relevance, for example in electrochemistry where the solvent-electrode interaction is relevant, and our findings can contribute to the understanding of these properties at the atomic scale.

We also investigated the behavior of two amino-functionalized molecules in order to understand the behavior of the NH_2 termination on Au(111). First, we studied NMA whose aminomethyl-termination drives the formation of complexes of 3 or 4 molecules, which we showed to be results of the interplay between the amino-amino and amino-substrate interactions. In this case, the Au(111) herringbone reconstruction plays a crucial role, where the relative population of these complexes is dictated by the *hcp* and *fcc* regions of the substrate. Second, we studied TAPP whose aminophenyl-terminations drive the formation of molecular wires via hydrogen bonds. In such wires, each TAPP is found to be alternately a proton donor or acceptor, with the latter trapping native gold adatoms at its center. Moreover, by means of STM manipulation, the donor TAPPs can be switched in two ways:

tautomerization or conformation switch, both switches being binary. We showed that both the TAPP wire geometry and the symmetry properties of switching are governed by the aminophenyl-terminations.

After studying the behaviour of amino-functionalized molecules on Au(111), in Part II we employed these molecules, coupling them with carboxylic-functionalized molecules, to design novel 2D hetero-organic architectures based on the A-C bond. We started first by considering two small prototypical molecules, NMA (amino-) and TPA (carboxylic-), which we showed to form hetero-organic wires in a competitive A-C bonding scheme. Our work on NMA-TPA is the first study of an in-plane hetero-molecular coupling based on the A-C interaction, and represents a novel method for steering the assembly of a carboxylic molecule on a metal surface.

In the last chapter, we exploited the A-C competitive bond to develop a novel guest-host supramolecular strategy based on chemical recognition rather than shape matching between the guest and host molecules. By employing a SAM of CTPP as the (carboxylic-) host template, we could successfully intercalate two small guest aminomethyl-terminated molecules, AMC and NMA, into the host template. No shape matching is required for the guest-host coupling; actually, we found that the chemical affinity is strong enough to modify the preexisting CTPP template to accommodate the guest molecules, suggesting that our method is also very flexible. By developing this novel guest-host strategy we demonstrated that the A-C recognition is a powerful tool to build new supramolecular motifs.

Our studies on the solvent-gold and amino-gold interaction, and the A-C recognition based methods we developed represent a step forward in the understanding of the structural properties of molecular layers and molecular junctions at fundamental level. Undoubtedly, there are still many open questions and possible development plans for our studies. For example, we should deepen the understanding of the role of the native gold adatoms, which is not crucial in the NMA-TPA and CTPP guest-host SAM, as opposed to the cases of the DMSO complexes and TAPP wires. Another important point is the fact that the A-C bond we explored is a hydrogen bond while, in a potential application of these molecules, more stable, covalently bonded structures would be desired. The condensation reaction where an A-C interaction is converted into a covalent bond, called peptide bond, is a fundamental mechanism in living systems, where amino acids condensate to form proteins. As mentioned in Chapter 6, in surface science the 2D homo-molecular self-assembly of amino acids on metal surfaces have been extensively studied; however, none has been able to induce the condensation of amino acids on surface so far.

Actually, we have already explored some possible strategies to induce condensation in our A-C bonded hetero-structures, although without any satisfactory result up to now. For example, we attempted to condensate the hydrogen bonded structures by X-ray irradiation of our sample. We will further examine this method by changing the exposure time of the sample to X-ray, or by changing the wavelength

(photon energy) of irradiation up to the ultraviolet range. Another possible strategy is the deposition of an additional molecule that can catalyze the condensation reaction or, as an alternative, we will change the supporting substrate from Au(111) to another more reactive metal surface. In our future plans we consider to explore all these strategies step by step in order to obtain for the first time the A-C condensation on surface.

Acronyms

A-C	Amino-Carboxylic
AMC	2-aminomethyl-15-crown-5
CTPP	5-(4-carboxyphenyl)-10,15,20-(triphenyl)porphyrin
DMSO	dimethyl sulfoxide
DOS	Density of States
IETS	Inelastic Electron Tunneling Spectroscopy
LT-STM	Low Temperature Scanning Tunneling Microscope
LDOS	Local Density of States
LEED	Low Energy Electron Diffraction
LHe	Liquid Helium
LN_2	Liquid Nitrogen
NEXAFS	Near Edge X-ray Absorption Fine Structure
NMA	1-naphthylmethylamine
RT	Room Temperature
SAM	Self-Assembled Monolayer
STM	Scanning Tunneling Microscope
STS	Scanning Tunneling Spectroscopy
TAPP	5,10,15,20-tetra(4-aminophenyl)porphyrin
TPA	terephthalic acid
UHV	Ultra High Vacuum
XPS	X-ray Photoelectron Spectroscopy

Acknowledgements

Finally, here we come to the most important part of this thesis. I must thank all the people for supporting and "sopporting" me during these years. First of all, I would like to thank my three phenomenal supervisors Carlo Dri, Albano Cossaro and Giovanni Comelli from whom I learned so much. I owe my gratitude to all my colleagues of our lab: Cristina Africh, Laerte Patera, Jeromy Zou, Alberto Rizzini, and the new entries Alessandro Sala and Mirko Panighel.

Thanks to all the colleagues who worked with me here in Trieste: Erik Vesselli, Manuel Corva, Enrico Monachino, Nicola Podda, Matteo Roiaz of the SFG group. Thanks to the ALOISA guys Albano, Alberto Verdini, Luca Floreano, Alberto Morgante, Dean Cevtko, Gregor Kladnik, Carla Castellarin, Giacomo Lovat, Marcos D. Rivera, Matus Stredansky, Roberto Costantini, and even Tommaso Fontanot, who would otherwise complain. Many thanks to my theoretician colleagues Simone Velari, Alessandro De Vita, Maria Peressi, and the group of Giovanna Fronzoni for their fantastic simulations. I want to thank also Giovanni Zamborlini, Matteo Jugovac and Vitaly Feyer for the intense work done together. Thanks also to prof. Leonhard Grill and his group in Graz for the fruitful (although unlucky) experience I had there for two months. Finally, I thank Amir Mazaheripour and Alon Gorodetsky.

I would like to thank also all the students who I supervised during these years: Irene, Giulia, Rossella, Roberto and Nicola. Then, I acknowledge my students of the "tutoraggio", with whom I had a wonderful teaching experience. I wish you all the best for the future!

I owe my gratitude to my family. Unable to thank everyone singly (also because I cannot remember their name…), here I mention my mum, dad and Angelo, the kingpin of Bar Sub. Giulia and Cristina (the best), instead, owe me their gratitude. I must also mention, because they asked me to, Luo and Ste. Last but not least, I thank Una for everything.

Special thanks go to my friends and imaginary colleagues Michele and Nicola, with whom one day I will start the "Megaditta". I thank Agnese and Enrico who, despite the long distance, always make me feel their presence and friendship, and Stefano who misses Trieste so much that he comes to visit me. Thanks also to Cabass and Marchiza, crazy guys. Special thanks to the astroguys of SISSA who are really too many, so cite them as Franca, Ricky *et al.* Thanks also to the PhDrinkers. Finally, I thank my imaginary friends who have been with me all my life.

Bibliography

1. Waldrop, M. M. The chips are down for Moore's law. *Nature* **530,** 144–147 (2016).
2. Jurow, M., Schuckman, A. E., Batteas, J. D. & Drain, C. M. Porphyrins as molecular electronic components of functional devices. *Coordination Chemistry Reviews* **254,** 2297–2310 (2010).
3. Everitt, D. L., Miller, W. J. W., Abbott, N. L. & Zhu, X. D. Evolution of a preferred orientation of polycrystalline grains in obliquely deposited gold films on an amorphous substrate. *Physical Review B* **62,** R4833–R4836 (2000).
4. Wang, Y., Teitel, S. & Dellago, C. Melting of icosahedral gold nanoclusters from molecular dynamics simulations. *The Journal of Chemical Physics* **122,** 214722 (2005).
5. Binnig, G., Rohrer, H., Gerber, C. & Weibel, E. Surface Studies by Scanning Tunneling Microscopy. *Physical Review Letters* **49,** 57–61 (1982).
6. R. P. Feynman. *There's plenty of room at the bottom* 1960.
7. *Wikimedia Commons*
8. Chen, C. J. *Introduction to Scanning Tunneling Microscopy Second Edition* (Oxford University Press, 2007).
9. J. Bardeen. Tunnelling from a Many Particle Point of View. *Physical Review Letters* **6,** 6–8 (1961).
10. D. M. Eigler and E. K. Schweizer. Positioning single atoms with a scanning tunnelling microscope. *Nature* **344,** 524–526 (1990).
11. Meyer, G. *et al.* Controlled Manipulation of Atoms and Small Molecules with a Low Temperature Scanning Tunneling Microscope. *Single Molecules* **1,** 79–86 (2000).
12. Moresco, F. *et al.* Conformational Changes of Single Molecules Induced by Scanning Tunneling Microscopy Manipulation: A Route to Molecular Switching. *Physical Review Letters* **86,** 672–675 (2001).
13. Stipe, B. *et al.* Single-Molecule Dissociation by Tunneling Electrons. *Physical Review Letters* **78,** 4410–4413 (1997).

14. Hla, S.-W., Bartels, L., Meyer, G. & Rieder, K.-H. Inducing All Steps of a Chemical Reaction with the Scanning Tunneling Microscope Tip: Towards Single Molecule Engineering. *Physical Review Letters* **85,** 2777–2780 (2000).

15. Feenstra, R. M. Scanning tunneling spectroscopy. *Surface Science* **299-300,** 965–979 (1994).

16. Hamers, R. Atomic-Resolution Surface Spectroscopy with the Scanning Tunneling Microscope. *Ann. Rev. Phys. Chem.* **40,** 531 (1989).

17. Feenstra, R. & Stroscio, J. Real-Space Determination of Surface Structure by Scanning Tunneling M icroscopy. *Physica Scripta* **55** (1987).

18. *Scanning Tunneling Microscopy I* (eds Güntherodt, H.-J. & Wiesendanger, R.) (Springer Berlin Heidelberg, Berlin, Heidelberg, 1992).

19. Komeda, T. Chemical identification and manipulation of molecules by vibrational excitation via inelastic tunneling process with scanning tunneling microscopy. *Progress in Surface Science* **78,** 41–85 (2005).

20. Dri, C. *Characterization and manipulation of single molecules and molecular complexes by Low Temperature Scanning Tunneling Microscopy* PhD thesis (Università degli Studi di Trieste, 2008).

21. G. Ertl and J. Küppers. *Low Energy and Surface Chemistry* (VHC Publisher, 1988).

22. Smart, R., Mcintyre, S., Bancroft, M. & Bello, I. *X-ray Photoelectron Spectroscopy*

23. Braraldi, A. *Fondamenti di fisca delle superfici* in (2012).

24. Doniach, S. & Sunjic, M. Many-eelctron singularity in X-ray photoemission and X-ray line spectra from metals. *Journal of Physics C* **285** (1970).

25. Mussa, O. *Development of High-pressure X-ray Photoelectron Spectroscopy (XPS) Unit* tech. rep. (Environmental Sciences, University of California, Berkeley).

26. Hofmann, A. *The physics of synchrotron radiation* (Cambridge University Press, 2004).

27. Hadjarab, F. & Erskine, J. L. Image properties of the hemispherical analyser applied to multichannel energy detection. *Journal of electron spectroscopy and related phenomena* **36,** 227–243 (1985).

28. Penner-Hahn, J. E. *X-ray Absorption Spectroscopy* tech. rep. (University of Michigan).

29. Paolucci, G. *XAFS (X-ray Absorption Fine Structure)* in (2011).

30. Bare, S. R. *XANES Measurements and Interpretation* in (2005), 1–51.

31. Stöhr, J. & Outka, D. A. Determination of molecular orientations on surfaces from the angular dependence of near-edge x-ray-absorption fine-structure spectra. *Physical Review B* **36,** 7891–7905 (1987).

32. *ALOISA*

33. *The ANCHOR project*

34. Barth, J. V. Molecular Architectonic on Metal Surfaces. *Annual Review of Physical Chemistry* **58,** 375–407 (2007).

35. De Feyter, S. & De Schryver, F. C. Two-dimensional supramolecular self-assembly probed by scanning tunneling microscopy. *Chemical Society Reviews* **32,** 139–150 (2003).

36. Bartels, L. Tailoring molecular layers at metal surfaces. *Nature Chemistry* **2,** 87–95 (2010).

37. Haq, S. *et al.* Versatile Bottom-Up Construction of Diverse Macromolecules on a Surface Observed by Scanning Tunneling Microscopy. *ACS Nano* **8,** 8856–8870 (2014).

38. Simard, M., Su, D. & Wuest, J. D. Use of hydrogen bonds to control molecular aggregation. Self-assembly of three-dimensional networks with large chambers. *Journal of the American Chemical Society* **113,** 4696–4698 (1991).

39. Desiraju, G. R. Supramolecular Synthons in Crystal Engineering—A New Organic Synthesis. *Angewandte Chemie International Edition in English* **34,** 2311–2327 (1995).

40. Clair, S. *et al.* STM Study of Terephthalic Acid Self-Assembly on Au(111): Hydrogen-Bonded Sheets on an Inhomogeneous Substrate. *The Journal of Physical Chemistry B* **108,** 14585–14590 (2004).

41. Yokoyama, T., Kamikado, T., Yokoyama, S. & Mashiko, S. Conformation selective assembly of carboxyphenyl substituted porphyrins on Au (111). *The Journal of Chemical Physics* **121,** 11993 (2004).

42. Otero, R. *et al.* Guanine Quartet Networks Stabilized by Cooperative Hydrogen Bonds. *Angewandte Chemie* **117,** 2310–2315 (2005).

43. Feng, Z. *et al.* A competitive amino-carboxylic hydrogen bond on a gold surface. *Chem. Commun.* **51,** 5739–5742 (2015).

44. Dmitriev, A., Spillmann, H., Lin, N., Barth, J. V. & Kern, K. Modular Assembly of Two-Dimensional Metal–Organic Coordination Networks at a Metal Surface. *Angewandte Chemie* **115,** 2774–2777 (2003).

45. Garah, M. E. *et al.* Molecular tectonics based nanopatterning of interfaces with 2D metal–organic frameworks (MOFs). *Chem. Commun.* **50,** 12250–12253 (2014).

46. Stepanow, S., Lin, N. & Barth, J. V. Modular assembly of low-dimensional coordination architectures on metal surfaces. *Journal of Physics: Condensed Matter* **20,** 184002 (2008).

47. Faraggi, M. N. *et al.* Bonding and Charge Transfer in Metal–Organic Coordination Networks on Au(111) with Strong Acceptor Molecules. *The Journal of Physical Chemistry C* **116,** 24558–24565 (2012).

48. Yang, Z. *et al.* Orbital Redistribution in Molecular Nanostructures Mediated by Metal–Organic Bonds. *ACS Nano* **8,** 10715–10722 (2014).

49. Freakley, S. J., He, Q., Kiely, C. J. & Hutchings, G. J. Gold Catalysis: A Reflection on Where We are Now. *Catalysis Letters* **145,** 71–79 (2015).

50. Laguna, A. *Modern Supramolecular Gold Chemistry* (ed Laguna, A.) 528 (Wiley-VCH Verlag GmbH & Co. KGaA, Weinheim, Germany, 2008).

51. Zhou, K. *et al.* A low content Au-based catalyst for hydrochlorination of C 2 H 2 and its industrial scale-up for future PVC processes. *Green Chem.* **17,** 356–364 (2015).

52. Dorsey, J. F. *et al.* Gold nanoparticles in radiation research: potential applications for imaging and radiosensitization. *Translational cancer research* **2,** 280–291 (2013).

53. Chen, M. S. The Structure of Catalytically Active Gold on Titania. *Science* **306,** 252–255 (2004).

54. Choudhary, T. & Goodman, D. Catalytically active gold: The role of cluster morphology. *Applied Catalysis A: General* **291,** 32–36 (2005).

55. Wittstock, A. & Bäumer, M. Catalysis by Unsupported Skeletal Gold Catalysts. *Accounts of Chemical Research* **47,** 731–739 (2014).

56. Harten, U., Lahee, A. M., Toennies, J. P., Woll, C. & Wöll, C. Observation of a Soliton Reconstruction of Au(111) by High-Resolution Helium-Atom Diffraction. *Physical Review Letters* **54,** 2619–2622 (1985).

57. Barth, J. V., Brune, H., Ertl, G. & Behm, R. J. Scanning tunneling microscopy observations on the reconstructed Au(111) surface: Atomic structure, long-range superstructure, rotational domains, and surface defects. *Physical Review B* **42,** 9307–9318 (1990).

58. Boscoboinik, J. A. *et al.* One-dimensional supramolecular surface structures: 1,4-diisocyanobenzene on Au(111) surfaces. *Physical Chemistry Chemical Physics* **12,** 11624 (2010).

59. Jewell, A. D., Tierney, H. L. & Sykes, E. C. H. Gently lifting gold's herringbone reconstruction: Trimethylphosphine on Au(111). *Physical Review B* **82,** 205401 (2010).

60. Jewell, A. D., Sykes, E. C. H. & Kyriakou, G. Molecular-scale surface chemistry of a common metal nanoparticle capping agent: Triphenylphosphine on Au(111). *ACS Nano* **6,** 3545–3552 (2012).

61. Mielke, J. *et al.* Adatoms underneath Single Porphyrin Molecules on Au(111). *Journal of the American Chemical Society* **137,** 1844–1849 (2015).

62. Saywell, A. *et al.* Manipulating the conformation of single organometallic chains on Au(111). *Journal of Physical Chemistry C* **118,** 1719–1728 (2014).

63. Shi, Z. & Lin, N. Porphyrin-Based Two-Dimensional Coordination Kagome Lattice Self-Assembled on a Au(111) Surface. *Journal of the American Chemical Society* **131,** 5376–5377 (2009).

64. Zhang, X., Zeng, Q. & Wang, C. On-surface single molecule synthesis chemistry: a promising bottom-up approach towards functional surfaces. *Nanoscale* **5,** 8269 (2013).

65. Jewell, A. D., Tierney, H. L., Zenasni, O., Lee, T. R. & Sykes, E. C. H. Asymmetric Thioethers as Building Blocks for Chiral Monolayers. *Topics in Catalysis* **54,** 1357–1367 (2011).

66. Bellisario, D. O., Jewell, A. D., Tierney, H. L., Baber, A. E. & Sykes, E. C. H. Adsorption, Assembly, and Dynamics of Dibutyl Sulfide on Au{111}. *The Journal of Physical Chemistry C* **114,** 14583–14589 (2010).

67. Cossaro, A. *et al.* X-ray diffraction and computation yield the structure of alkanethiols on gold(111). *Science (New York, N.Y.)* **321,** 943–6 (2008).

68. Maksymovych, P., Voznyy, O., Dougherty, D. B., Sorescu, D. C. & Yates, J. T. Gold adatom as a key structural component in self-assembled monolayers of organosulfur molecules on Au(111). *Progress in Surface Science* **85,** 206–240 (2010).

69. Häkkinen, H. The gold-sulfur interface at the nanoscale. *Nature chemistry* **4,** 443–55 (2012).

70. Olmos-Asar, J. A., Ludueña, M. & Mariscal, M. M. Monolayer protected gold nanoparticles: the effect of the headgroup–Au interaction. *Physical Chemistry Chemical Physics* **16,** 15979 (2014).

71. Olmos-Asar, J. A., Rapallo, A. & Mariscal, M. M. Development of a semiempirical potential for simulations of thiol–gold interfaces. Application to thiol-protected gold nanoparticles. *Physical Chemistry Chemical Physics* **13,** 6500 (2011).

72. Classen, T. *et al.* Templated Growth of Metal-Organic Coordination Chains at Surfaces. *Angewandte Chemie International Edition* **44,** 6142–6145 (2005).

73. Tseng, T.-C., Abdurakhmanova, N., Stepanow, S. & Kern, K. Hierarchical Assembly and Reticulation of Two-Dimensional Mn- and Ni–TCNQ x (x = 1, 2, 4) Coordination Structures on a Metal Surface. *The Journal of Physical Chemistry C* **115,** 10211–10217 (2011).

74. Abdurakhmanova, N. *et al.* Stereoselectivity and electrostatics in charge-transfer Mn- and Cs-TCNQ4 networks on Ag(100). *Nature Communications* **3,** 940 (2012).

75. Floris, A., Comisso, A. & De Vita, A. Fine-Tuning the Electrostatic Properties of an Alkali-Linked Organic Adlayer on a Metal Substrate. *ACS Nano* **7,** 8059–8065 (2013).

76. Feng, Z. *et al.* Trapping of Charged Gold Adatoms by Dimethyl Sulfoxide on a Gold Surface. *ACS Nano* **9,** 8697–8709 (2015).

77. Wöll, C., Chiang, S., Wilson, R. J. & Lippel, P. H. in *Physical Review B* 11, 114–117 (1989).

78. Takeuchi, N., Chan, C. & Ho, K. Au(111): A theoretical study of the surface reconstruction and the surface electronic structure. *Physical Review B* **43** (1991).

79. Smallwood, I. M. *Handbook of organic solvent properties* (Arnold; Halsted Press, London; New York, 1996).

80. Kvakovszky, G., McKim, A. & Moore, J. C. *A Review of Microelectronic Manufacturing Applications Using DMSO-Based Chemistries* in *ECS Transactions* **11** (ECS, 2007), 227–234.

81. Zhu, P. *et al.* Dissolution of Brominated Epoxy Resins by Dimethyl Sulfoxide To Separate Waste Printed Circuit Boards. *Environmental Science & Technology* **47,** 2654–2660 (2013).

82. Ashwood-Smith, M. J. Current concepts concerning radioprotective and cryoprotective properties of dimethyl sulfoxide in cellular systems. *Annals of the New York Academy of Sciences* **243,** 246–256 (1975).

83. Thong, H.-Y., Zhai, H. & Maibach, H. Percutaneous Penetration Enhancers: An Overview. *Skin Pharmacology and Physiology* **20,** 272–282 (2007).

84. Schröter, C., Roelfs, B. & Solomun, T. The interaction of dimethylsulfoxide with a gold surface. *Surface Science* **380,** L441–L445 (1997).

85. Ikemiya, N. & Gewirth, A. A. Structure Sensitive Adsorption of DMSO on Au Surfaces. *J. Phys. Chem. B* **104,** 873–877 (2000).

86. Sexton, B., Avery, N. & Turney, T. A spectroscopic study of the coordination of dimethyl sulfoxide to a platinum (111) surface. *Surface Science* **124,** 162–174 (1983).

87. Garwood, A., Garwood, G. A. & Hubbard, A. T. Superlattices formed by interaction of polar solvents with Pt(111) surfaces studied by LEED, Auger spectroscopy and thermal desorption mass spectrometry. *Surface Science* **118,** 223–247 (1982).

88. Si, S. K. & Gewirth, A. A. Complex formation between halogens and sulfoxides on metal surfaces. *Physical Chemistry Chemical Physics* **3,** 3325–3329 (2001).

89. Roelfs, B., Schröter, C. & Solomun, T. A comparison of metal/vacuum and metal/electrolyte interfaces : The Au(100)/(dimethylsulfoxide) and (dimethylsulfoxide + acetonitrile) systems. *Berichte der Bunsengesellschaft für physikalische Chemie* **101,** 1105–1112 (1997).

90. Si, S. K. & Gewirth, A. A. Solvent Organization above Metal Surfaces: Ordering of DMSO on Au. *The Journal of Physical Chemistry B* **104,** 10775–10782 (2000).

91. Thomas, R., Shoemaker, C. B. & Eriks, K. The molecular and crystal structure of dimethyl sulfoxide, (H 3 C) 2 SO. *Acta Crystallographica* **21,** 12–20 (1966).

92. Stoltze, P. Simulation of surface defects. *Journal of Physics: Condensed Matter* **6,** 9495–9517 (1994).

93. Zhang, J.-M., Song, X.-L., Zhang, X.-J., Xu, K.-W. & Ji, V. Atomistic simulation of point defects at low-index surfaces of noble metals. *Surface Science* **600,** 1277–1282 (2006).

94. Baker, T. A., Kaxiras, E. & Friend, C. M. Insights from Theory on the Relationship Between Surface Reactivity and Gold Atom Release. *Topics in Catalysis* **53,** 365–377 (2010).

95. Knak Jensen, S. J., Tang, T.-H. & Csizmadia, I. G. Hydrogen-Bonding Ability of a Methyl Group. *The Journal of Physical Chemistry A* **107,** 8975–8979 (2003).

96. Cepellotti, A. *et al.* NH 3 -NO Coadsorption System on Pt(111). II. Intermolecular Interaction. *The Journal of Physical Chemistry C* **117,** 21196–21202 (2013).

97. Desiraju, G. R. The C-H···O Hydrogen Bond: Structural Implications and Supramolecular Design. *Accounts of Chemical Research* **29,** 441–449 (1996).

98. Löwdin, P.-O. Quantum Theory of Many-Particle Systems. I. Physical Interpretations by Means of Density Matrices, Natural Spin-Orbitals, and Convergence Problems in the Method of Configurational Interaction. *Physical Review* **97,** 1474–1489 (1955).

99. Pawin, G. *et al.* A Surface Coordination Network Based on Substrate-Derived Metal Adatoms with Local Charge Excess. *Angewandte Chemie International Edition* **47,** 8442–8445 (2008).

100. Boscoboinik, J., Kestell, J., Garvey, M., Weinert, M. & Tysoe, W. T. Creation of Low-Coordination Gold Sites on Au(111) Surface by 1,4-phenylene Diisocyanide Adsorption. *Topics in Catalysis* **54,** 20–25 (2011).

101. Feng, M., Sun, H., Zhao, J. & Petek, H. Self-Catalyzed Carbon Dioxide Adsorption by Metal–Organic Chains on Gold Surfaces. *ACS Nano* **8,** 8644–8652 (2014).

102. Rim, K. T. *et al.* Charging and Chemical Reactivity of Gold Nanoparticles and Adatoms on the (111) Surface of Single-Crystal Magnetite: A Scanning Tunneling Microscopy/Spectroscopy Study. *The Journal of Physical Chemistry C* **113,** 10198–10205 (2009).

103. Chrétien, S. & Metiu, H. Density functional study of the charge on Au n clusters (n=1–7) supported on a partially reduced rutile TiO2(110): Are all clusters negatively charged? *The Journal of Chemical Physics* **126,** 104701 (2007).

104. Wörz, A. S., Heiz, U., Cinquini, F. & Pacchioni, G. Charging of Au Atoms on TiO 2 Thin Films from CO Vibrational Spectroscopy and DFT Calculations. *The Journal of Physical Chemistry B* **109,** 18418–18426 (2005).

105. Baker, T. A., Liu, X. & Friend, C. M. The mystery of gold's chemical activity: local bonding, morphology and reactivity of atomic oxygen. *Phys. Chem. Chem. Phys.* **13,** 34–46 (2011).

106. Bauer, A., Schier, A. & Schmidbaur, H. (Methyldiphenylphosphine) (trimethylsiloxy) gold(I). *Acta Crystallographica Section C Crystal Structure Communications* **51,** 2030–2032 (1995).

107. Su, C.-C. & Faller, J. W. Application of electron spectroscopy for chemical analysis to the study of ambidentate binding in sulfoxide complexes. *Inorganic Chemistry* **13,** 1734–1736 (1974).

108. Leite, T. C. M., de Barros, A. L. F., Ferreira, G. B., Guerra, A. C. O. & Turci, C. C. Photoabsorption spectroscopy of dimethyl sulfoxide at the O1s, C1s, S2s, and S2p Regions: A comparison with acetone. *International Journal of Quantum Chemistry* **112,** 3421–3433 (2012).

109. Atak, K. *et al.* The chemical bond in carbonyl and sulfinyl groups studied by soft X-ray spectroscopy and ab initio calculations. *Chemphyschem : a European journal of chemical physics and physical chemistry* **13,** 3106–11 (2012).

110. Sze, K., Brion, C., Tronc, M., Bodeur, S. & Hitchcock, A. Inner and valence shell electronic excitation of dimethyl sulfoxide by electron energy loss and photoabsorption spectroscopies. *Chemical Physics* **121,** 279–297 (1988).

111. Stöhr, J. *NEXAFS Spectroscopy* 1996th ed. (eds Ertl, G., Gomer, R., Mills, D. L. & Helmut, K. V. L.) 404 (Springer, 1992).

112. Peronio, A. *et al.* NH 3 -NO Coadsorption System on Pt(111). I. Structure of the Mixed Layer. *The Journal of Physical Chemistry C* **117,** 21186–21195 (2013).

113. Kervyn, S. *et al.* "Magic" Surface Clustering of Borazines Driven by Repulsive Intermolecular Forces. *Angewandte Chemie International Edition* **52,** 7410–7414 (2013).

114. Borkowska, Z. & Hamelin, A. The influence of the crystallographic orientation on the double layer parameters of the Au/dimethylsulphoxide interface. *Journal of Electroanalytical Chemistry and Interfacial Electrochemistry* **241,** 373–377 (1988).

115. Duggan, J. N. & Roberts, C. B. Aggregation and Precipitation of Gold Nanoparticle Clusters in Carbon Dioxide-Gas-Expanded Liquid Dimethyl Sulfoxide. *The Journal of Physical Chemistry C* **118,** 14595–14605 (2014).

116. Zeuthen, P., Knudsen, K. G. & Whitehurst, D. Organic nitrogen compounds in gas oil blends, their hydrotreated products and the importance to hydrotreatment. *Catalysis Today* **65,** 307–314 (2001).

117. Hansmeier, A. R., Meindersma, G. W. & de Haan, A. B. Desulfurization and denitrogenation of gasoline and diesel fuels by means of ionic liquids. *Green Chemistry* **13,** 1907 (2011).

118. Kamber, N. E. *et al.* Organocatalytic Ring-Opening Polymerization. *Chemical Reviews* **107,** 5813–5840 (2007).

119. Dechy-Cabaret, O., Martin-Vaca, B. & Bourissou, D. Controlled Ring-Opening Polymerization of Lactide and Glycolide. *Chemical Reviews* **104,** 6147–6176 (2004).

120. Stanislaus, A. & Cooper, B. H. Aromatic Hydrogenation Catalysis: A Review. *Catalysis Reviews* **36,** 75–123 (1994).

121. Halász, A., Baráth, Á., Simon-Sarkadi, L. & Holzapfel, W. Biogenic amines and their production by microorganisms in food. *Trends in Food Science & Technology* **5,** 42–49 (1994).

122. Bridge, M. & Somers, J. The adsorption of methylamine on Pt(111). *Vacuum* **38,** 317–320 (1988).

123. Deng, Z. *et al.* Decomposition mechanism of methylamine to hydrogen cyanide on Pt(111): selectivity of the C–H, N–H and C–N bond scissions. *RSC Advances* **4,** 12266 (2014).

124. Kang, D. & Trenary, M. Surface chemistry of ethylenediamine ($NH_2CH_2CH_2NH_2$) on Pt(111). *Surface Science* **470,** L13–L19 (2000).

125. Lv, C.-Q., Li, J., Ling, K.-C., Shang, Z.-F. & Wang, G.-C. Methylamine decomposition on nickel surfaces: A density functional theory study. *Surface Science* **604,** 779–787 (2010).

126. Nunney, T., Birtill, J. & Raval, R. Infrared studies of sub-monolayer methylamine and trimethylamine adsorption on Ni(111). *Surface Science* **427-428,** 282–287 (1999).

127. Chorkendorff, I., Russell, J. N. & Yates, J. T. Surface reaction pathways of methylamine on the Ni(111) surface. *The Journal of Chemical Physics* **86,** 4692 (1987).

128. Baca, A. G., Schulz, M. A. & Shirley, D. A. Electron energy loss spectroscopy (EELS) of CH_3NH_2 adsorbed on Ni(100), Ni(111), Cr(100), and Cr(111). *The Journal of Chemical Physics* **83,** 6001 (1985).

129. Sasaki, T., Aruga, T., Kuroda, H. & Iwasawa, Y. Coadsorption of CO and methylamine on Ru(001): effects of coadsorbed CO on dissociation paths of methylamine. *Surface Science Letters* **249,** L347–L353 (1991).

130. Johnson, D. F., Wang, Y., Parmeter, J. E., Hills, M. M. & Weinberg, W. H. Chemisorption and thermal decomposition of methylamine on the ruthenium(001) surface. *Journal of the American Chemical Society* **114,** 4279–4290 (1992).

131. Chen, J. & Winograd, N. The adsorption and decomposition of methylamine on Pd{111}. *Surface Science* **326,** 285–300 (1995).

132. Venkataraman, L., Klare, J. E., Nuckolls, C., Hybertsen, M. S. & Steigerwald, M. L. Dependence of single-molecule junction conductance on molecular conformation. *Nature* **442,** 904–907 (2006).

133. Hoft, R. C., Ford, M. J., McDonagh, A. M. & Cortie, M. B. Adsorption of Amine Compounds on the Au(111) Surface: A Density Functional Study. *The Journal of Physical Chemistry C* **111,** 13886–13891 (2007).

134. Balducci, G. *et al.* Computational Study of Amino Mediated Molecular Interaction Evidenced in N 1s NEXAFS: 1,4-Diaminobenzene on Au (111). *The Journal of Physical Chemistry C* **119,** 1988–1995 (2015).

135. Kladnik, G. *et al.* Ultrafast Charge Transfer through Noncovalent Au-N Interactions in Molecular Systems. *The Journal of Physical Chemistry C* **117,** 16477–16482 (2013).

136. Dri, C. *et al.* Chemistry of the Methylamine Termination at a Gold Surface: From Autorecognition to Condensation. *The Journal of Physical Chemistry C* **120,** 6104–6115 (2016).

137. Hanke, F. & Björk, J. Structure and local reactivity of the Au(111) surface reconstruction. *Physical Review B* **87,** 235422 (2013).

138. Cossaro, A. *et al.* Amine Functionalization of Gold Surfaces: Ultra High Vacuum Deposition of Cysteamine on Au(111). *The Journal of Physical Chemistry C* **114,** 15011–15014 (2010).

139. Minkov, I. *et al.* Core excitations of naphthalene: Vibrational structure versus chemical shifts. *The Journal of Chemical Physics* **121,** 5733 (2004).

140. Hollauer, E. *et al.* Configuration interaction simulation of the NEXAFS photoabsorption spectrum of naphthalene. *Journal of the Brazilian Chemical Society* **16,** 31–36 (2005).

141. Plekan, O. *et al.* An X-ray absorption study of glycine, methionine and proline. *Journal of Electron Spectroscopy and Related Phenomena* **155,** 47–53 (2007).

142. Nyberg, M. *et al.* The electronic structure and surface chemistry of glycine adsorbed on Cu(110). *The Journal of Chemical Physics* **112,** 5420 (2000).

143. Graf, N. *et al.* XPS and NEXAFS studies of aliphatic and aromatic amine species on functionalized surfaces. *Surface Science* **603,** 2849–2860 (2009).

144. Czapik, A., Konowalska, H. & Gdaniec, M. p -Phenylenediamine and its dihydrate: two-dimensional isomorphism and mechanism of the dehydration process, and N—H···N and N—H···π interactions. *Acta Crystallographica Section C Crystal Structure Communications* **66,** 0128–0132 (2010).

145. Jiang, P., Nion, A., Marchenko, A., Piot, L. & Fichou, D. Rotational Polymorphism in 2-Naphthalenethiol SAMs on Au(111). *Journal of the American Chemical Society* **128,** 12390–12391 (2006).

146. Tsuzuki, S., Honda, K., Uchimaru, T., Mikami, M. & Tanabe, K. Origin of the Attraction and Directionality of the NH/π Interaction: Comparison with OH/π and CH/π Interactions. *Journal of the American Chemical Society* **122,** 11450–11458 (2000).

147. Worth, G. A. & Wade, R. C. Aromatic-(i+2) Amine Interaction in Peptides. *The Journal of Physical Chemistry* **99,** 17473–17482 (1995).

148. Wheeler, S. E. & Bloom, J. W. G. Toward a More Complete Understanding of Noncovalent Interactions Involving Aromatic Rings. *The Journal of Physical Chemistry A* **118,** 6133–6147 (2014).

149. Salonen, L. M., Ellermann, M. & Diederich, F. Aromatic Rings in Chemical and Biological Recognition: Energetics and Structures. *Angewandte Chemie International Edition* **50,** 4808–4842 (2011).

150. Weigelt, S. *et al.* Formation of Trioctylamine from Octylamine On Au(111). *Journal of the American Chemical Society* **130,** 5388–5389 (2008).

151. Auwärter, W., Écija, D., Klappenberger, F. & Barth, J. V. Porphyrins at interfaces. *Nature Chemistry* **7,** 105–120 (2015).

152. Otsuki, J. STM studies on porphyrins. *Coordination Chemistry Reviews* **254,** 2311–2341 (2010).

153. Mohnani, S. & Bonifazi, D. Supramolecular architectures of porphyrins on surfaces: The structural evolution from 1D to 2D to 3D to devices. *Coordination Chemistry Reviews* **254,** 2342–2362 (2010).

154. Yokoyama, T., Yokoyama, S., Kamikado, T. & Mashiko, S. Nonplanar adsorption and orientational ordering of porphyrin molecules on Au(111). *The Journal of Chemical Physics* **115,** 3814 (2001).

155. Fendt, L. A. *et al.* Modification of supramolecular binding motifs induced by substrate registry: Formation of self-assembled macrocycles and chain-like patterns. *Chemistry - A European Journal* **15,** 11139–11150 (2009).

156. Grill, L. *et al.* Nano-architectures by covalent assembly of molecular building blocks. *Nature Nanotechnology* **2,** 687–691 (2007).

157. Lafferentz, L. *et al.* Controlling on-surface polymerization by hierarchical and substrate-directed growth. *Nature Chemistry* **4,** 215–220 (2012).

158. Heim, D. *et al.* Self-assembly of flexible one-dimensional coordination polymers on metal surfaces. *Journal of the American Chemical Society* **132,** 6783–6790 (2010).

159. Heim, D. *et al.* Surface-assisted assembly of discrete porphyrin-based cyclic supramolecules. *Nano Letters* **10,** 122–128 (2010).

160. Haq, S. *et al.* Clean coupling of unfunctionalized porphyrins at surfaces to give highly oriented organometallic oligomers. *Journal of the American Chemical Society* **133,** 12031–12039 (2011).

161. Pham, T. A. *et al.* Heat-induced formation of one-dimensional coordination polymers on Au(111): an STM study. *Chem. Commun.* **51,** 14473–14476 (2015).

162. Liljeroth, P., Repp, J. & Meyer, G. Current-Induced Hydrogen Tautomerization and Conductance Switching of Naphthalocyanine Molecules. *Science* **317,** 1203–1206 (2007).

163. Auwärter, W. *et al.* A surface-anchored molecular four-level conductance switch based on single proton transfer. *Nature Nanotechnology* **7,** 41–46 (2011).

164. Qiu, X. H., Nazin, G. V. & Ho, W. Mechanisms of Reversible Conformational Transitions in a Single Molecule. *Physical Review Letters* **93,** 196806 (2004).

165. Wang, Y., Kröger, J., Berndt, R. & Hofer, W. A. Pushing and Pulling a Sn Ion through an Adsorbed Phthalocyanine Molecule. *Journal of the American Chemical Society* **131,** 3639–3643 (2009).

166. Venkataraman, L. *et al.* Single-molecule circuits with well-defined molecular conductance. *Nano Letters* **6,** 458–462 (2006).

167. Scudiero, L., Barlow, D. E. & Hipps, K. W. Physical Properties and Metal Ion Specific Scanning Tunneling Microscopy Images of Metal(II) Tetraphenylporphyrins Deposited from Vapor onto Gold (111). *The Journal of Physical Chemistry B* **104,** 11899–11905 (2000).

168. Moresco, F. *et al.* TBPP molecules on copper surfaces: a low temperature scanning tunneling microscope investigation. *Surface Science* **499,** 94–102 (2002).

169. Auwärter, W. *et al.* Self-assembly and conformation of tetrapyridyl-porphyrin molecules on Ag(111). *The Journal of chemical physics* **124,** 194708 (2006).

170. Seufert, K. *et al.* Cis-dicarbonyl binding at cobalt and iron porphyrins with saddle-shape conformation. *Nature Chemistry* **3,** 114–119 (2011).

171. Wang, Y., Zhou, K., Shi, Z. & Ma, Y.-q. Structural reconstruction and spontaneous formation of Fe polynuclears: a self-assembly of Fe–porphyrin coordination chains on Au(111) revealed by scanning tunneling microscopy. *Phys. Chem. Chem. Phys.* **18,** 14273–14278 (2016).

172. Meyer, J. *et al.* Tuning the formation of discrete coordination nanostructures. *Chem. Commun.* **51,** 12621–12624 (2015).

173. Klappenberger, F. *et al.* Temperature dependence of conformation, chemical state, and metal-directed assembly of tetrapyridyl-porphyrin on Cu(111). *The Journal of chemical physics* **129,** 214702 (2008).

174. Röckert, M. *et al.* Coverage- and temperature-dependent metalation and dehydrogenation of tetraphenylporphyrin on cu(111). *Chemistry (Weinheim an der Bergstrasse, Germany)* **20,** 8948–53 (2014).

175. Bürker, C. *et al.* Self-Metalation of 2 H -Tetraphenylporphyrin on Cu(111) Studied with XSW: Influence of the Central Metal Atom on the Adsorption Distance. *The Journal of Physical Chemistry C* **118,** 13659–13666 (2014).

176. González-Moreno, R. *et al.* Following the Metalation Process of Protoporphyrin IX with Metal Substrate Atoms at Room Temperature. *The Journal of Physical Chemistry C* **115,** 6849–6854 (2011).

177. Goldoni, A. *et al.* Room Temperature Metalation of 2H-TPP Monolayer on Iron and Nickel Surfaces by Picking up Substrate Metal Atoms. *ACS Nano* **6,** 10800–10807 (2012).

178. Diller, K. *et al.* Self-metalation of 2H-tetraphenylporphyrin on Cu(111): An x-ray spectroscopy study. *The Journal of Chemical Physics* **136,** 014705 (2012).

179. Chen, M. *et al.* Direct Synthesis of Nickel(II) Tetraphenylporphyrin and Its Interaction with a Au(111) Surface: A Comprehensive Study. *The Journal of Physical Chemistry C* **114,** 9908–9916 (2010).

180. Papageorgiou, A. C. *et al.* Self-terminating protocol for an interfacial complexation reaction in vacuo by metal-organic chemical vapor deposition. *ACS nano* **7,** 4520–6 (2013).

181. Di Santo, G. *et al.* Supramolecular engineering through temperature-induced chemical modification of 2H-tetraphenylporphyrin on Ag(111): flat phenyl conformation and possible dehydrogenation reactions. *Chemistry (Weinheim an der Bergstrasse, Germany)* **17,** 14354–9 (2011).

182. Choi, B. Y. *et al.* Conformational molecular switch of the azobenzene molecule: A scanning tunneling microscopy study. *Physical Review Letters* **96,** 1–4 (2006).

183. Capozzi, B. *et al.* Single-molecule diodes with high rectification ratios through environmental control. *Nature Nanotechnology* **10,** 522–527 (2015).

184. Kumagai, T. *et al.* Controlling intramolecular hydrogen transfer in a porphycene molecule with single atoms or molecules located nearby. *Nature chemistry* **6,** 41–6 (2014).

185. Simpson, G. J. *et al.* New class of metal bound molecular switches involving H-tautomerism. *Nano letters* **14,** 634–9 (2014).

186. Ladenthin, J. N. *et al.* Hot Carrier-Induced Tautomerization within a Single Porphycene Molecule on Cu(111). *ACS Nano,* 150612155017004 (2015).

187. Böckmann, H. *et al.* Direct Observation of Photoinduced Tautomerization in Single Molecules at a Metal Surface. *Nano Letters* **16,** 1034–1041 (2016).

188. Nacci, C., Erwin, S. C., Kanisawa, K. & Fölsch, S. Controlled Switching within an Organic Molecule Deliberately Pinned to a Semiconductor Surface. *ACS Nano* **6,** 4190–4195 (2012).

189. Auwärter, W. *et al.* Site-specific electronic and geometric interface structure of Co-tetraphenyl-porphyrin layers on Ag(111). *Physical Review B* **81,** 245403 (2010).

190. Cicoira, F., Santato, C. & Rosei, F. in *Top Curr Chem* April, 203–267 (2008).

191. Lackinger, M. & Heckl, W. M. Carboxylic Acids: Versatile Building Blocks and Mediators for Two-Dimensional Supramolecular Self-Assembly. *Langmuir* **25,** 11307–11321 (2009).

192. Ivasenko, O. & Perepichka, D. F. Mastering fundamentals of supramolecular design with carboxylic acids. Common lessons from X-ray crystallography and scanning tunneling microscopy. *Chem. Soc. Rev.* **40,** 191–206 (2011).

193. Carrera, a. *et al.* Controlling Carboxyl Deprotonation on Cu(001) by Surface Sn Alloying. *The Journal of Physical Chemistry C* **117,** 17058–17065 (2013).

194. Etter, M. C. & Adsmond, D. A. The use of cocrystallization as a method of studying hydrogen bond preferences of 2-aminopyrimidine. *Journal of the Chemical Society, Chemical Communications* **589,** 589 (1990).

195. Almarsson, Ö. & Zaworotko, M. J. Crystal engineering of the composition of pharmaceutical phases. Do pharmaceutical co-crystals represent a new path to improved medicines? *Chemical Communications,* 1889–1896 (2004).

196. Mukherjee, A. & Desiraju, G. R. Synthon polymorphism and pseudopolymorphism in co-crystals. The 4,4'-bipyridine-4-hydroxybenzoic acid structural landscape. *Chemical Communications* **47,** 4090 (2011).

197. Aakeröy, C. B., Desper, J. & Urbina, J. F. Supramolecular reagents: versatile tools for non-covalent synthesis. *Chemical Communications* **6081,** 2820 (2005).

198. Kühnle, a., Molina, L. M., Linderoth, T. R., Hammer, B. & Besenbacher, F. Growth of Unidirectional Molecular Rows of Cysteine on Au(110)-(1×2) Driven by Adsorbate-Induced Surface Rearrangements. *Physical Review Letters* **93,** 086101 (2004).

199. Cossaro, A. *et al.* Electronic and geometric characterization of the L-cysteine paired-row phase on Au(110). *Langmuir* **22,** 11193–11198 (2006).

200. Humblot, V. *et al.* Characterization of Two-Dimensional Chiral Self-Assemblies L- and D-Methionine on Au(111). *Langmuir* **30,** 203–212 (2014).

201. Reichert, J. *et al.* L-Tyrosine on Ag(111): Universality of the Amino Acid 2D Zwitterionic Bonding Scheme? *ACS Nano* **4,** 1218–1226 (2010).

202. Mateo Marti, E., Barlow, S., Haq, S. & Raval, R. Bonding and assembly of the chiral amino acid S-proline on Cu(110): the influence of structural rigidity. *Surface Science* **501,** 191–202 (2002).

203. Stepanow, S. *et al.* Deprotonation-Driven Phase Transformations in Terephthalic Acid Self-Assembly on Cu(100). *The Journal of Physical Chemistry B* **108,** 19392–19397 (2004).

204. Cossaro, A. *et al.* Tailoring SAM-on-SAM Formation. *The Journal of Physical Chemistry Letters* **2,** 3124–3129 (2011).

205. Theobald, J. a., Oxtoby, N. S., Phillips, M. a., Champness, N. R. & Beton, P. H. Controlling molecular deposition and layer structure with supramolecular surface assemblies. *Nature* **424,** 1029–1031 (2003).

206. Sun, X., Jonkman, H. T. & Silly, F. Tailoring two-dimensional PTCDA–melamine self-assembled architectures at room temperature by tuning molecular ratio. *Nanotechnology* **21,** 165602 (2010).

207. Cossaro, A., Cvetko, D. & Floreano, L. Amino-carboxylic recognition on surfaces: from 2D to 2D + 1 nano-architectures. *Physical chemistry chemical physics : PCCP* **14,** 13154–62 (2012).

208. Uvdal, K., Bodö, P. & Liedberg, B. l-cysteine adsorbed on gold and copper: An X-ray photoelectron spectroscopy study. *Journal of Colloid and Interface Science* **149,** 162–173 (1992).

209. Colson, J. W. & Dichtel, W. R. Rationally synthesized two-dimensional polymers. *Nature Chemistry* **5,** 453–465 (2013).

210. Griessl, S., Lackinger, M., Edelwirth, M., Hietschold, M. & Heckl, W. M. Self-Assembled Two-Dimensional Molecular Host-Guest Architectures From Trimesic Acid. *Single Molecules* **3,** 25–31 (2002).

211. Elemans, J. A. A. W., Lei, S. & De Feyter, S. Molecular and Supramolecular Networks on Surfaces: From Two-Dimensional Crystal Engineering to Reactivity. *Angewandte Chemie International Edition* **48,** 7298–7332 (2009).

212. Zwaneveld, N. A. A. *et al.* Organized Formation of 2D Extended Covalent Organic Frameworks at Surfaces. *Journal of the American Chemical Society* **130,** 6678–6679 (2008).

213. Liang, H. *et al.* Two-dimensional molecular porous networks constructed by surface assembling. *Coordination Chemistry Reviews* **253,** 2959–2979 (2009).

214. Yoshimoto, S., Honda, Y., Ito, O. & Itaya, K. Supramolecular Pattern of Fullerene on 2D Bimolecular "Chessboard" Consisting of Bottom-up Assembly of Porphyrin and Phthalocyanine Molecules. *Journal of the American Chemical Society* **130,** 1085–1092 (2008).

215. Stepanow, S., Lin, N., Barth, J. V. & Kern, K. Non-covalent binding of fullerenes and biomolecules at surface-supported metallosupramolecular receptors. *Chemical Communications,* 2153 (2006).

216. MacLeod, J. M., Ben Chaouch, Z., Perepichka, D. F. & Rosei, F. Two-Dimensional Self-Assembly of a Symmetry-Reduced Tricarboxylic Acid. *Langmuir* **29,** 7318–7324 (2013).

217. Madueno, R., Räisänen, M. T., Silien, C. & Buck, M. Functionalizing hydrogen-bonded surface networks with self-assembled monolayers. *Nature* **454,** 618–621 (2008).

218. Sung Cho, H. *et al.* Extra adsorption and adsorbate superlattice formation in metal-organic frameworks. *Nature* **527,** 503–507 (2015).

219. Perdigão, L. M. A. *et al.* Functionalized Supramolecular Nanoporous Arrays for Surface Templating. *Chemistry - A European Journal* **14,** 7600–7607 (2008).

220. Collman, J. P., Devaraj, N. K. & Chidsey, C. E. D. "Clicking" Functionality onto Electrode Surfaces. *Langmuir* **20,** 1051–1053 (2004).

221. Frasconi, M., Mazzei, F. & Ferri, T. Protein immobilization at gold–thiol surfaces and potential for biosensing. *Analytical and Bioanalytical Chemistry* **398,** 1545–1564 (2010).

222. Rusmini, F., Zhong, Z. & Feijen, J. Protein Immobilization Strategies for Protein Biochips. *Biomacromolecules* **8,** 1775–1789 (2007).

223. Liu, G.-Y. & Amro, N. A. Positioning protein molecules on surfaces: A nanoengineering approach to supramolecular chemistry. *Proceedings of the National Academy of Sciences* **99,** 5165–5170 (2002).

224. Amro, N. A., Xu, S. & Liu, G.-y. Patterning Surfaces Using Tip-Directed Displacement and Self-Assembly. *Langmuir* **16,** 3006–3009 (2000).

225. Geissler, M. & Xia, Y. Patterning: Principles and Some New Developments. *Advanced Materials* **16,** 1249–1269 (2004).

226. Ginger, D. S., Zhang, H. & Mirkin, C. A. The Evolution of Dip-Pen Nanolithography. *Angewandte Chemie International Edition* **43,** 30–45 (2004).

227. Frederick, B., Ashton, M., Richardson, N. & Jones, T. Orientation and bonding of benzoic acid, phthalic anhydride and pyromellitic dianhydride on Cu(110). *Surface Science Letters* **292,** A603 (1993).

228. Lei, S. B. *et al.* Surface Stabilized Porphyrin and Phthalocyanine Two-Dimensional Network Connected by Hydrogen Bonds. *The Journal of Physical Chemistry B* **105,** 10838–10841 (2001).

229. Gokel, G. W., Leevy, W. M. & Weber, M. E. Crown Ethers: Sensors for Ions and Molecular Scaffolds for Materials and Biological Models. *Chemical Reviews* **104,** 2723–2750 (2004).

230. Banerjee, M., Gupta, A., Saha, S. K. & Chakravorty, D. 1-Aza-15-Crown-5 Functionalized Graphene Oxide for 2D Graphene-Based Li + -ion Conductor. *Small* **11,** 3451–3457 (2015).

231. Lin, S.-Y., Liu, S.-w., Lin, C.-m. & Chen, C.-h. Recognition of Potassium Ion in Water by 15-Crown-5 Functionalized Gold Nanoparticles. *Analytical Chemistry* **74,** 330–335 (2002).